

KEK Proceedings 2010-9
November 2010
R

Proceedings of the Seventeenth EGS Users' Meeting in Japan

August 2 - 4, 2010.
KEK, Tsukuba, Japan

Edited by

Y. Namito, H. Hirayama and S. Ban



High Energy Accelerator Research Organization

High Energy Accelerator Research Organization (KEK), 2010

KEK Reports are available from:

High Energy Accelerator Research Organization (KEK)
1-1 Oho, Tsukuba-shi
Ibaraki-ken, 305-0801
JAPAN

Phone: +81-29-864-5137
Fax: +81-29-864-4604
E-mail: irdpub@mail.kek.jp
Internet: <http://www.kek.jp>

FOREWARD

The Seventeenth EGS Users' Meeting in Japan was held at High Energy Accelerator Research Organization (KEK) from August 2 to 4. The meeting has been hosted by the Radiation Science Center. More than 100 participants attended the meeting.

The meeting was divided into two parts. Short course on EGS was held at the first half of the workshop using EGS5 code. In the later half, 14 talks related EGS were presented. The talk covered the wide fields, like the medical application and the calculation of various detector responses *etc.* These talks were very useful to exchange the information between the researchers in the different fields.

Finally, we would like to express our great appreciation to all authors who have prepared manuscript quickly for the publication of this proceedings.

Hideo Hirayama
Yoshihito Namito
Syuichi Ban
Radiation Science Center
KEK, High Energy Accelerator Research Organization

CONTENTS

Numerical Calculation of the Goudsmit-Saunderson Multiple Scattering Angular Distribution	1
<i>K. Okei and T. Nakatsuka</i>	
Use of Meth Tallies in the Combinatorial Geometry of the EGS5 Code	7
<i>T. Sugita and T. Torii</i>	
Development of Monte Carlo Dose Verification System for MHI-TM2000	19
<i>Y. Ishihara, A. Sawada, M. Nakamura, S. Kaneko, K. Takayama, T. Mizowaki, M. Kokubo, and M. Hiraoka</i>	
Dose Characteristics of the ^{125}I Seeds for Prostate Brachytherapy	25
<i>T. Matsunaga, N. Kataoka, K. Yasui, T. Shimozato, H. Fuse, Y. Oribe, Y. Igarashi, M. Komori, and Y. Obata</i>	
Dose Distribution for Iodine-125 Seed Implant Brachytherapy	33
<i>S. Wakumura, K. Koshida, K. Matsubara, Y. Kurata, S. Ueda, and K. Noto</i>	
Angular Dependence of ^{192}Ir HDR Radiation Source for Treatment	41
<i>S. Tsuji and N. Narihiro</i>	
Fundamental Study for 3-Dimensional Dose Verification from Compton Scattered Photons Using EGS Simulation	50
<i>T. Kodama, A. Myojoyama, and H. Saitoh</i>	
Investigation of Influence by Gold Crown to Radiation Therapy in Oral Cavity	58
<i>Y. Igarashi, Y. Ito, T. Shimozato, M. Komori, and Y. Obata</i>	
Electron Absorbed Fractions and S Values in a Mouse Voxel Phantom	65
<i>A. Mohammadi and S. Kinase</i>	
Calculation of Dose Equivalent for Positrons Using the Monte Carlo Code EGS5	75
<i>T. Kato, K. Aoki, S. Yokoyama, K. Minami, H. Yashima, A. Taniguchi, T. Nakamura, and H. Hirayama</i>	
Estimation of Patient Exposure Doses Using Anthropomorphic Phantom Undergoing X-ray CT Examination	82
<i>Y. Morishita and S. Koyama</i>	
Monte Carlo Simulation of Energy Deposition in Imaging Plate	89
<i>T. Miyata, H. Rito, M. Kajihara, T. Yamauchi, and K. Oda</i>	
Development of an MC Generator for Polarized γ Conversion to an e^+e^- Pair	94
<i>D. Bernard</i>	

Numerical calculation of the Goudsmit-Saunderson multiple scattering angular distribution

K. Okei[†] and T. Nakatsuka[‡]

[†]*Kawasaki Medical School, Kurashiki 701-0192, Japan*

[‡]*Okayama Shoka University, Okayama 700-8601, Japan*

Abstract

Several methods for accelerating the numerical computation of the Goudsmit-Saunderson multiple scattering angular distribution have been studied. It was found that the double exponential formula is very efficient for the numerical integration of obtaining Legendre coefficients and the convergence of the Legendre series can be accelerated with the transformation proposed by Yennie, Ravenhall and Wilson (1954).

1 Introduction

Charged particles passing through matter suffer deflections due to the Coulomb scattering, and the process is the main source of the angular and lateral spreads. However, in Monte Carlo simulations at high energies, sampling all deflections is unfeasible because of the huge number of events. Hence, multiple scattering theories are employed [1, 2, 3].

Molière's theory [4, 5, 6] is widely used in Monte Carlo codes but it can only be accurate where the small angle approximation is valid. On the other hand, the theories of Goudsmit-Saunderson [7, 8] and of Lewis [9] are applicable to large angle scattering. However in their theories, the multiple scattering angular distribution has the form of a Legendre series and its computation can require thousands of terms to converge. Therefore we studied several methods to accelerate the numerical computation of the Goudsmit-Saunderson distribution.

2 Multiple scattering distribution

In the Goudsmit-Saunderson theory, the multiple scattering angular distribution $f(\theta)$ after a path length t is described as

$$\begin{aligned} f(\theta) &= \sum_{l=0}^{\infty} \frac{2l+1}{4\pi} \exp \left[-\frac{t}{\lambda} \left\{ 1 - \int_0^{\pi} 2\pi \sin \theta f_1(\theta) P_l(\cos \theta) d\theta \right\} \right] P_l(\cos \theta) \\ &= \sum_{l=0}^{\infty} \frac{2l+1}{4\pi} \exp \left[-\frac{t}{\lambda} \left\{ 1 - \int_{-1}^1 2\pi f_1(\theta) P_l(\cos \theta) d\cos \theta \right\} \right] P_l(\cos \theta) \\ &= \sum_{l=0}^{\infty} \frac{2l+1}{4\pi} \exp \left[-\frac{t}{\lambda} \{1 - F_l\} \right] P_l(\cos \theta) \\ &= \sum_{l=0}^{\infty} \frac{2l+1}{4\pi} \exp \left[-\frac{t}{\lambda} g_l \right] P_l(\cos \theta) \end{aligned} \tag{1}$$

where λ is the mean free path, $f_1(\theta)$ is the single scattering angular distribution and P_l are the Legendre polynomials. To test the numerical computation, we used the screened Rutherford cross

section and f_1 , F_l can be written as

$$2\pi f_1(\theta) = \frac{\chi_a^2(\chi_a^2 + 4)}{8} / 4 \left(\sin^2 \frac{\theta}{2} + \frac{\chi_a^2}{4} \right)^2 = \frac{\chi_a^2(\chi_a^2 + 4)}{8} / \left(1 - \cos \theta + \frac{\chi_a^2}{2} \right)^2 \quad (2)$$

$$F_l = \frac{\chi_a^2(\chi_a^2 + 4)}{8} \frac{1}{2} \left(\frac{\chi_a^2}{4} \right)^{-l-2} \frac{\Gamma(l+1)\Gamma(l+2)}{\Gamma(2l+2)} {}_2F_1 \left(l+1, l+2; 2l+2; - \left(\frac{\chi_a^2}{4} \right)^{-1} \right). \quad (3)$$

Here χ_a is the screening angle [4, 5, 6] and ${}_2F_1$ is the hypergeometric function [9].

2.1 Numerical integration

Since the integration for obtaining F_l must be performed for each term of the series, an efficient and fast algorithm should be selected. Here we tested the Gauss-Legendre (GL) quadrature [10] and the double exponential (DE) formula [11, 12, 13].

Two integral variables θ and $\mu = \cos \theta$ were examined for faster convergence. We also tested the effect of splitting the interval of integration $[0, \pi]$ over θ ($[-1, 1]$ over μ) into two intervals, $[0, \theta_d]$ and $[\theta_d, \pi]$ ($[-1, \mu_d]$ and $[\mu_d, 1]$). Because the integrand is steep near $\theta = 0$ ($\mu = 1$), θ_d (μ_d) is set to be the zero point of F_l closest to $\theta = 0$ ($\mu = 1$).

2.1.1 Gauss-Legendre quadrature

Figure 1 shows the relative error of F_l computed by GL quadrature, $|F_{l, \text{GL}} - F_l|/F_l$, as a function of the number of abscissas with integration variable θ (cross) and μ (plus) for $l = 100$ (left: $\chi_a = 0.1$ right: $\chi_a = 0.001$) and figure 2 shows the error for $\chi_a = 0.01$ (left: $l = 100$ right: $l = 1000$). Results obtained with the integration range divided are also shown (square and asterisk). (In the cases of the integrations with the interval splitting, the numbers of abscissas were doubled.) It can be seen that GL with θ converges faster than with μ and the interval splitting improves convergence for smaller χ_a . For the $l = 1000$ case, even 1024 points GL integration fails to achieve an relative error of 10^{-6} .

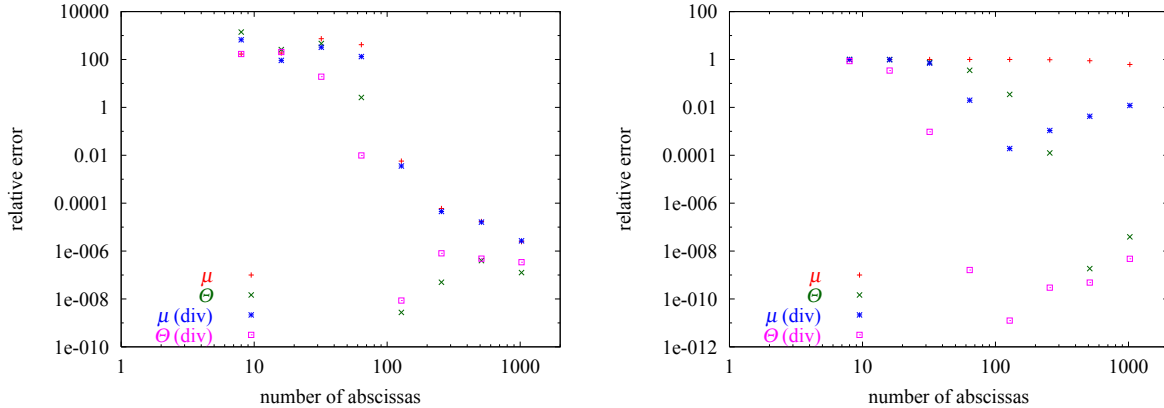


Figure 1: The relative error of F_l computed by GL for $l = 100$. (left: $\chi_a = 0.1$ right: $\chi_a = 0.001$)

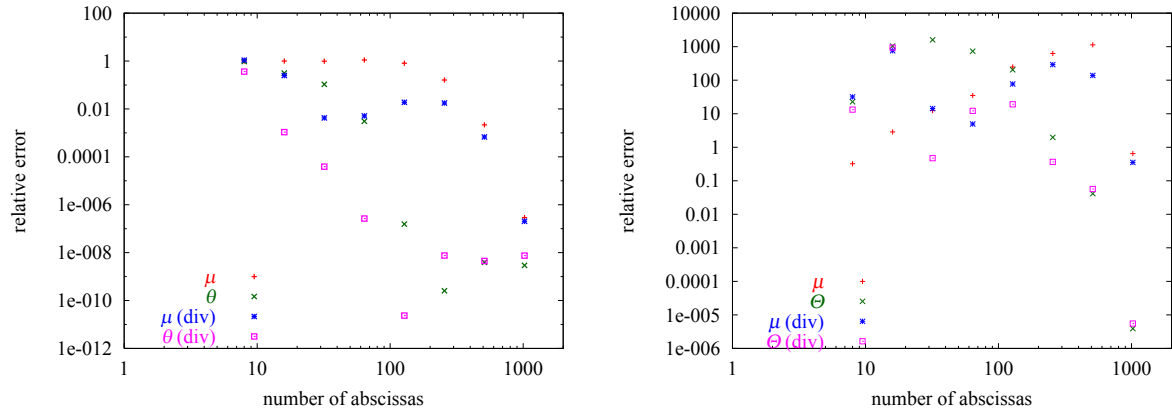


Figure 2: The relative error of F_l computed by GL for $\chi_a = 0.01$. (left: $l = 100$ right: $l = 1000$)

2.1.2 Double exponential formula

DE formula is well known to be very powerful for numerical integrations. It can be used for the evaluation of oscillatory functions [11, 12, 13] and we have applied the method to obtain the small angle multiple scattering distribution [14]. Here we study the efficiency of DE method for calculating the Goudsmit-Saunders distribution using the routines `intde` and `intdeo` [15] provided by the author of refs. [11] and [12].

Figure 3 shows the number of integrand function calls required for convergence of the numerical integration of F_l as a function of l for $\chi_a = 0.01$. The open and solid circles show the results from `intde` and `intdeo` routines respectively. In the calculations, the relative error tolerance was set to be 10^{-15} (the real relative error may be larger than this value due to the cancellation of significant digits). For larger l , say, $l > 50$, `intdeo` converges faster than `intde`.

The resultant F_l and its relative error are shown in the left and right panels of figure 4 respectively. It is noteworthy that the relative error of `intdeo` is less than 10^{-6} up to $l \sim 13000$.

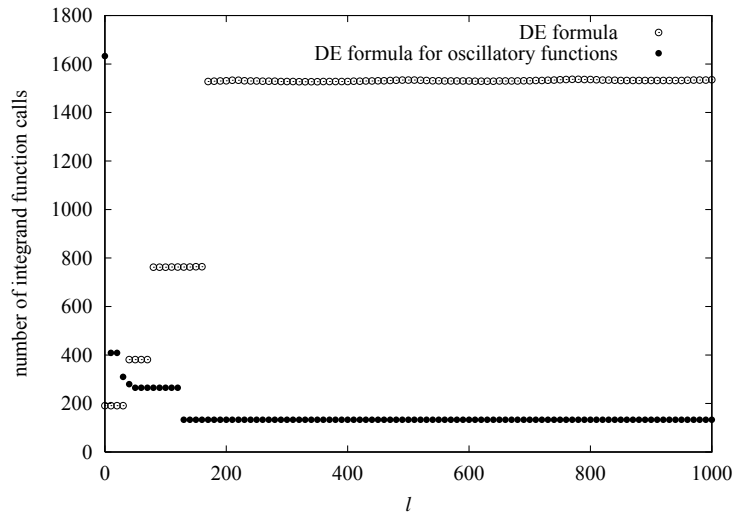


Figure 3: The number of integrand function calls required for convergence of the numerical integration of F_l as a function of l for $\chi_a = 0.01$.

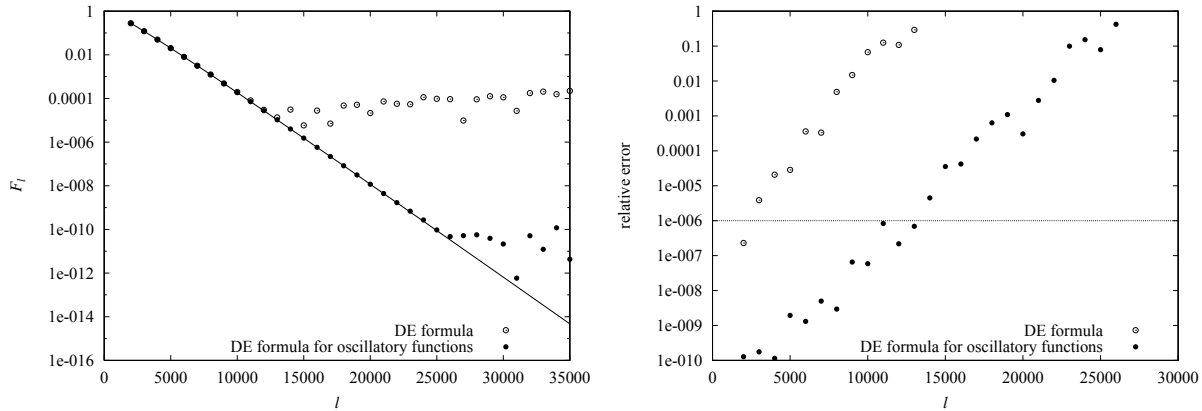


Figure 4: The numerically calculated F_l (left) and its relative error (right) for $\chi_a = 0.01$. The solid curve in the left panel shows the analytical solution (eq. (3)).

2.2 Convergence acceleration of series

Because the convergence of the series (1) is slow, we transform them for $\theta \neq 0$, following Yennie, Ravenhall and Wilson [16, 17, 18], as

$$(1 - \cos \theta)^m f(\theta) = \sum_{l=0}^{\infty} a_l^{(m)} P_l(\cos \theta) \quad (4)$$

where

$$\begin{aligned} a_l^{(m)} &= a_l^{(m-1)} - \frac{l+1}{2l+3} a_{l+1}^{(m-1)} - \frac{l}{2l-1} a_{l-1}^{(m-1)}, \\ a_l^{(0)} &= \frac{2l+1}{4\pi} \exp\left[-\frac{t}{\lambda} gl\right], \end{aligned}$$

and $a_l^{(m)} = 0$ for $l < 0$. This transformation is derived from the recurrence relation of the Legendre polynomials,

$$(2l+1)xP_l(x) = lP_{l-1}(x) + (l+1)P_{l+1}(x)$$

and can be applied to any series of the same form $f(x) = \sum a_l P_l(x)$.

Figure 5 shows the number of terms required for convergence for $\chi_a = 10^{-4}$, $m = 3$ and $t/\lambda = 1000$ (left panel), 100 (right panel). In the computation, the relative error tolerance and the maximum number of terms were set to be 10^{-6} and 2000 respectively. Except for very small angles, the transformed series converge much faster. In the case of very short path lengths, it seems that the cancellation of significant digits prevents convergence of the transformed series.

The Goudsmit-Saunderson multiple scattering angular distributions computed by the direct and transformed series are compared in figure 6 for $\chi_a = 10^{-4}$ and $t/\lambda = 1000$. It can be seen that the transformed series give the same distribution as the direct one.

3 Conclusion

We have studied several methods to accelerate the numerical computation of the Goudsmit-Saunderson multiple scattering angular distribution. It was found that the double exponential method is very efficient for the integration for obtaining F_l and the convergence of the Legendre series can be accelerated by the transformation (4).

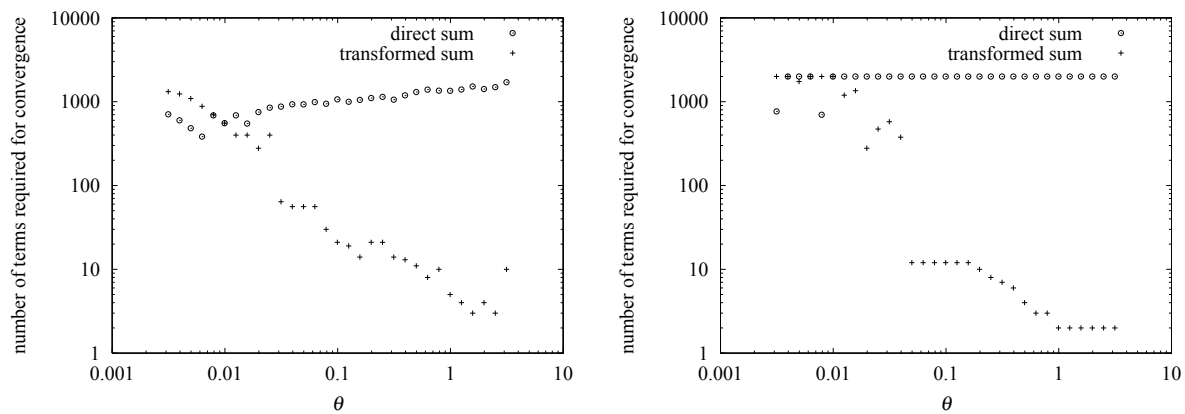


Figure 5: The number of terms required for convergence for $\chi_a = 10^{-4}$. (left: $t/\lambda = 1000$ right: $t/\lambda = 100$)

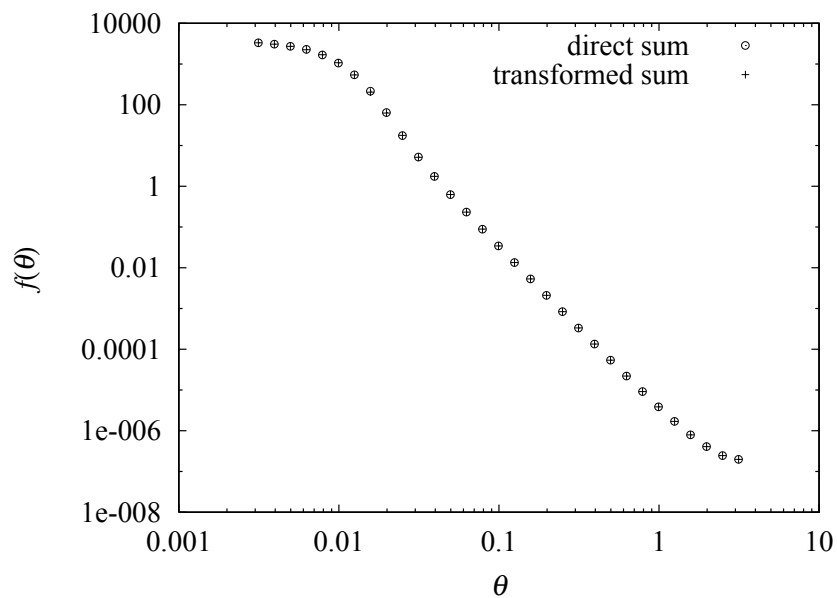


Figure 6: The Goudsmit-Saunders multiple scattering angular distribution for $\chi_a = 10^{-4}$ and $t/\lambda = 1000$.

References

- [1] W.R. Nelson, D.W.O. Rogers and H. Hirayama, The EGS4 Code System, Stanford Linear Accelerator report SLAC-265 (1985).
- [2] GEANT Detector Description and Simulation Tool, CERN Program Library Long Writeup, PHYS325 (1993).
- [3] H. Hirayama et al., The EGS5 Code System, SLAC-R-730 (2005) and KEK Report 2005-8 (2005).
- [4] G. Molière, *Z. Naturforsch.* **2a**, 133 (1947).
- [5] G. Molière, *Z. Naturforsch.* **3a**, 78 (1948).
- [6] H.A. Bethe, *Phys. Rev.* **89**, 1256 (1953).
- [7] S. Goudsmit and J. L. Saunderson, *Phys. Rev.* **57**, 24 (1940)
- [8] S. Goudsmit and J. L. Saunderson, *Phys. Rev.* **58**, 36 (1940)
- [9] H. W. Lewis, *Phys. Rev.* **78**, 526 (1950)
- [10] W.H. Press et al., *Numerical Recipes in C: The Art of Scientific Computing*, 2nd ed., Cambridge University Press (1992).
- [11] T.Ooura and M.Mori, *Journal of Computational and Applied Mathematics* **38**, 353 (1991).
- [12] T.Ooura and M.Mori, *Journal of Computational and Applied Mathematics* **112**, 229 (1999).
- [13] M. Mori and M. Sugihara, *Journal of Computational and Applied Mathematics* **127**, 287 (2001).
- [14] K. Okei and T. Nakatsuka, *Proc. 13th EGS Users' Meeting in Japan*, KEK Proceedings 2006-4, 28 (2006).
- [15] <http://www.kurims.kyoto-u.ac.jp/ooura/intde.html>
- [16] D. R. Yennie, D. G. Ravenhall and R. N. Wilson, *Phys. Rev.* **95**, 500 (1954)
- [17] N. Sherman, *Phys. Rev.* **103**, 1601, (1956)
- [18] D. Walter and V. Putte, *Nucl. Inst. Meth.* **115**, 117 (1974)

USE OF MESH TALLIES IN THE COMBINATORIAL GEOMETRY OF THE EGS5 CODE

T. Sugita¹, T. Torii²

¹Science and System Laboratory Ltd., Tomobe, Ibaraki 309-1716, Japan

²Tsuruga Head Office, Japan Atomic Energy Agency, Tsuruga, Fukui 914-8585, Japan

Abstract

To calculate the spatial distribution of radiation flux (dose), it is important to obtain the average flux in the evaluating areas. Then, the mesh tally (FMESH) that calculates the radiation flux in the evaluation areas is prepared in the MCNP5 code. We have developed a user-routine that calculate the 3-D mesh tallies, which can be used with the MCNP5, in a Combinatorial Geometrical version of the EGS5 code. We have also developed a supporting tool for users to use EGS code easily and to control the input making and execution by graphical interface (GUI).

1. Introduction

There is a need that obtains average fluence rates of the evaluating regions. There is mesh tallies in MCNP5 code to calculate the fluence rate. In the CG version of the EGS5 code, mesh tallies were not able to be calculated. We have developed a user-routine to calculate the mesh tallies in the EGS5 code. Conventionally, input data was made by the line command in the EGS5 code. Here, we have developed the interface code that controls the EGS5 calculation by using GUI.

2. A Mesh tally user-routine in EGS5

2.1 Definition of A track length tally.

A track length tally has used for definition a mesh tally. A track length tally is derived from that a particle tracking length divide a volume of evaluating region. A next is showing a definition of a track length tally.

```
=TRACKLENGHT_MESH
```

```
-10.0 10.0 20 -10.0 10.0 20 -10.0 10.0 20 0 1  
-3.0 3.0 6 -3.0 3.0 6 -3.0 3.0 6 0 2
```

```
=TRACKLENGHT_ENERGY
```

```
10  
0.001 1.0 2.0 3.0 4.0 5.0 6.0 7.0 8.0 9.0 10.0  
5  
1.05 1.15 1.25 1.35 1.45 1.55
```

2.2 How to build up a track length tally in the EGS5

The next lines have added in the last part of subroutine HOWFAR. This obtains a shut length from a boundary length of next region and a boundary length of a next mesh area.

```
call get_nextcloss(x(np),y(np),z(np),u(np),v(np),w(np),
&    umeshbnd,ustep)
if(umeshbnd.lt.ustep) then
  ustep = umeshbnd
  irnew= ir(np)
endif
```

The next lines have added in the subroutine AUSGAB..

```
if (iarg.eq.0) then
  if (ustep.ne.0.0) then
    if(iq(np).ne.0) then
      eeee=e(np)-PRM
    else
      eeee=e(np)
    end if
    call get_tracklength(ir(np),iq(np),eeee,
&      x(np),y(np),z(np),u(np),v(np),w(np),wt(np),
&      edep,ustep,tvstep)
  end if
endif
```

And the next subroutine has added in the EGS5 code.

```
subroutine get_tracklength(irnp,iqnp,enp,
&  xnp,ynp,znp,unp,vnp,wnp,wtnp,edepnp,ustepnp,tvstepnp)
implicit none
include include/egs5_h.f  ! Main EGS5 "header" file
integer MXTRACKENG,MXTRACKENGNO,MXTRACKREG
parameter (MXTRACKENG = 120, MXTRACKENGNO = 5, MXTRACKREG=10000)
integer imp,iqnp
real*8 enp,xnp,ynp,znp,unp,vnp,wnp,wtnp,
&  edepnp,ustepnp,tvstepnp
common/com1t/tverg(MXTRACKENG+1,MXTRACKENGNO),
& tvtbl(MXTRACKENG+1,MXTRACKREG),tvvol(MXTRACKREG),
&  tverr(MXTRACKENG+1,MXTRACKREG),
&  itverg(MXTRACKENGNO),
```

```

& itvtbl(MXTRACKREG),ntrackreg(MXTRACKREG),ntverg
real*8  tverg,tvtbl,tvol,tverr
integer itverg,itvtbl,ntrackreg,ntverg
common/comtlp/tvxs(MXTRACKREG),tvxe(MXTRACKREG),
&          tvys(MXTRACKREG),tvye(MXTRACKREG),
&          tvzs(MXTRACKREG),tvze(MXTRACKREG),
&          mtvx(MXTRACKREG),mtvy(MXTRACKREG),
&          mtvz(MXTRACKREG),iqtv(MXTRACKREG),
&          iptv(MXTRACKREG),nowrg(MXTRACKREG),itrackreg
real*8  tvxs,tvxe,tvys,tvye,tvzs,tvze
integer mtvx,mtvy,mtvz,iqtv,iptv,nowrg,itrackreg
common/compdsig/pdsig(MXREG)
real*8  pdsig,sigpd
integer i,ii,ie
integer ignmed
real*8  sig
real*8  edepwt          ! Local variables
ignmed = 0
edepwt = edepnp*wtnp
if(itrackreg.ne.0) then
  call add_meshflux(iqnp,enp,xnp,ynp,znp,unp,vnp,wnp,wtnp,
&                  tvstepnp,ustepnp)
end if
return
end
subroutine add_meshflux(iq,e,x,y,z,u,v,w,wt,tvstep,ustep)
implicit none
include 'include/egs5_h.f          ! Main EGS5 "header" file
include 'include/user_cg/cghead.f
include 'include/user_cg/source_common.f
integer MXTRACKENG,MXTRACKENGNO,MXTRACKREG
parameter (MXTRACKENG = 120, MXTRACKENGNO = 5, MXTRACKREG=10000)
real*8  e,x,y,z,u,v,w,wt,tvstep,ustep
integer iq
common/comtlp/tverg(MXTRACKENG+1,MXTRACKENGNO),
&          tvtbl(MXTRACKENG+1,MXTRACKREG),tvvol(MXTRACKREG),
&          tverr(MXTRACKENG+1,MXTRACKREG),
&          itverg(MXTRACKENGNO),
&          itvtbl(MXTRACKREG),ntrackreg(MXTRACKREG),ntverg
real*8  tverg,tvtbl,tvol,tverr
integer itverg,itvtbl,ntrackreg,ntverg

```

```

common/comt1p/tvxs(MXTRACKREG),tvxe(MXTRACKREG),
&          tvys(MXTRACKREG),tvye(MXTRACKREG),
&          tvzs(MXTRACKREG),tvze(MXTRACKREG),
&          mtvx(MXTRACKREG),mtvy(MXTRACKREG),
&          mtvz(MXTRACKREG),iqtv(MXTRACKREG),
&          iptv(MXTRACKREG),
&          nowrg(MXTRACKREG),itrackreg
real*8  tvxs,tvxe,tvys,tvye,tvzs,tvze
integer mtvx,mtvy,mtvz,iqtv,iptv,nowrg,itrackreg
real*8  xx,yy,zz
integer i,k,kk,n
if(itrackreg.eq.0) then
  return
endif
xx=x+u*ustep/2.0d0
yy=y+v*ustep/2.0d0
zz=z+w*ustep/2.0d0
call get_nowreg(xx,yy,zz)
do 200 i=1,itrackreg
  if(nowrg(i).ne.0) then
    if(iq.eq.iqtv(i)) then
      if(i.eq.1) then
        n=nowrg(i)
      else
        n=ntrackreg(i-1)+nowrg(i)
      endif
      kk = 0
      do 120 k=1,itverg(iptv(i))
        if(e.ge.tverg(k,iptv(i)).and.
&          e.lt.tverg(k+1,iptv(i))) then
          kk=k
          go to 140
        end if
120      continue
        if(e.eq.tverg(itverg(iptv(i))+1,iptv(i))) then
          kk=itverg(iptv(i))
        endif
140      continue
        if(kk.ne.0) then
          tvtbl(kk,n)=tvtbl(kk,n)+tvstep*wt/tvvol(n)
          tverr(kk,n)=tverr(kk,n)+tvstep*wt/tvvol(n)

```

```

        tvtbl(MXTRACKENG+1,n)=tvtbl(MXTRACKENG+1,n)
&
        +tvstep*wt/tvvol(n)
        tverr(MXTRACKENG+1,n)=tverr(MXTRACKENG+1,n)
&
        +tvstep*wt/tvvol(n)
    endif
endif
endif
200 continue
return
end

```

2.3 A sample output of a track length tally.

(1) The calculating condition.

Geometry: Air region 200x200x200[cm] .around 25[cm] of concrete wall.

center is (0,0,0), there are phantom and concrete brock.

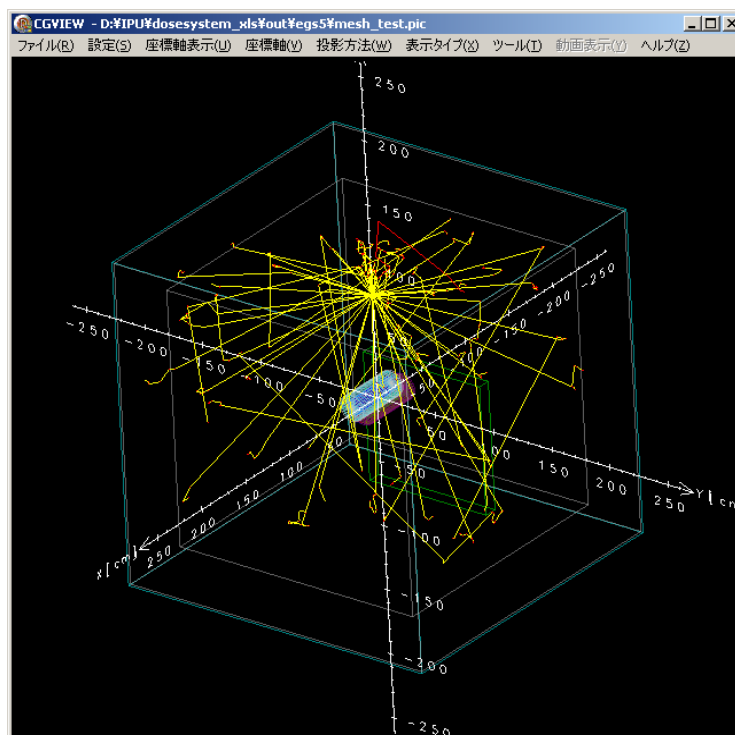
Source: 1[MeV] of photon , position of beam is (0,0,80.0), isotropic point source.

Number of source particle : 1000000

Mesh : X -125.0 ~ 125.0 50division 1mesh=5[cm]

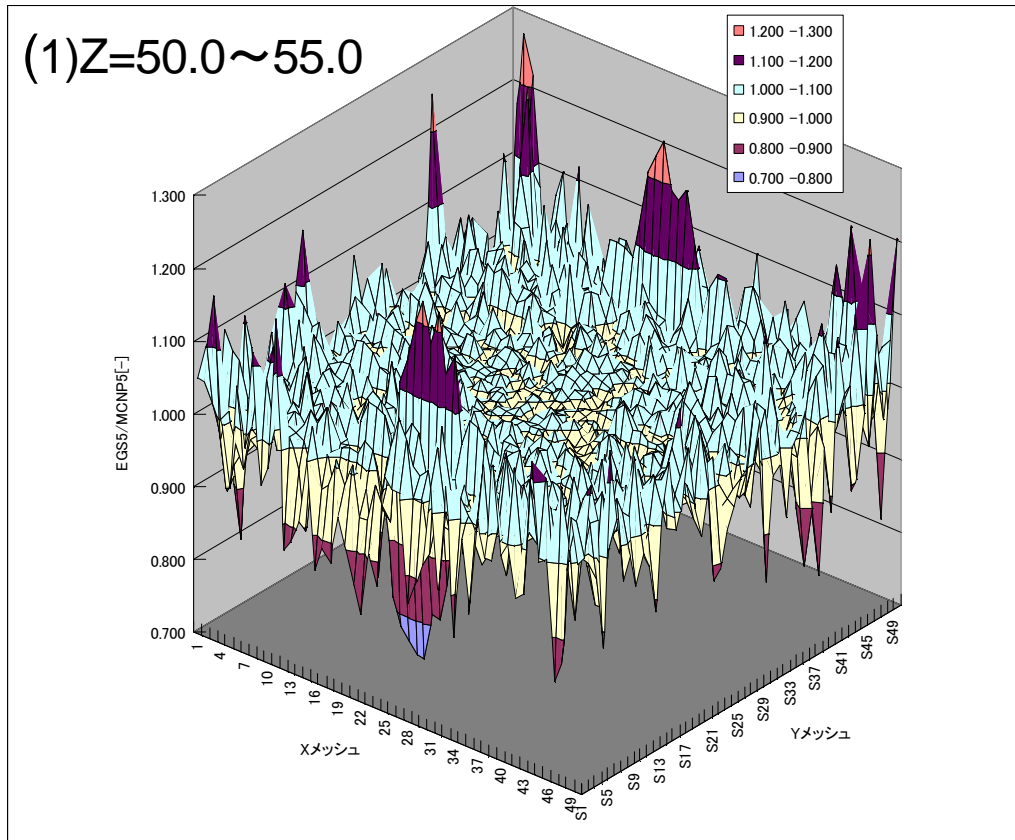
Y -125.0 ~ 125.0 50division 1mesh=5[cm]

Z -125.0 ~ 125.0 50division 1mesh=5[cm]

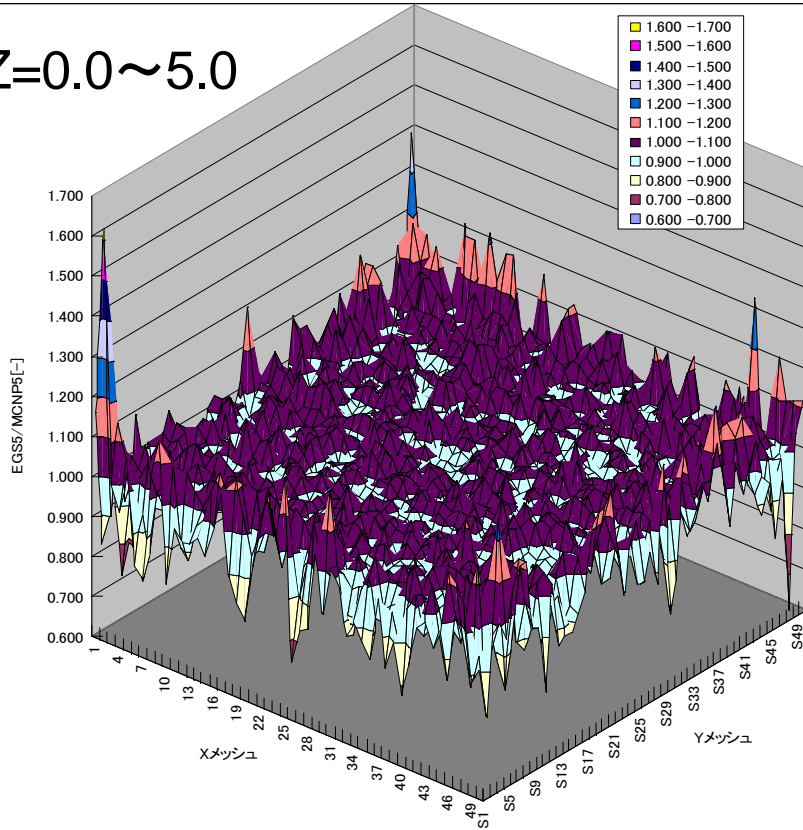


(2) The output of the calculation.

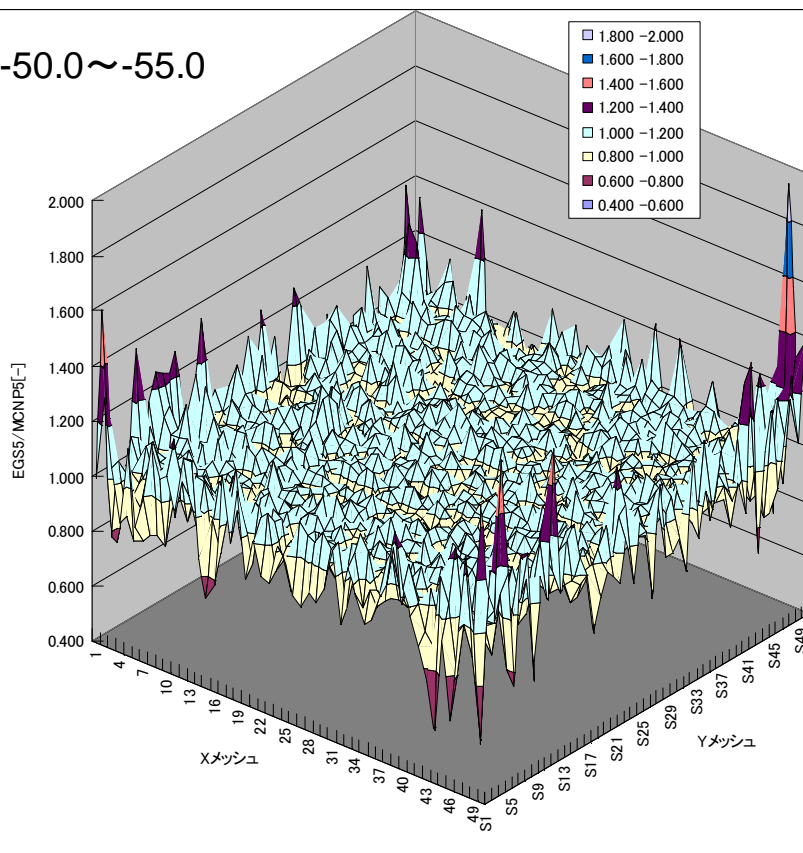
Next, the comparison of the calculation results by the EGS code and the MCNP code is shown. Ratios (EGS5/MCNP5) in an arbitrary Z axis section are shown below. It is convergent in the air areas within 20% though the ratio of EGS5/MCNP5 becomes large (max. factor 2) in the outside concrete area because convergent is insufficient.



(2) Z=0.0~5.0



(3) Z=-50.0~-55.0



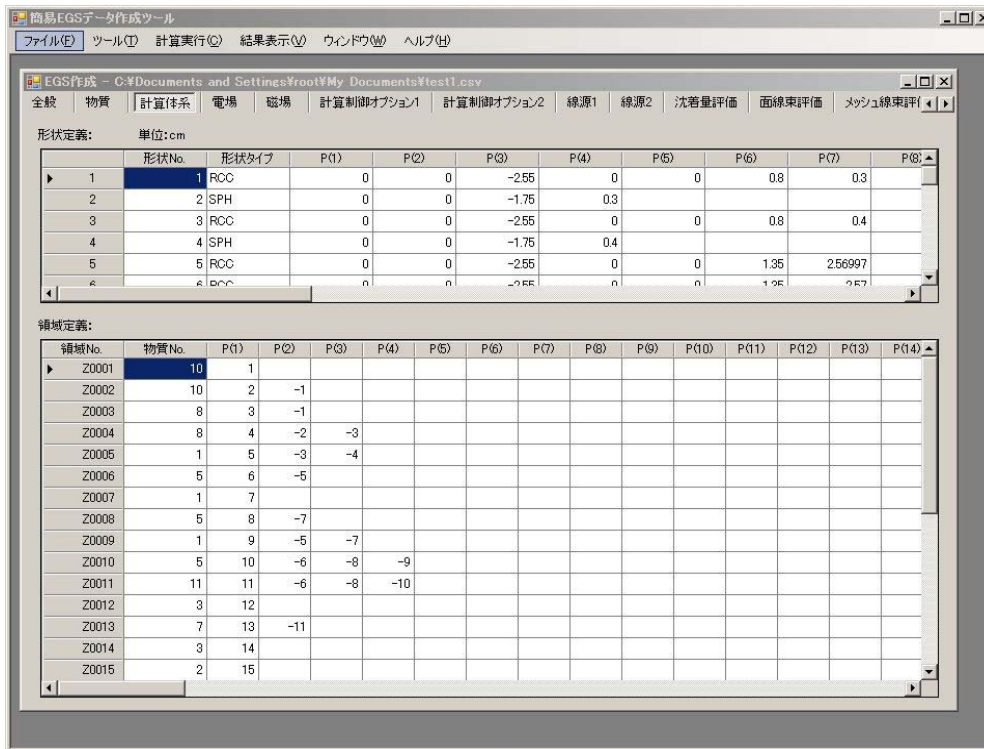
3. GUI driver System for EGS5 calculation.

3.1 Purpose of developed GUI driver system.

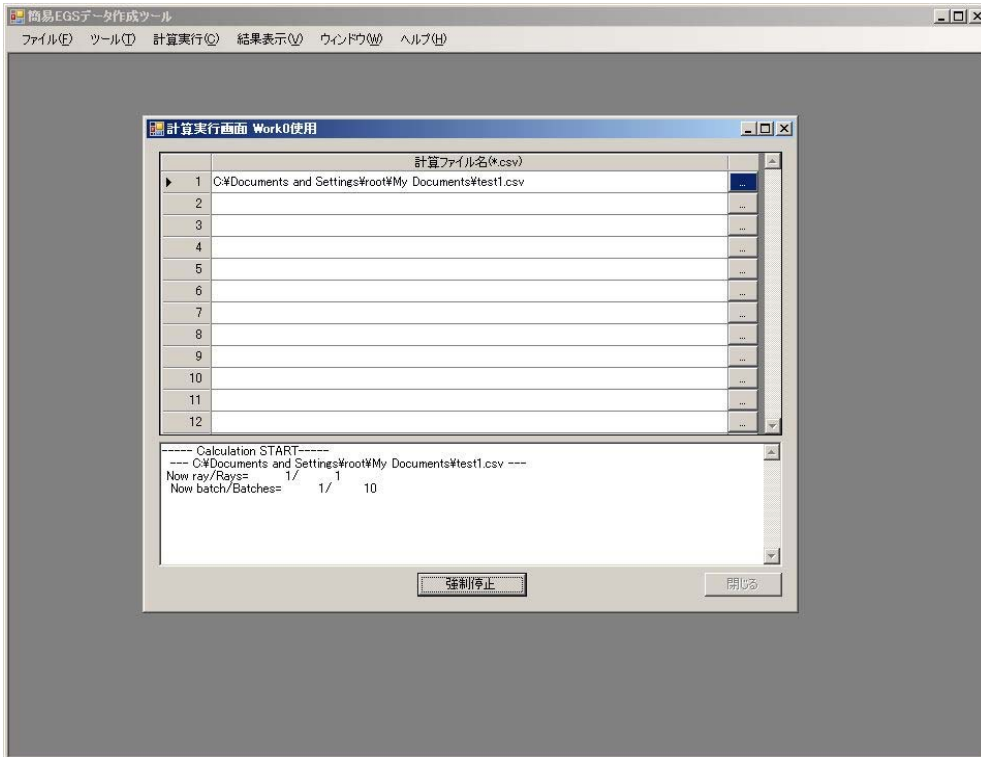
We have developed a user code of EGS5 that can be calculated without compile at runtime. In the code, calculation parameters are setting in a SYSIN file. Here we have developed an interface code that controls the EGS5 calculation by using GUI. The language used is C#, and running OS is windows XP or late.

3.2 Feature of GUI driver system.

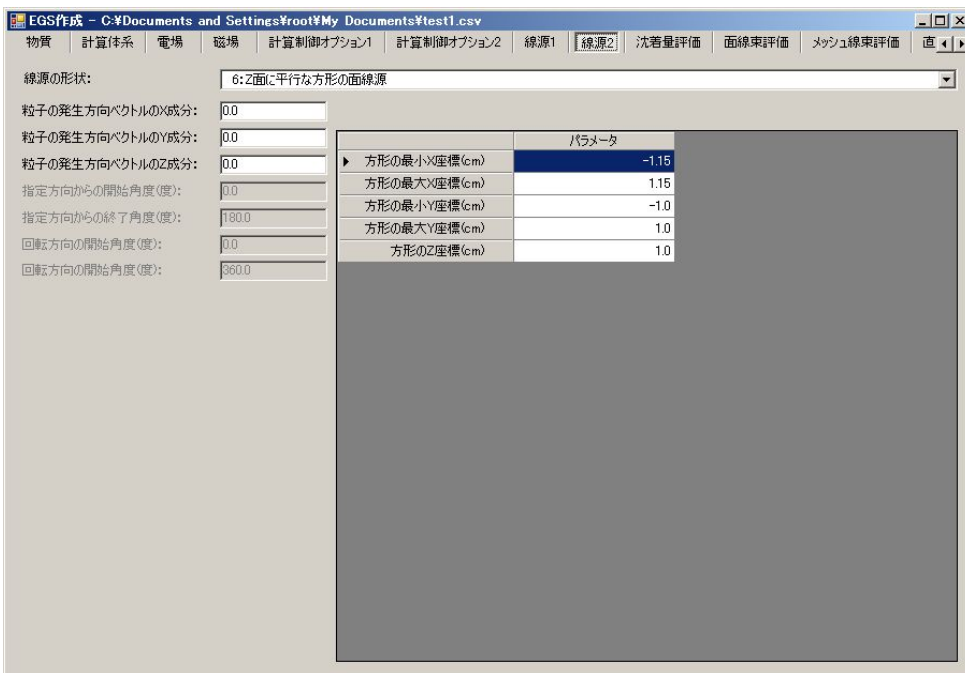
- It has many source pattern and tally pattern then it is making easily a input data of EGS5 by GUI.
- It is running a EGS5 code By GUI.
- It can show CG geometry and source area and direction..
- It can output the result tables.



input viewing surface



executing viewing surface



source definition viewing surface

評価タリー

EGS作成 - C:\Documents and Settings\root\My Documents\test1.csv

物質 計算体系 電場 磁場 計算制御オプション1 計算制御オプション2 線源1 線源2 沈着量評価 面線束評価 **メッシュ線束評価** 直

メッシュ線束評価: 行う

No.	評価粒子	評価エネルギー	X下限範囲[cm]	X上限範囲[cm]	X分層数	Y下限範囲[cm]	Y上限範囲[cm]	Y分層数	Z下限範囲[cm]	Z上限範囲
▶ 1	光子	1	-100	100	10	-100	100	10	-100	-100
2	陽電子	2	-100	100	20	-100	100	5	-100	-100

評価エネルギー-1: 4 評価エネルギー-2: 4 評価エネルギー-3: 0

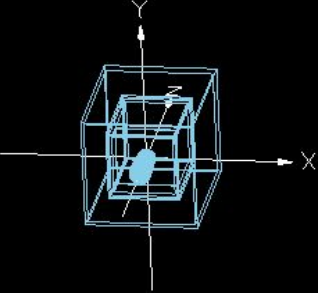
境界No.	境界エネルギー(MeV)
▶ 1	0.001
2	0.01
3	0.1
4	1.0
5	10.0

境界No.	境界エネルギー(MeV)
▶ 1	0.001
2	0.01
3	0.1
4	1.0
5	10.0

境界No.	境界エネルギー(MeV)
▶ 1	0.001
2	0.01
3	0.1
4	1.0
5	10.0

tally definition viewing surface

体系の整合性確認



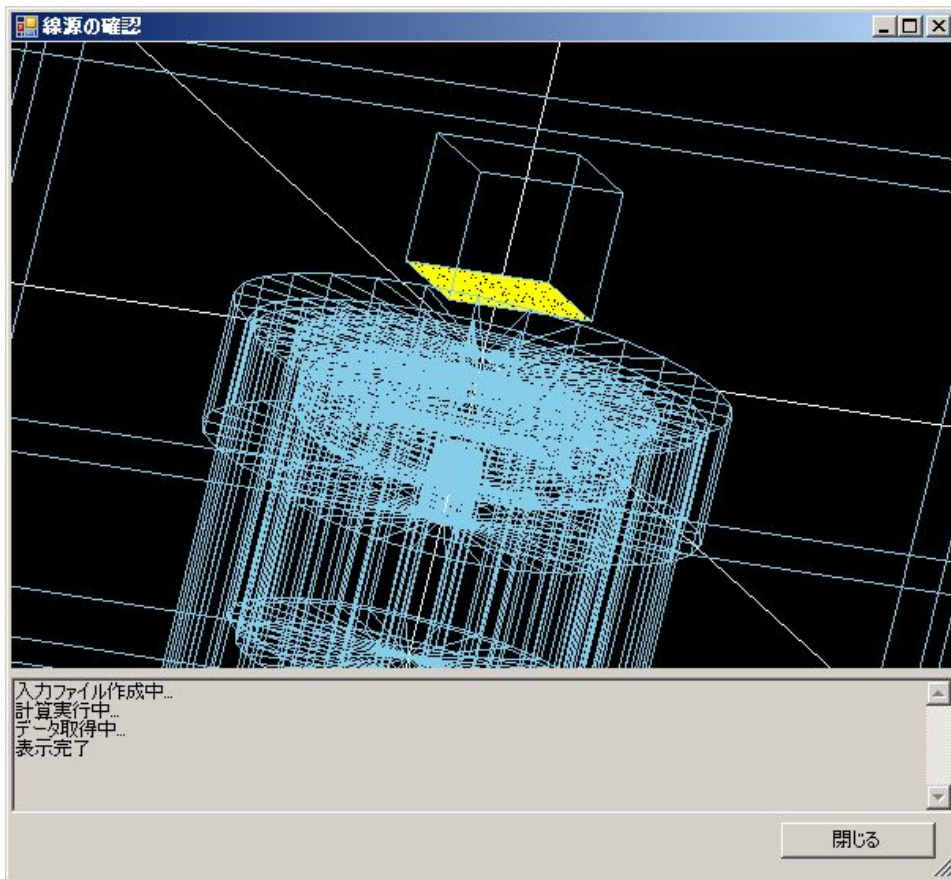
走査数: 10000 始点座標(X,Y,Z): 0.0 0.0 0.0

走査状況: 695/10000

Point(2.23E-1,1.22E-1,-1.82E+0)で領域が定義されていません。
 Point(-2.22E-1,-1.45E-1,-1.81E+0)で領域が定義されていません。
 Point(-1.15E-1,-2.49E-1,-1.80E+0)で領域が定義されていません。
 Point(-5.79E-2,2.68E-1,-1.80E+0)で領域が定義されていません。

中止 閉じる

consistency check viewing surface



source check viewing surface

表示するファイル: C:\Documents and Settings\root\My Documents\test1.out

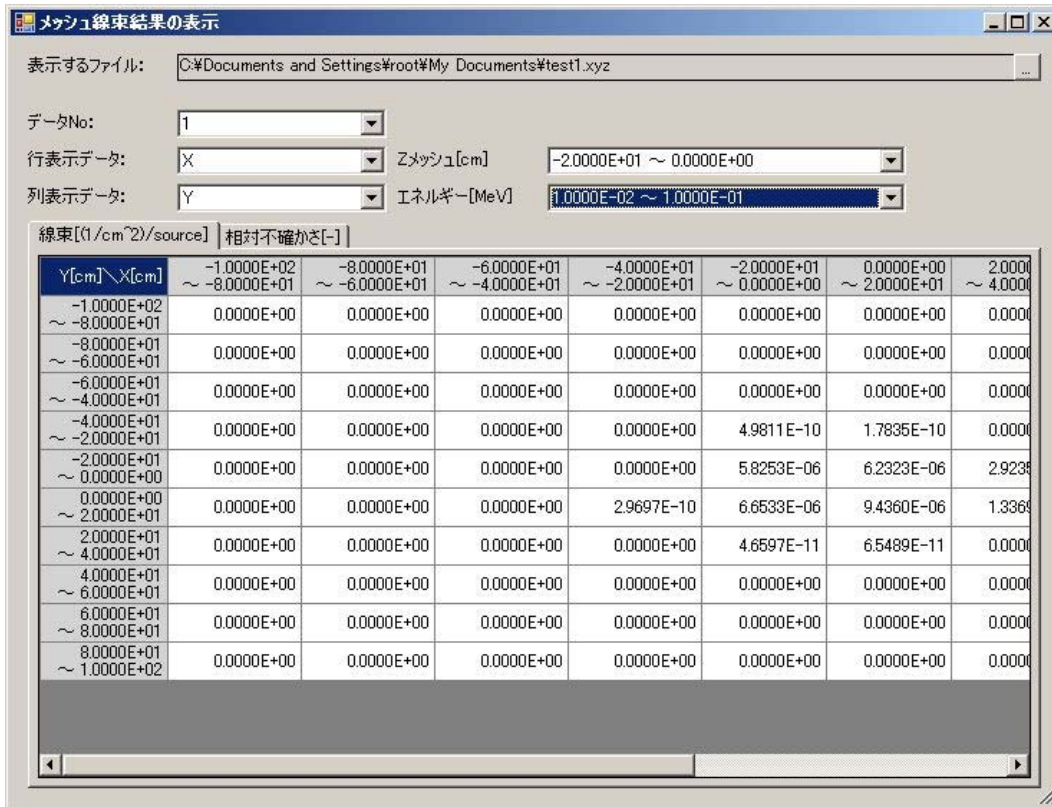
表示データ: 沈着量(エネルギー毎カウ)

評価対象: 領域

評価情報:
粒子数[Source Particles]=10000 線源[Source]=CO-60

エネルギーNo.	エネルギー [MeV]	領域No. 1	領域No. 5
▶ 1	0.005000	0.0000E+00	6.0000E-04
2	0.010000	0.0000E+00	2.0000E-04
3	0.015000	0.0000E+00	6.0000E-04
4	0.020000	0.0000E+00	4.0000E-04
5	0.025000	0.0000E+00	6.0000E-04
6	0.030000	0.0000E+00	6.0000E-04
7	0.035000	0.0000E+00	1.1990E-03
8	0.040000	0.0000E+00	6.0000E-04
9	0.045000	0.0000E+00	9.9900E-04
10	0.050000	0.0000E+00	4.0000E-04
11	0.055000	0.0000E+00	6.0000E-04
12	0.060000	0.0000E+00	9.9900E-04
13	0.065000	0.0000E+00	9.9900E-04

result table viewing surface



result mesh tally viewing surface

4. Conclusions

We have developed the user-routine that calculate the mesh tallies with a CG (Combinatorial Geometry) in the EGS5 code. We also have developed the interface code that controls the EGS5 calculation by using GUI.

Acknowledgments

We are grateful to Prof. H. Hirayama and Dr. Y. Namito of KEK for their encouragement of this work.

References

- 1) W.R. Nelson, H. Hirayama, and D.W.O. Rogers, SLAC-265 (1985).
- 2) T. Torii, and T. Sugita, Development of PRESTA-CG Incorporating Combinatorial Geometry in EGS4/PRESTA, JNC TN1410 2002-001 (2002).

Development of Monte Carlo dose verification system for MHI-TM2000

**Y. Ishihara^{1,2}, A. Sawada¹, M. Nakamura¹, S. Kaneko³,
K. Takayama¹, T. Mizowaki¹, M. Kokubo⁴, M. Hiraoka¹**

¹*Department of Radiation Oncology and Image-applied Therapy, Kyoto University Graduate School of Medicine*

²*Research Fellow of the Japan Society for the Promotion of Science*

³*Medical Systems Engineering Section, Mitsubishi Heavy Industries, Ltd.*

⁴*Division of Radiation Oncology Institute of Biomedical Research and Innovation*

e-mail: y.ishi@kuhp.kyoto-u.ac.jp

1. Introduction

MHI-TM2000 (Mitsubishi Heavy Industries, Ltd., Japan) is an innovative image-guide radiotherapy (IGRT) system employing a C-band X-ray head with gimbal mechanics, two sets of kV X-ray tubes and flat panel detectors mounted on an O-ring shaped gantry, an electronic portal imaging device, an infrared camera system, and a robotic treatment couch with six degrees of freedom [1,2]. This IGRT system has a capability of pursuing irradiation for a moving target using real-time imaging and real-time active beam adaptation, this is, four-dimensional radiotherapy. We are developing an integrated Monte Carlo (MC) dose calculation system as a routine verification tool of four-dimensional radiotherapy. The purposes of this study were to propose specific MC models of the X-ray head and the multi-leaf collimator (MLC) for MHI-TM2000 and to validate their accuracy.

2. Materials and Methods

6 MV photon beam delivered by the MHI-TM2000 unit at our hospital was simulated using EGSnrc/BEAMnrc and EGSnrc/DOSXYZnrc codes. Subsequently, the X-ray head composed of a target, a primary collimator, a flattening filter, a monitor chamber, a fixed secondary collimator, and a MLC was simulated based on the specification. The MLC is of the single focus type and has 30 pairs of leaves of 5 mm thickness at the isocenter with a maximum field size of 15 x 15 cm². Figure 1 shows the geometric schema of the MHI-TM2000 model. Next, the central axis depth doses and the lateral doses at 15, 100, and 200 mm depth were simulated under the source to surface distance (SSD) of 900 mm. Central axis depth doses were normalized to the dose at 100 mm depth for a MLC open field of 15 x 15 cm² while the lateral ones were normalized to the dose at 15 mm depth. Then, Each of them was compared with the corresponding measurement using a CC06 ionization chamber and a water phantom.

In terms with the MLC model, the static tests for Tongue-and-Groove (T&G) effect, leaf leakage, and round leaf effect (5 x 5, 10 x 10, and 15 x 15 cm²) were simulated employing well-commissioned phase space data (PSD) in the head model. Figure 2 illustrates the MLC patterns for each test, respectively. On the other hand, film measurements were performed using Kodak EDR2 film with a solid water phantom under similar conditions. The measured doses were normalized to the dose at each test's depth (leakage: 50 mm depth dose with SSD of 950 mm, T&G and round leaf: 100 mm depth dose with SSD of 900 mm) for the MLC open field, respectively. The differences between simulated and measured doses were calculated.

3. Results

Figure 3 represents the central axis depth dose profiles with the MLC fully opened. The simulated depth doses beyond the buildup point gave agreement of within 1.0%. Figure 4 depicts the simulated and the measured lateral dose profiles. The simulated lateral doses, except for around the penumbra, agreed to within 1.3% for all depth. T&G profiles are shown in Fig. 5. The averaged differences between the simulated and the measured doses were 2.7% and the simulated profile compared well with the measured one.

The differences between the simulated and the measured doses agreed less than 3.0% for both the leaf leakage (Fig. 6) and the round leaf effect (Fig. 7).

4. Conclusions

We have developed specific MC models of the X-ray head and the MLC for MHI-TM2000. From the result, it is concluded that our MC models have reasonable accuracy, suggesting that the dose calculation of pursuing irradiation for a moving target may be feasible with the proposed MC models.

References

- 1) Kamino Y, Takayama K, Kokubo M, et al.: Development of a four-dimensional image-guided radiotherapy system with a gimbaled X-ray head, *Int J. Radiation Oncology Biol. Phys.* 66, 271-278, 2006.
- 2) Kamino Y, Miura S, Kokubo M, et al.: Development of an ultrasmall C-band linear accelerator guide for a four-dimensional image-guided radiotherapy system with a gimbaled x-ray head, *Med. Phys.* 34, 1797-1808, 2007. Intensity Modulated Radiation Therapy Collaborative Working Group, "Intensity-modulated radiotherapy: Current status and issues of interest," *Int. J. Radiat. Oncol., Biol., Phys.* **51**, 880-914 (2001).

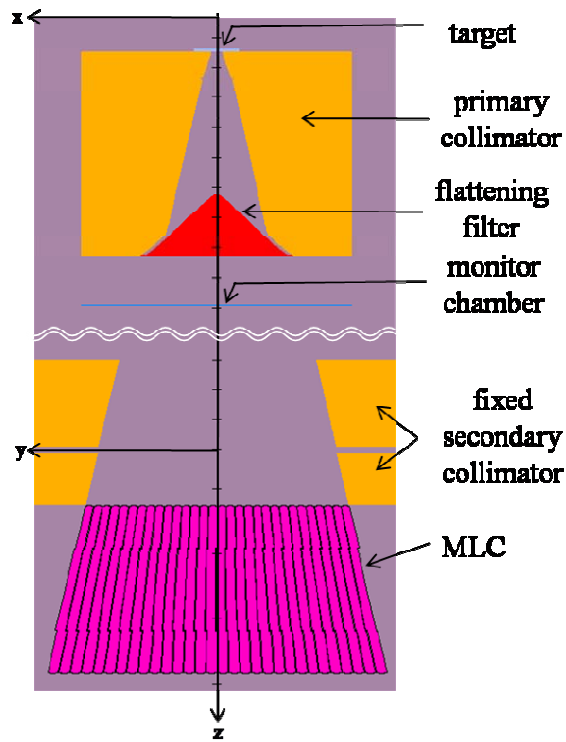


Figure 1 Geometric schema of the X-ray head and MLC components. Lower fixed secondary collimator and MLC are rotated by 90 degrees.

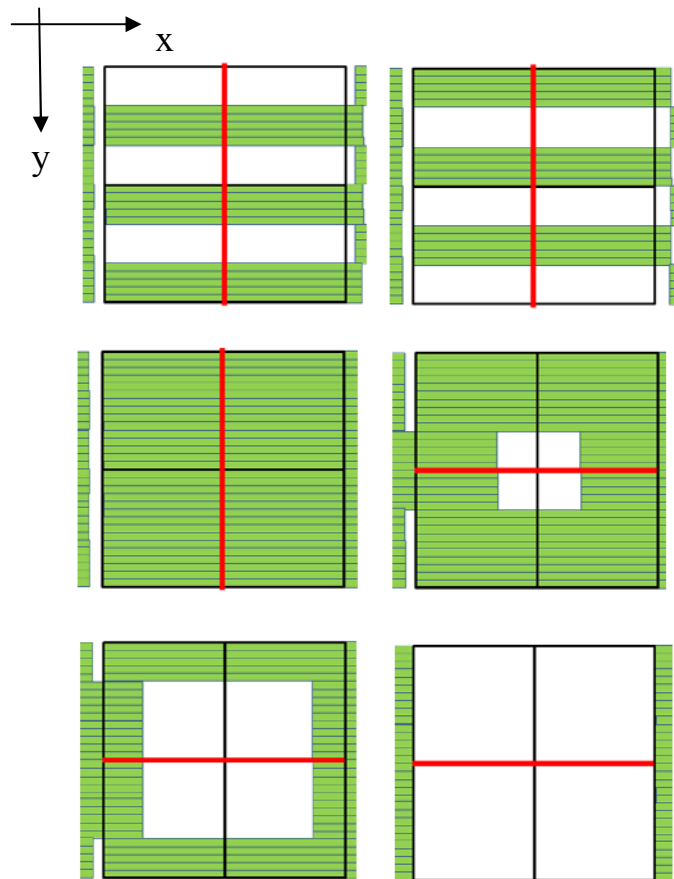


Figure 2 MLC patterns for each test. Red lines depict profile lines. T&G profiles are simulated by combining (a) with (b). (c) shows a leaf leakage pattern. Round leaf profiles are calculated for (d) $5 \times 5 \text{ cm}^2$, (e) $10 \times 10 \text{ cm}^2$, and (f) $15 \times 15 \text{ cm}^2$.

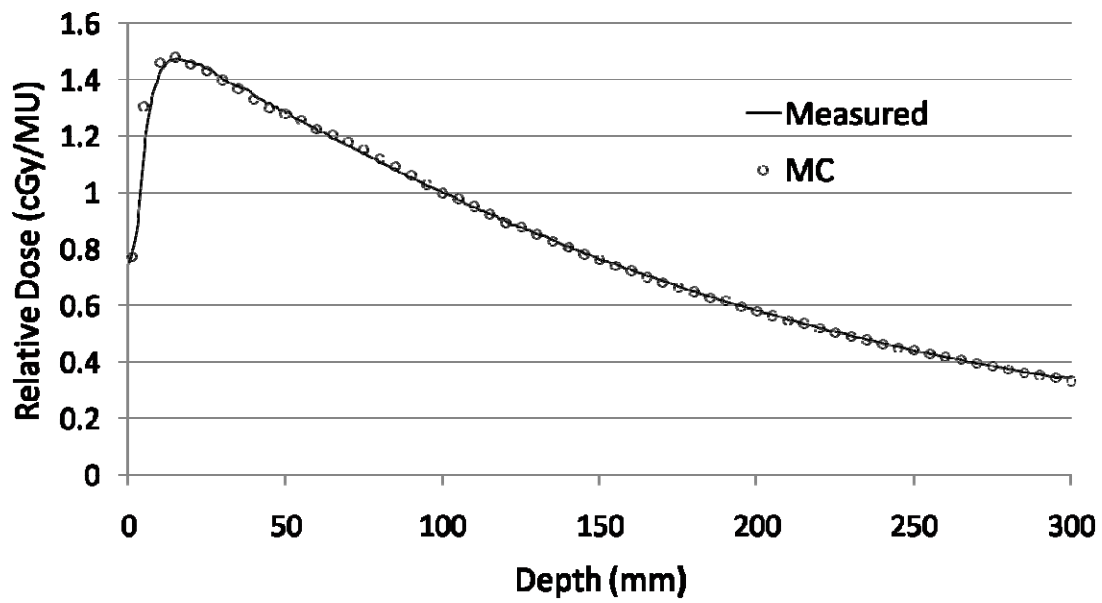


Figure 3 Depth dose profiles for the simulated doses with a resolution of $0.5 \times 0.5 \times 0.5 \text{ cm}^3$ and the measured doses.

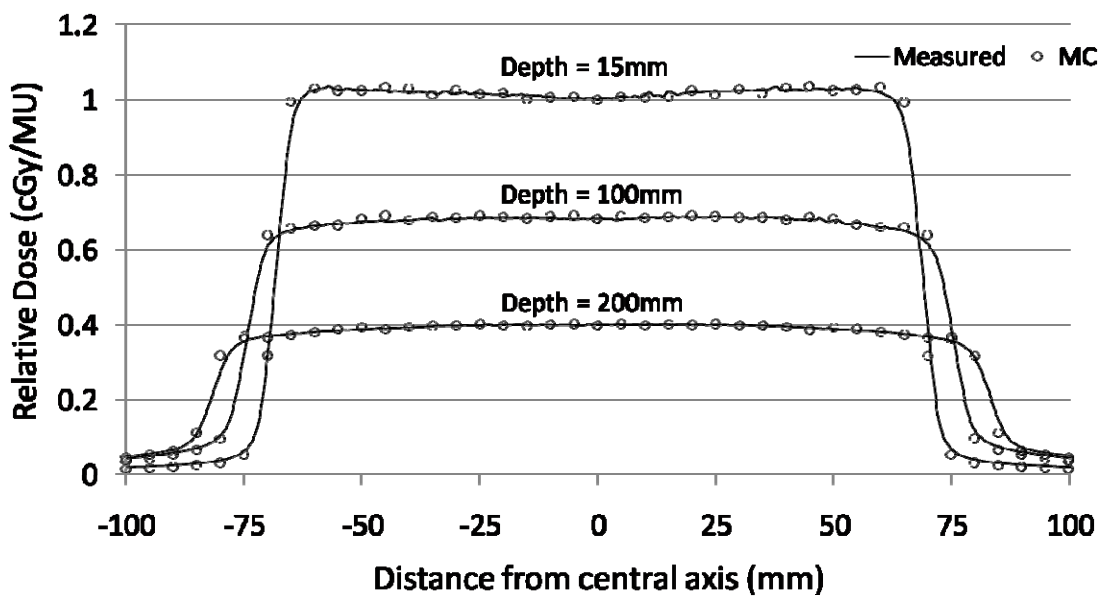


Figure 4 Lateral dose profiles as a function of distance from the central axis for the simulated doses with a resolution of $0.5 \times 0.5 \times 0.5 \text{ cm}^3$ and the measured doses at 15 mm, 100 mm, and 200 mm depth, respectively.

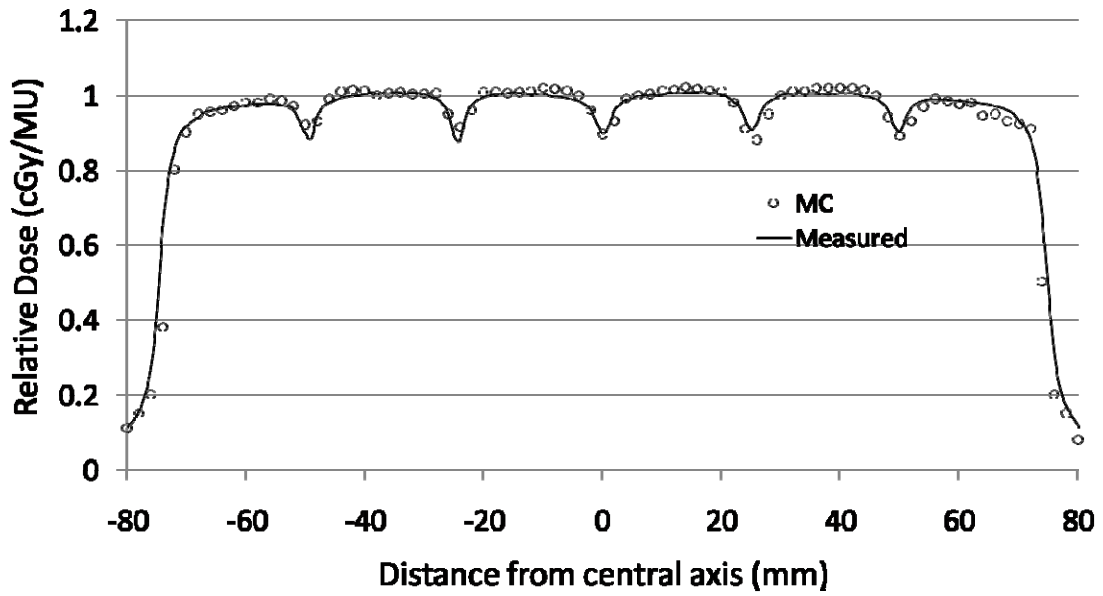


Figure 5 T&G profiles as a function of distance from the central axis for the simulated doses with a resolution of $0.3 \times 0.2 \times 0.3 \text{ cm}^3$ and the measured doses.

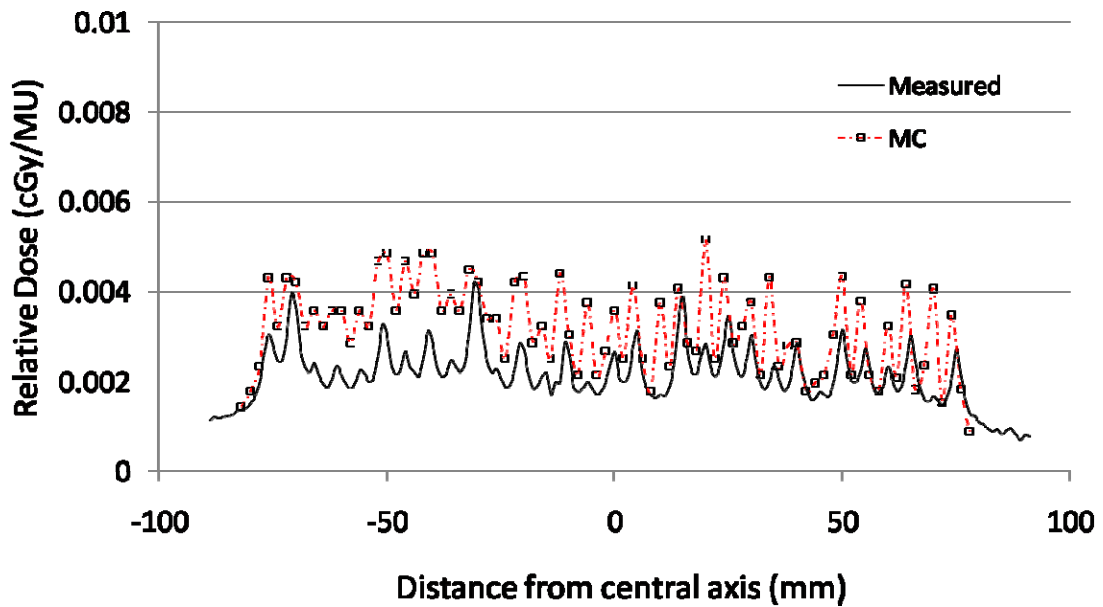


Figure 6 Leaf leakage profiles as a function of distance from the central axis for the simulated doses with a resolution of $0.3 \times 0.2 \times 0.3 \text{ cm}^3$ and the measured doses.

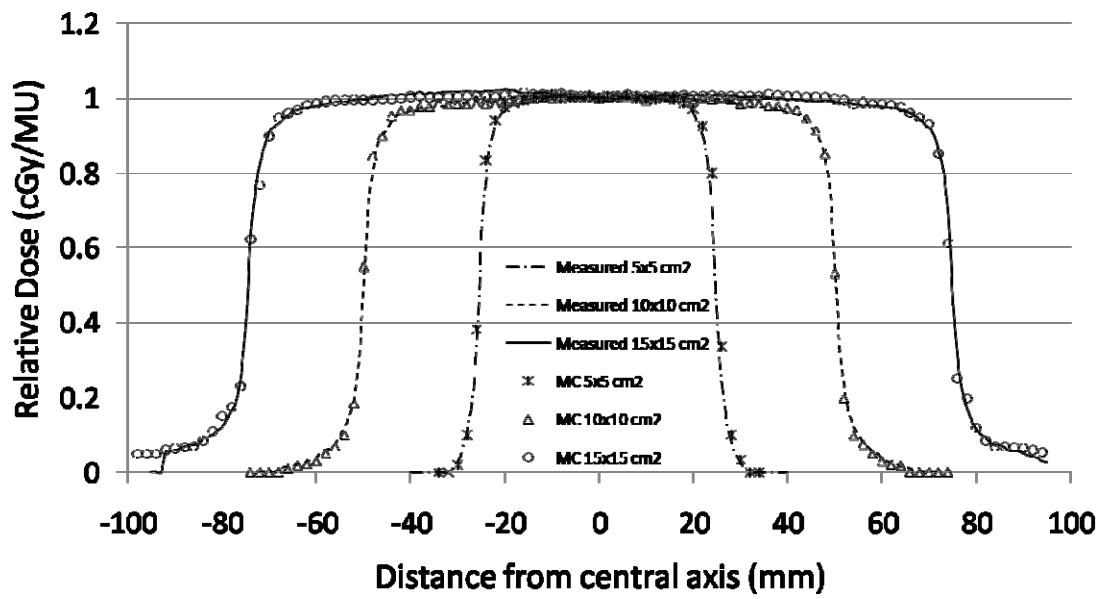


Figure 7 Round leaf profiles as a function of distance from the central axis for the simulated doses with a resolution of $0.2 \times 0.3 \times 0.3 \text{ cm}^3$ and the measured doses.

Dose characteristics of the ^{125}I seeds for Prostate Brachytherapy

T. Matsunaga, N. Kataoka¹, K. Yasui², T. Shimozato³, H. Fuse, Y. Oribe, Y. Igarashi,
M. Komori³, and Y. Obata³

*Department of Radiological Technology, Graduate School of Medicine, Nagoya University
1-1-20 Daikou-Minami, Higashi-ku, Nagoya, Japan*

¹ *Anjo Kosei Hospital*

² *Health & Welfare Bureau, City of Nagoya*

³ *Department of Radiological Technology, School of Health Science, Nagoya University*

E-mail: matsunaga.takuma@h.mbox.nagoya-u.ac.jp

Abstract

In Japan, two ^{125}I brachytherapy sources, the Amersham Health model 6711 and the SourceTech Medical model STM1251, are used for the treatment of prostate cancer. Because of the differences of the external geometry and the internal material between two sources, the dose characteristics are also different. We calculated the photon energy spectra, the radial dose function, and the anisotropy function of two sources using Monte Carlo (MC) simulation. The photon energy spectra of the 6711 included characteristic X-rays from the internal rod (Ag), but that of the STM1251 didn't include characteristic X-rays from the internal rod (Au). The discrepancies of the radial dose function between two ^{125}I sources ranged from -3.2 to 3.0 %. The discrepancy of the anisotropy function between two ^{125}I sources was -24.6 % (5°), and ranged from -4.0 to 5.3 % ($> 10^\circ$). It seems that these discrepancies were derived from existence or nonexistence of characteristic X-rays from the internal rod and the differences of the geometry of Ti capsule.

1. Introduction

An interstitial brachytherapy is a form of direct implantation of radioactive sources into cancerous tissue. The numbers of ^{125}I brachytherapy source models and their clinical use have increased. In Japan, the Amersham Health model 6711 and the SourceTech Medical model STM1251 are used for the treatment of prostate cancer. These source models have a similar external geometry, with nearly identical outer dimensions. The internal active material of these sources is in the form of cylindrical rods (silver, gold), coated with a radioactive layer. The internal structures and the source encapsulation can cause the significant absorption and the scattering of low-energy photons.

Using a full set of the AAPM's Task Group 43 (TG-43) [1-3] dose calculation formalism, the absorbed dose rate in water, $D(r,\theta)$, at location (r,θ) relative to the source center and the longitudinal axis is given by

$$D(r,\theta) = S_k \Lambda \frac{G(r,\theta)}{G(r_0,\theta_0)} F(r,\theta) g(r)$$

where S_k is the measured air-kerma strength of the source in units of U, Λ is the dose rate constant, $G(r,\theta)$ is the geometry function, $F(r,\theta)$ is the anisotropy function, $g(r)$ is the radial dose function, and $(r_0,\theta_0)=(1 \text{ cm},\pi/2)$ is the reference point on the source transverse axis where $F(r,\theta)$ and $g(r)$ are normalized to unity.

In this study, the photon energy spectra, $F(r,\theta)$, and $g(r)$ were calculated using Monte Carlo (MC) simulation and compared between two ^{125}I sources to evaluate differences of the source geometry and material.

2. Materials and Methods

MC calculations were performed using EGS 5 code [4]. The cut-off energies for the transport calculation of electron (ECUT) and photon (PCUT) in all simulation were set to 512 and 1 keV, respectively. Statistical uncertainties were less than 1.0 % at the reference point.

2.1 ^{125}I seeds modeling

The design of the 6711 source is presented in Fig.1 (a). The 6711 source consists of a cylinder of silver coated with a radioactive iodine layer and encased inside a cylindrically symmetric titanium capsule of the radial thickness of 0.07 mm and semispherical end-caps [5]. The design of the STM1251 source is presented in Fig.1 (b). A layer of the radioactive iodine is deposited on top of thin copper layer, which, in turn, is deposited upon a nickel-coated aluminum cylinder. This cylinder contains a cylindrical gold core. The titanium capsule has the radial thickness of 0.08 mm and 0.13 mm thick end-caps [6]. The ^{125}I spectrum needed for MC calculations was taken from NuDat (Table 1) [7].

2.2 Photon energy spectra

The photon energy spectra of the two ^{125}I sources in vacuum at reference point were calculated. In the MC calculation, the photon energy spectra for the each source were scored in 0.1 keV bins.

2.3 TG-43 dosimetry parameters

$g(r)$ is the radial dose function that accounts for the radial dependence of the photon absorption and scatter in the medium along the transverse axis ($\theta=\pi/2$). The radial dose function $g(r)$ can be obtained as

$$g(r) = \frac{D(r, \theta_0) G(r_0, \theta_0)}{D(r_0, \theta_0) G(r, \theta_0)}$$

$F(r, \theta)$ is the anisotropy function that accounts for the angular dependence of the photon absorption and scatter in the encapsulation and the medium. The anisotropy function $F(r, \theta)$ can be obtained as

$$F(r, \theta) = \frac{D(r, \theta) G(r, \theta_0)}{D(r, \theta_0) G(r, \theta)}$$

In this study, $g(r)$ and $F(r, \theta)$ ($r = 0.5, 1.0, 2.0$ cm) of the two ^{125}I sources were calculated. The discrepancies between two ^{125}I sources were calculated as $((6711 - \text{STM1251}) / \text{STM1251}) \times 100$ (%).

3. Results and Discussions

3.1 Photon energy spectra

Fig.2 (a)-(b) shows the photon energy spectra of the 6711 and the STM1251, respectively. Each photon energy spectra included 5 keV Ti K X-rays. The photon energy spectra of the 6711 included 20 - 25 keV characteristic X-rays from the internal rod (Ag), but that of the STM1251 didn't include characteristic X-rays from the internal rod (Au). This is because Au characteristic X-rays were absorbed in high Z materials consisting the STM1251 such as Al, Ni, Cu, and Ti. Fig.3 (a)-(d) shows the absorbed energy spectra of Al, Ni, Cu, and Ti, respectively. These absorbed energy spectra included 10 - 15 keV Au L X-rays.

3.2 Radial dose function : $g(r)$

Fig.4 (a)-(b) shows the radial dose function $g(r)$ of the 6711 and the STM1251, respectively. There were good agreement in comparing the $g(r)$ to reference [2][3] in the results of both the 6711 and the STM1251. Fig.5 shows the comparing of the $g(r)$ between two ^{125}I sources. There was difference in the gradient of the $g(r)$. The discrepancies between two ^{125}I sources ranged from -3.2 to 3.0 %. It seems that the differences of the photon energy spectrum for the

sources effect to the $g(r)$.

3.3 Anisotropy function : $F(r, \theta)$

Fig.6 (a)-(b) shows the anisotropy function of the 6711 and the STM1251. There were good agreement in comparing the $F(r, \theta)$ to reference [2][3] in the results of both the 6711 and the STM1251. Fig.7 shows the comparing of $F(r, \theta)$ ($r = 1\text{cm}$) between two ^{125}I sources. For angles $\leq 10^\circ$, the maximum discrepancies between two ^{125}I sources were -24.6% (5°), and for angles $>10^\circ$, the discrepancies ranged from -4.0% to 5.3% . It seems that the differences of the geometry of Ti capsule effect to the anisotropy function: the 6711 has semispherical end-caps and the STM1251 has plate end-caps.

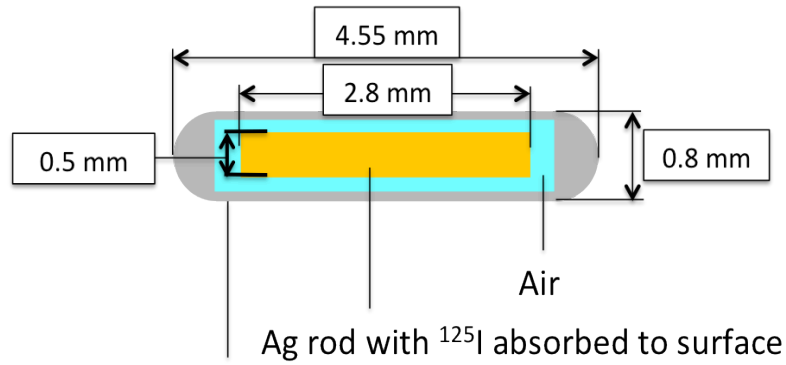
4. Conclusions

We calculated and compared some dosimetric parameters of two ^{125}I sources used in Japan by MC simulation. The difference of the photon energy spectra for the sources effect to the radial dose function, and that of the geometry of Ti capsule effects to the anisotropy function.

References

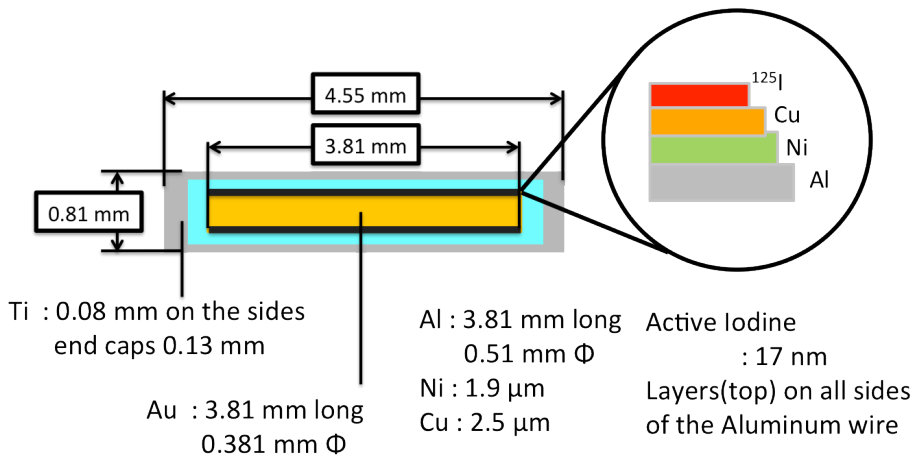
- 1) R. Nath, L. L. Anderson, G. Luxton, K. A. Weaver, J. F. Williamson, and A. S. Meigooni, "Dosimetry of interstitial brachytherapy sources: Recommendations of the AAPM Radiation Therapy Committee Task Group No. 43," *Med. Phys.* **22**, 209–234, (1995).
- 2) M. J. Rivard, B. M. Coursey, L. A. DeWerd, M. S. Huq, G. S. Ibbott, M. G. Mitch, R. Nath, and J. F. Williamson, "Update of AAPM Task Group No. 43 Report: A revised AAPM protocol for brachytherapy dose calculations," *Med. Phys.* **31**, 633–674, (2004).
- 3) M. J. Rivard, W. M. Butler, L. A. DeWerd, M. S. Huq, G. S. Ibbott, A. S. Meigooni, C. S. Melhus, M. G. Mitch, R. Nath, and J. F. Williamson, "Supplement to the 2004 update of the AAPM Task Group No. 43 Report," *Med. Phys.* **34**, 2187–2205, (2007).
- 4) H. Hirayama, Y. Namito, A. F. Bielajew, S. J. Wilderman, and W. R. Nelson, *The EGS5 Code System*, SLAC-R-730 Stanford Linear Accelerator Center, Stanford, CA, (2005).
- 5) J. Dolan, Z. Li, and J. F. Williamson, "Monte Carlo and experimental dosimetry of an ^{125}I brachytherapy seed," *Med. Phys.* **33**, 4675–4684, (2006).
- 6) A. S. Kirov and J. F. Williamson, "Monte Carlo-aided dosimetry of the Source Tech Medical Model STM1251 I-125 interstitial brachytherapy source," *Med. Phys.* **28**, 764–772, (2001).
- 7) National Nuclear Data Centre, information extracted from the NuDat 2.5 database, <http://www.nndc.bnl.gov/nudat2>.

(a)



Ti : 0.07 mm thickness

(b)



Ti : 0.08 mm on the sides
end caps 0.13 mm

Au : 3.81 mm long
0.381 mm Φ

Al : 3.81 mm long
0.51 mm Φ
Ni : 1.9 μm
Cu : 2.5 μm

Active Iodine : 17 nm
Layers(top) on all sides
of the Aluminum wire

Fig.1 Cross-sectional view of the internal structures of the two ^{125}I source models used in this study.
(a) Model 6711 (b) Model STM1251

Table 1 The primary ^{125}I photon spectrum used in Monte Carlo simulation taken from NuDat

	Energy (keV)	Intensity (%)
XR 1	3.77	14.9 % 6
XR $k\alpha_2$	27.202	40.1 % 10
XR $k\alpha_1$	27.472	74.0 % 19
XR $k\beta_3$	30.944	6.83 % 17
XR $k\beta_1$	30.995	13.2 % 3
XR $k\beta_2$	31.704	3.80 % 9
	35.4922 5	6.68 % 13

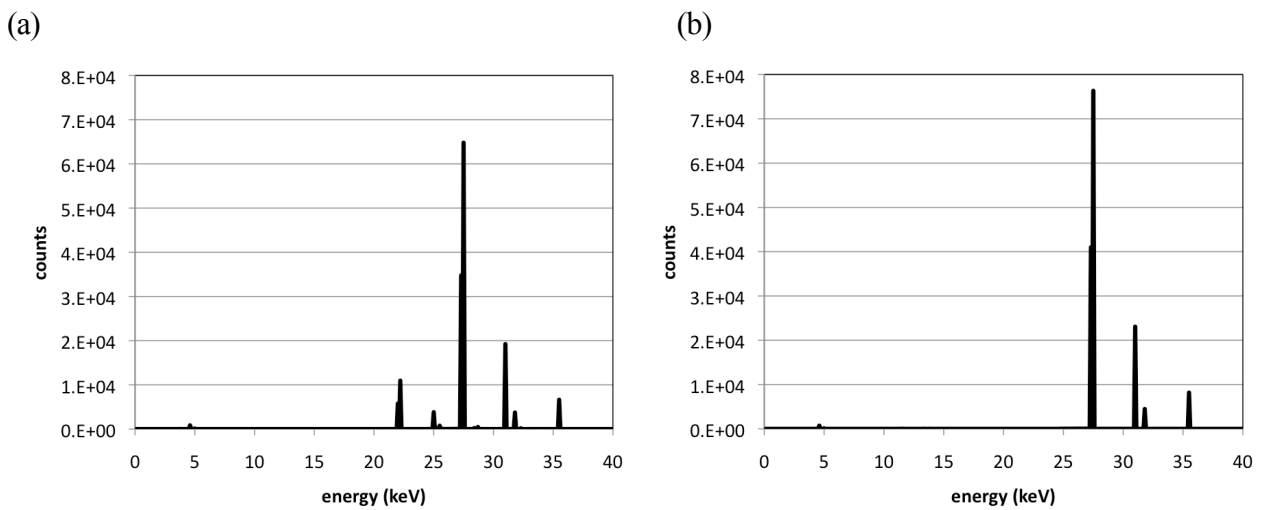


Fig.2 The photon energy spectra of the two ^{125}I sources. (a) Model 6711 (b) Model STM1251.

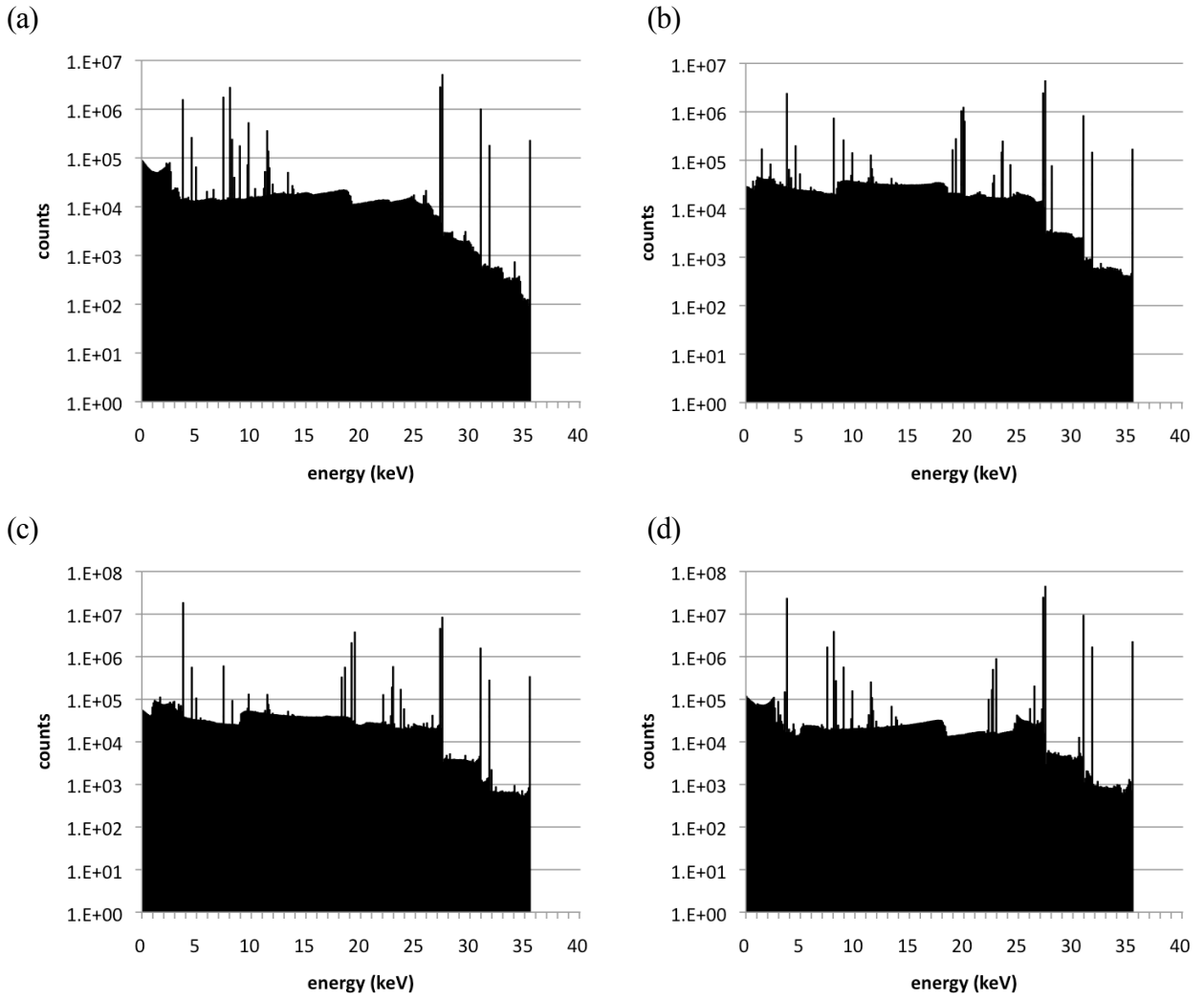


Fig.3 The absorbed energy spectra of the materials consisting the STM1251.
 (a) Al (b) Ni (c) Cu (d) Ti

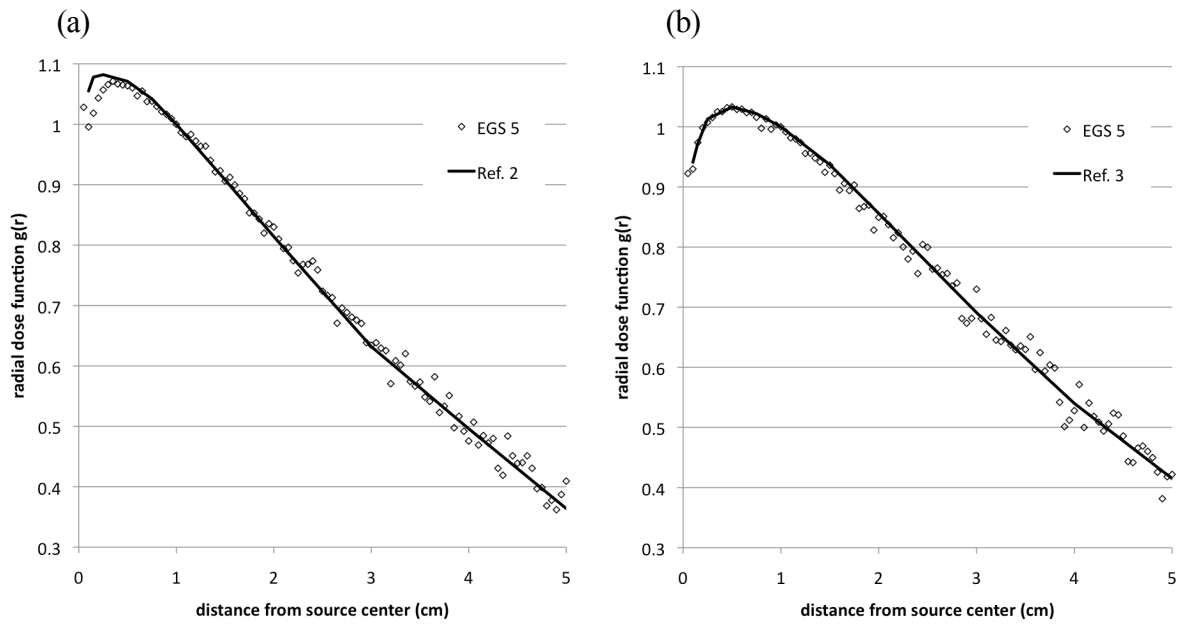


Fig.4 The radial dose function of the two ^{125}I sources. (a) Model 6711 (b) Model STM1251.

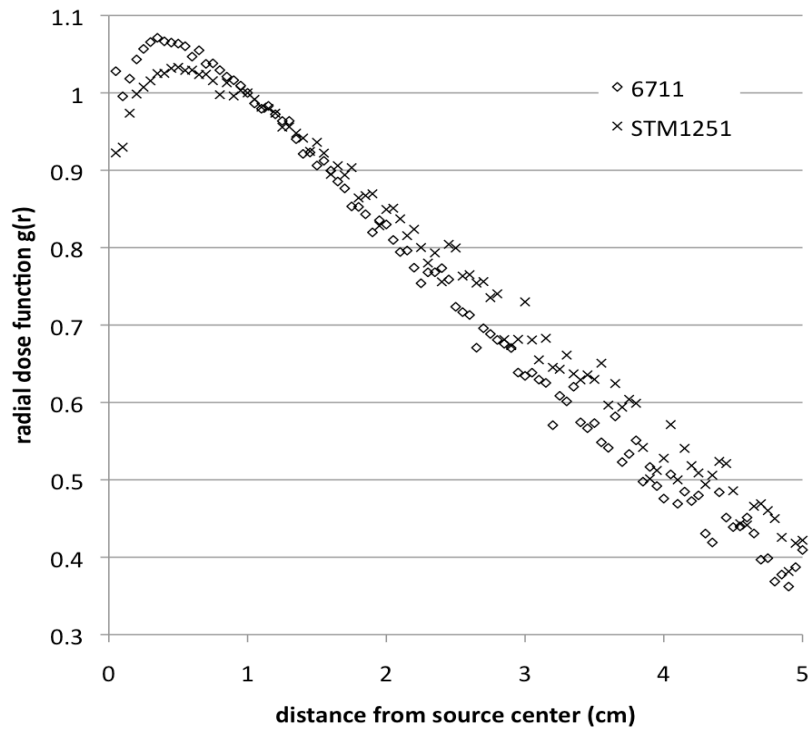


Fig.5 The comparing of the radial dose function between two ^{125}I sources

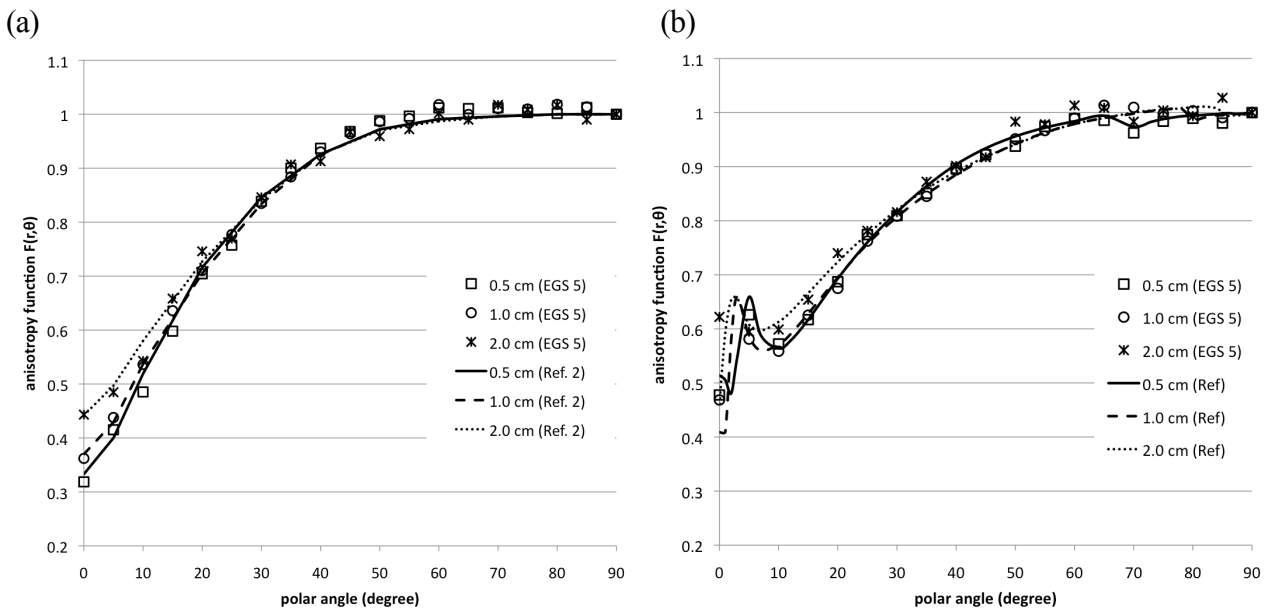


Fig.6 The anisotropy function of of the two ^{125}I sources. (a) Model 6711 (b) Model STM1251.

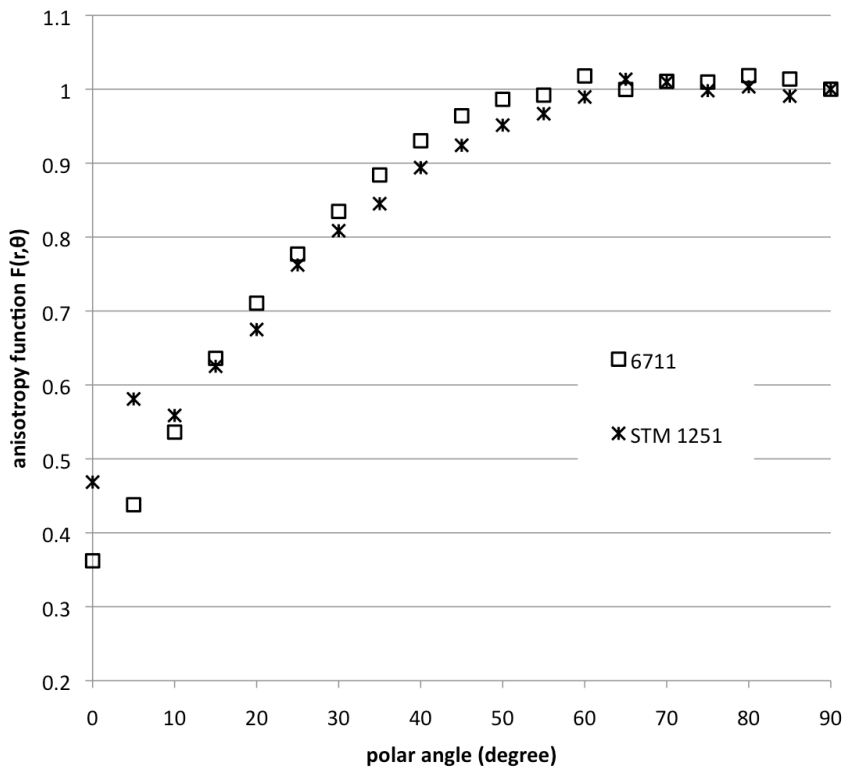


Fig.7 The comparing of the anisotropy function between two ^{125}I sources

Dose Distribution for Iodine-125 Seed Implant Brachytherapy

Sho Wakumura¹, Kichiro Koshida², Kousuke Matsubara²,
Yuichi Kurata³, shinichi ueda³, and Kimiya Noto³

¹Graduate School of Medical Science, Kanazawa University

²School of Health Science, College of Medical,
Pharmaceutical and Health Science, Kanazawa University

³Radiology Division, Kanazawa University Hospital

e-mail: swn440_613@yahoo.co.jp

Abstract

The incidence of prostate cancer is increasing in Japan, and iodine-125 (¹²⁵I) seed implant brachytherapy is becoming more widely used. Seed sources from 2 companies (STM1251, Model6711) are used for ¹²⁵I seed implant brachytherapy in Japan. In this study, energy spectra of brachytherapy were examined to determine whether the same energy spectra can be obtained during simulations. In addition, radiation dose distribution with radiation source placement used in the actual treatment was examined with actual measurements and simulations. The source-to-detector distance for actual energy spectrum measurement was 5 cm, and the energy spectrum of photons entering the Ge detector was detected at every 30° of radiation source angle. Simulations were conducted with the same setup as used for actual measurement. With regard to radiation dose distribution, placement of the radiation source and the shapes of the prostate and rectum are specified by the treatment plan, and radiation dose distribution is created using a 0.2×0.2×0.2 cm³-voxel tissue phantom. With regard to energy distribution of photons emitted from the radiation source, spectra comparable to those obtained in the actual measurement were obtained in both STM1251 and Model6711 brachytherapy. With regard to radiation dose distribution inside the phantom created as described above, which mimics the prostate, the simulation results for both radiation sources showed distributions different from that of the treatment plan. With regard to the emitted photon energy distribution, properties specific to the two types of radiation source were well simulated. To improve the accuracy of radiation dose distribution, the voxel size of the phantom must be made smaller, and the human body composition should be used as the composition of each voxel.

1. Introduction

The incidence and mortality rates of prostate cancer have been increasing in Japan, and with introduction of PSA examination, the number of identified cases of localized early prostate cancer is rapidly increasing. Thus, the use of iodine-125 (¹²⁵I) seed implant brachytherapy is becoming more widespread for prostate cancer. The types of radiotherapy for prostate cancer include external-beam radiotherapy and interstitial radiotherapy, and ¹²⁵I seed implant brachytherapy is included in interstitial radiotherapy. The benefits of this treatment include the spatial radiation dose distribution, which is better than that of external-beam radiation therapy, relatively few side effects with decreased dose to surrounding organs and good likelihood of maintenance of the reproductive function of the prostate, and reduced incidence of urinary

incontinence.

¹²⁵I seed sources from 2 companies (STM1251, Model6711) are used for ¹²⁵I seed implant brachytherapy in Japan, and each has its characteristic energy spectrum for the radiation source. As the change in radiation dose distribution around the radiation source is very sharp, and the actual measurement of energy spectrum emitted from the radiation source and the spectrum from simulation must match, the energy spectra of brachytherapies were examined to determine whether the same results were obtained with simulations. In addition, treatment plan and simulations were compared to examine the effects of therapeutic and peripheral doses.

2. Materials and Methods

2.1 Energy spectrum

Measurements were taken with the ¹²⁵I seed implant brachytherapy source (STM1251, Model6711) placed 5 cm from the Ge detector (High-Purity Germanium EG&G ORTEC Detector Model GLP-06165/05-P)¹⁾ A lead shield for spectral measurement in diagnostic X-ray was put on to the Ge detector to shield against scattered radiation. An angle of 0° was set to a point perpendicular to the source long axis, and the energy spectrum was obtained from the results of the Ge detector at every 30°.

For simulation, the structures of the seed radiation sources from the two companies are shown in Figs. 1 and 2. These radiation sources were placed in the same manner as in the actual measurement, and the point of origin of photons was set at aluminum wire (0.5 mm) in STM1251 and the surface of silver tow (0.51 mm) in Model6711²⁾⁻⁵⁾. Photons were produced from each point in 4π directions, and the total number of photons was 2.0×10⁸. The energy division was set as 0.156 keV, and energy spectrum was obtained based on the results.

2.2 Radiation dose distribution

For the actual measurement, 1 case of intraoperative plan was used for each radiation source. The uniformity of the radiation source was measured at a point 2 mm from the center of the radiation source in water-equivalent material. Therefore, in the treatment plan, the compositions of the prostate and surrounding organs were calculated as water-equivalent material. Absorbed dose at an arbitrary point in the treatment plan is calculated using equation (1)⁶⁾

$$D(r,\theta) = K_8 \Lambda_{r\theta} \left[\frac{G(r,\theta)}{G(r_0,\theta_0)} \right] g_{r_0}(r) F(r,\theta) \quad \dots(1)$$

D(r,θ), K₈, Ar₀, G(r,θ), g_{r₀}(r), and F(r,θ) are absorbed dose rate point (r,θ), reference air kerma rate, dose rate constant, geometry factor, radial dose function, and anisotropy function, respectively.

In simulations, the placement of radiation sources and the shapes of the prostate and rectum are specified by the treatment plan, and prostate composition is considered as soft tissue, composition around the prostate as muscle tissue⁷⁾ using 0.2×0.2×0.2 cm³-voxel tissue phantom. Using the results obtained, Origin 8 (Light Stone) was used to determine the radiation dose distributions in the transverse, coronal and sagittal planes.

3. Results

3.1 Measurement of energy spectrum and simulation comparison

Energy spectra of STM1251 and Model6711 derived from the results are shown in Figs. 3 and 4,

respectively. The maximum counts were corrected to 10,000 and 6,000, respectively.

In both STM1251 and Model6711, the ^{125}I energy peaks (average energy 35.5 keV, 31.0 keV, 27.5 keV) were analyzed. In Model6711, characteristic X-ray of Ag (Ag- K_{α} : 22.1 keV; Ag- K_{β} : 24.9 keV) and Ti (Ti- K_{α} : 4.51 keV, Ti- K_{β} : 4.93 keV) were also observed⁸⁾. The energy peaks observed in both STM1251 and in Model6711 at around 18 keV were Ge- K_{α} , K_{β} escape peak from the Ge detector¹⁾

The error between the actual measurement and simulation was maximum error +4.38% (31.0 keV), minimum error -2.24% (35.5 keV) in STM1251 and maximum error +3.74% (31.0 keV), minimum error +2.24% (35.5keV) in Model6711; both were within $\pm 5\%$.

Figures 5 and 6 show the actual measurement at each angle and energy spectra of the simulations with STM1251 and Model6711, respectively. For each radiation source, the number of photons detected decreases as the angles increases.

3.2 Radiation dose distribution measurement and comparison to the simulation

Figures 7, 8, and 9 show the radiation dose distribution obtained from the results. In each figure, the treatment plan is shown on the left and the radiation dose distribution is shown on the right.

The transverse planes in both STM1251 and Model6711 were relatively well-matched between simulation and actual measurement, but in the simulation, the position in the dose region was shifted compared to that of the treatment plan. In the coronal plane, expansion of each dose region was observed. In the sagittal plane, high-dose regions that were not seen in the treatment plan were observed.

In the simulation, radiation dose reached the rectum due to expansion of the dose region in transverse and sagittal planes, and in the coronal plane the radiation dose for the urethral tube was different from the actual measurement.

4. Discussion

Similar energy spectra were observed in simulation and actual measurement for both radiation sources. The differences observed with different angles were also matched closely between simulation and actual measurement. The reason why the characteristic X-ray spectrum for Ti was observed in simulation with Model6711 was because in actual measurement, the counts around a few keV were cut out by the Ge detector.

Slight shifts in position of radiation dose distribution were observed in both STM1251 and Model6711, which was probably due to the effects of voxel size. In addition, as the prostate and composition around the prostate were different between the treatment plan and the simulation, the dose region was expanded in the simulation.

The high-dose regions observed in sagittal plane in the simulation results for both radiation sources were probably because the radiation source was placed proximal to the cross-section that was measured, and because of the prominent effects of the above-mentioned voxel size and composition.

5. Conclusions

Comparison of the emitted photon energy distribution of the actual measurement and simulation showed good simulated properties of the two types of radiation source. Ti is used in STM1251 as well as in Model6711, but Ti was not detected in STM1251, and therefore the cutoff value in simulation must be considered further.

We believe the accuracy of radiation dose distribution can be improved by using smaller voxel sizes and by making the composition of each voxel closer to the human body composition. The results in this study

suggested the possibility that the actual radiation dose in the prostate will differ from the treatment plan, and therefore further comparisons between prostate and peripheral composition converted to water-equivalent material and to prostatic glandular tissue are necessary.

References

- 1) SEIKO EG&G: HPGe (High-Purity Germanium) Planar Photon Detector System EG&G ORTEC Part Number 803408 Manual Revision A
- 2) STM1251: Document from Medicon, Inc.
- 3) Model6711: Document from Nihon Medi-Physics Co., Ltd.
- 4) Sridhar Sahoo, T. Palani Selvam: An EGSnrc investigation of the air-kerma strength, dose rate constant, and radial dose function of ¹²⁵I brachytherapy source
- 5) A. S. Kirov and J. F. Williamson: Monte Carlo-aided dosimetry of the Source Tech Model STM1251 I-125 interstitial brachytherapy source
- 6) ICRU REPORT 72
- 7) ICRU REPORT 46
- 8) Edgardo Browne, Richard B. Firestone, Virginia S. Shirley: Table of Radioactive Isotopes, 1985
- 9) Takahiro Yamada: Status of radiation dose standard traceability of ¹²⁵I seeds radiation source Japan Radioisotope Association

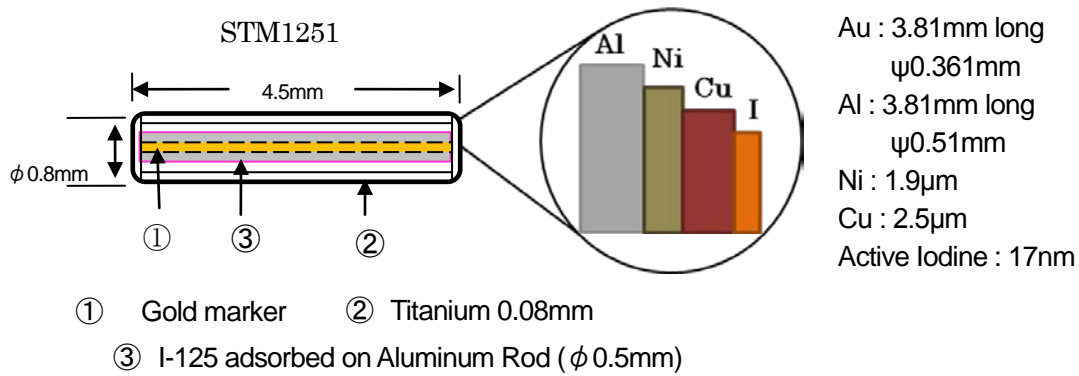


Fig.1 Internal structure of STM1251

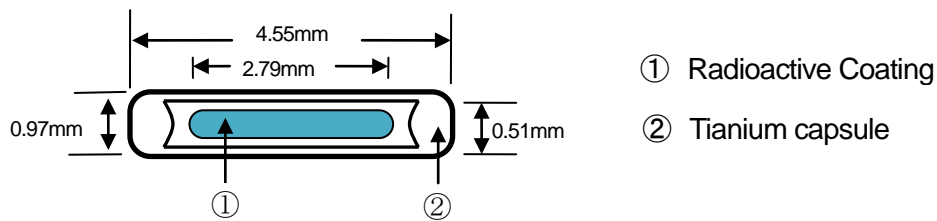


Fig.2 Internal structure of Model6711

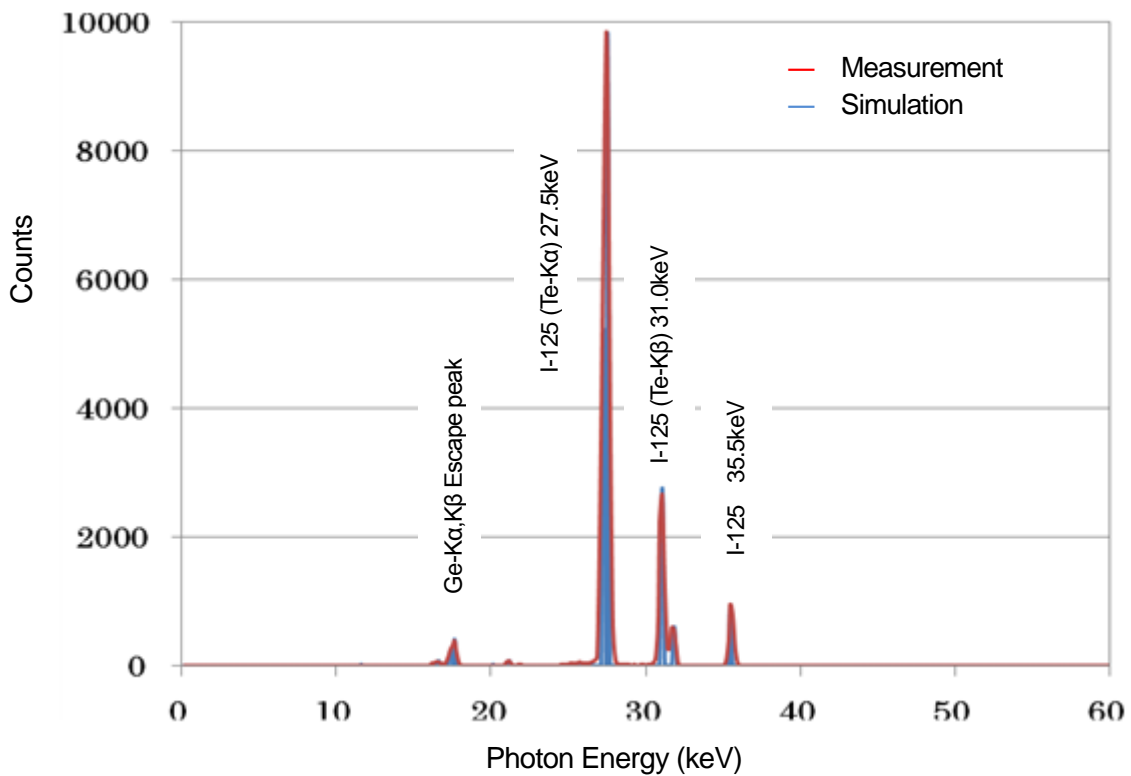


Fig.3 The results of the measured and simulated energy spectra of STM1251

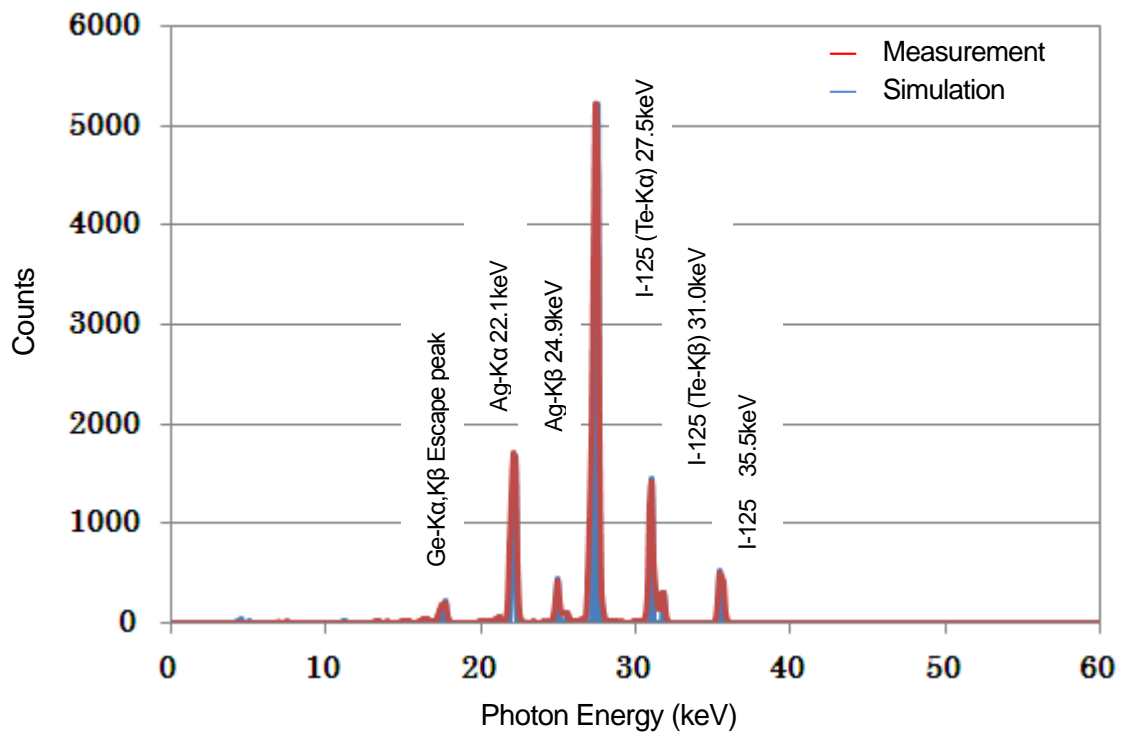


Fig.4 The results of measured and simulated energy spectra of Model6711

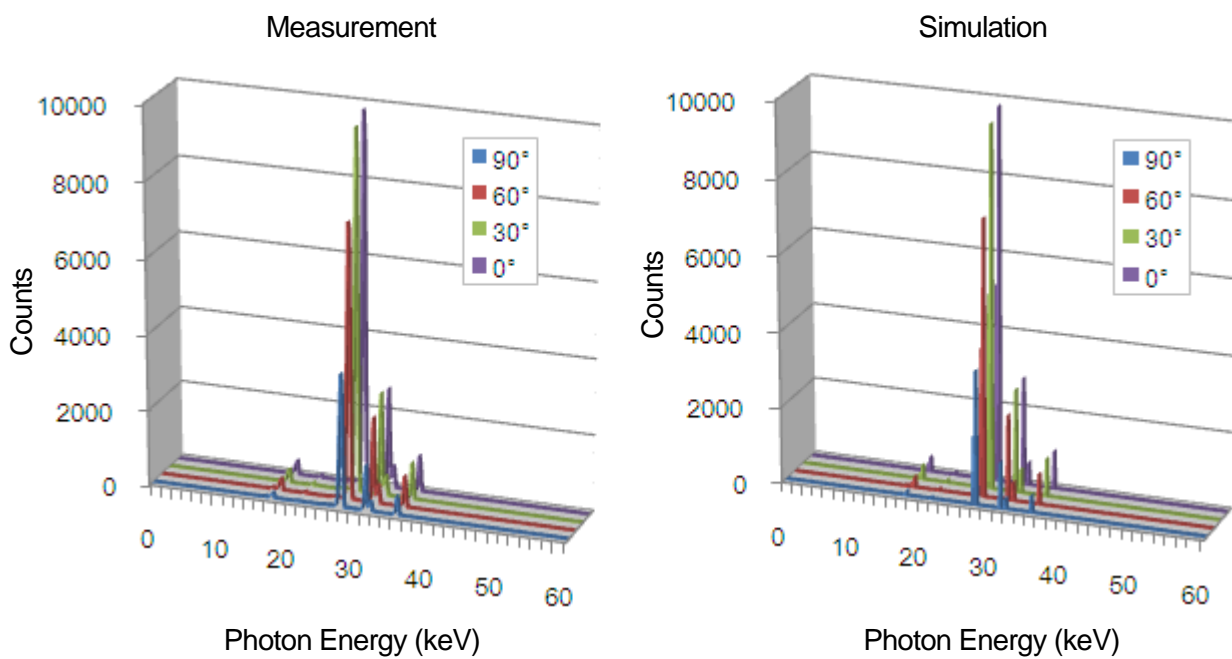


Fig.5 Comparison among the results of each angle energy spectra of STM1251

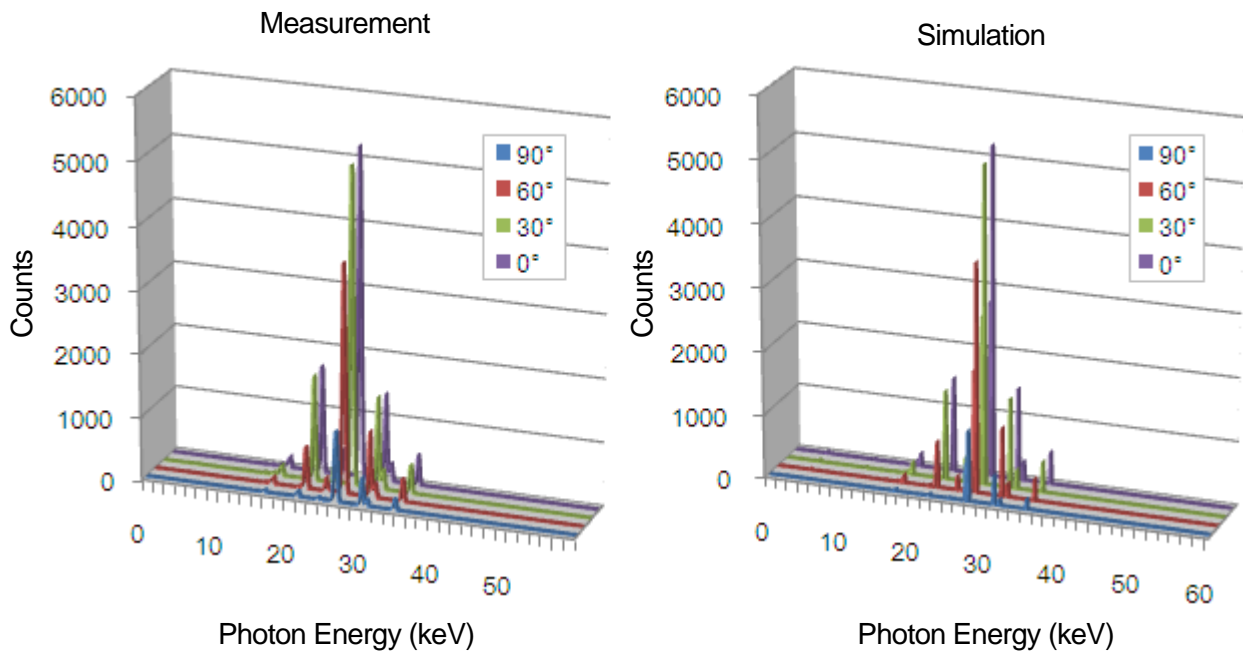


Fig.6 Comparison among the results of each angle energy spectra of Model6711

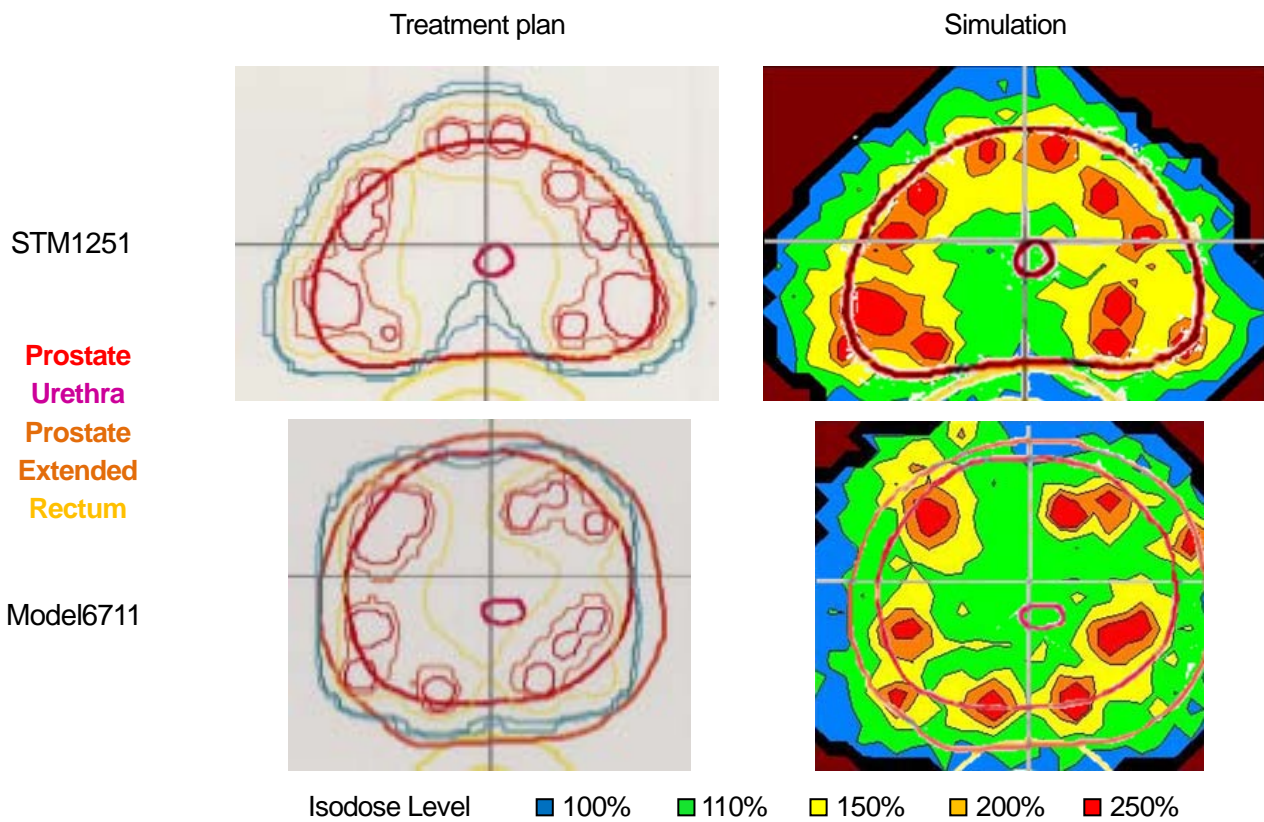


Fig.7 Radiation dose distribution of treatment and simulation in Transverse plan

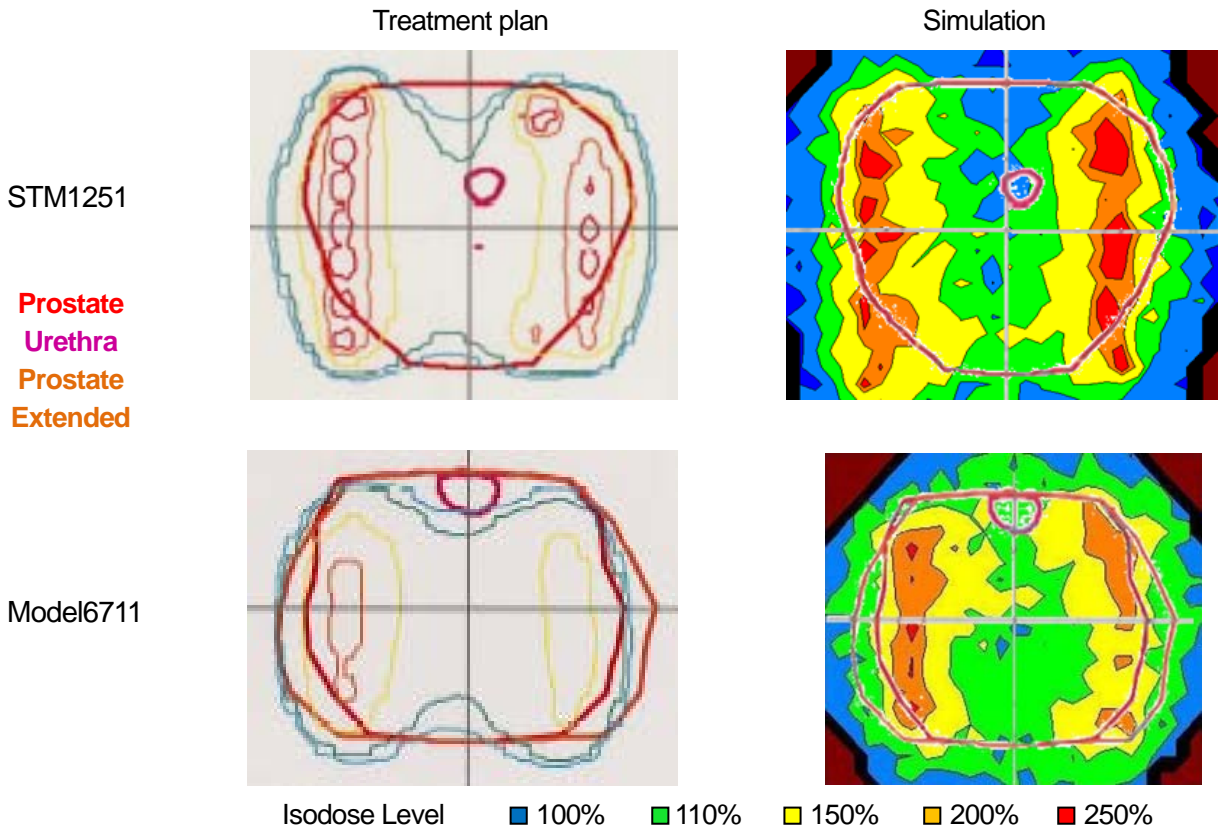


Fig.8 Radiation dose distribution of treatment plan and simulation in Coronal plan

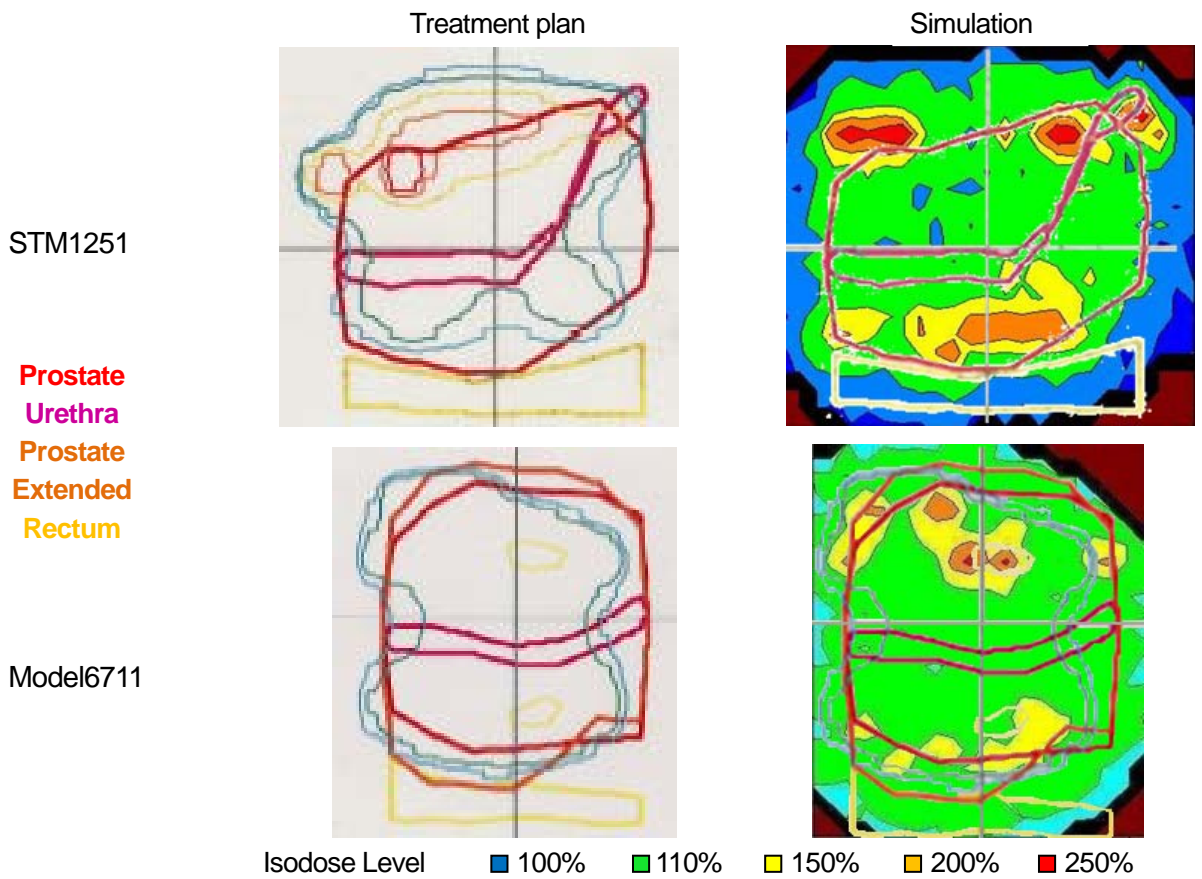


Fig.9 Radiation dose distribution of treatment plan and simulation in Sagittal plan

ANGULAR DEPENDENCE OF ^{192}Ir HDR RADIATION SOURCE FOR TREATMENT

S. TSUJI and N. NARIHIRO[†]

Kawasaki Medical School, Kurashiki 701-0192, Japan

[†]*Kawasaki College of Allied Health Professions, Kurashiki 701-0194, Japan*

Abstract

The microSelectron-HDR remote afterloading device has used for high dose-rate brachytherapy. We use the calculations of AAPM TG43 for brachytherapy. We indicated the comparison between the calculations of TG43 and EGS5 simulations for brachytherapy. However the comparison was restricted calculations, simulations and measurements along the axis of ^{192}Ir source cable($\theta = 0$). We report the comparisons among TG43 calculations, EGS5 simulations and the measurements various distances and angles.

1 Introduction

The microSelectron-HDR remote afterloading device with high-intensity ^{192}Ir sources is used for brachytherapy. The sources capsuled in a stainless are embedded and irradiated the prostate. Generally, a clinical treatment is planned before an actual irradiation in a body. The calculated values of doses are derived from PLATO clinical planning system. The calculation algorithm follows American Association of Physicists in Medicine Task group No.43 Report (AAPM TG-43) [1], and they are based on dose-rate distributions used for clinical implementation and dose-calculation methodologies. AAPM TG-43 is generally the only the way of the algorithm for brachytherapy in Radiology. Some ^{192}Ir dose rate for brachytherapy source are investigated with Monte Carlo simulations [2, 3, 4, 6] The EGS5 is the powerful simulation for electromagnetic interactions and can be applied in the field of radiology. Comparing of EGS5 simulations and TG-43 calculations is important to check the reliability of TG-43 and consequently we can do a reliable treatment. We reported doses comparisons with EGS5 simulations, TG-43 calculations and measurements last year. However they are compared only “investigations in a straight line”, which was investigated along the axis of ^{192}Ir source cable. In this time, we investigate doses a various distance and angles between an ^{192}Ir source and a detector. We report the differences among the measurements, EGS simulations and TG-43 calculations.

2 AAPM TG-43

The PLATO brachytherapy planning system calculate based on AAPM TG-43 [1]. The dose-rate equation is following,

$$\dot{D}(r, \theta) = S_k \cdot \Lambda \cdot \frac{G(r, \theta)}{G(r_0, \theta_0)} \cdot g(r) \cdot F(r, \theta), \quad (1)$$

where r denote the distance (in centimeters) from the center of the active source to the point of interest, r_0 denotes the reference distance which is specified to be 1 cm in this protocol, and θ denotes the polar angle specifying the point of interest, θ_0 denotes the reference angle which is specified to be 90° shown as Fig.1. The other parameter S_k , Λ , $G(r, \theta)$, $g(r)$ and $F(r, \theta)$ represent the air-kerma strength, the dose rate constant, the geometry function, the radial dose function and the 2D anisotropy function respectively. S_k is calculated as the source intensity when the treatment

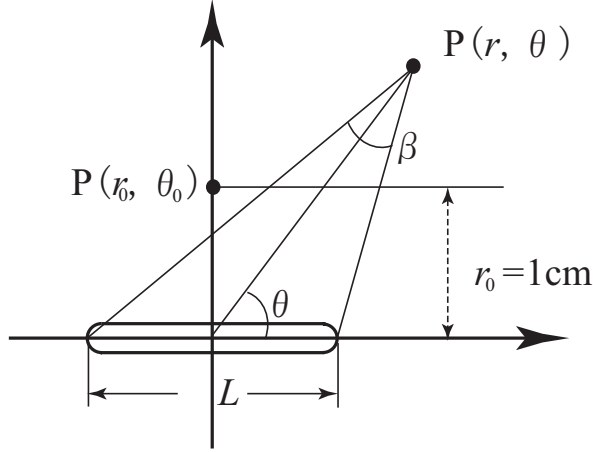


Figure 1: Coordinate system used for brachytherapy dose calculations. $P(r, \theta)$ represents the interesting point. r_0 and θ_0 mean 1 cm and 90° respectively.

starts. Λ is used the value 1.108 cGy/h/U in this planning system. The unit U is defined as the air-kerma strength, $1U=1\text{cGy}\cdot\text{cm}^2/\text{h}$.

2.1 Geometry function

The purpose of the geometry function is to improve the accuracy with which dose rate can be estimated by interpolation from data tabulated at discrete points. The protocol uses of point and line source models give the following functions,

$$G_P(r, \theta) = r^{-2} \quad \text{point source approximation,} \quad (2)$$

$$G_L(r, \theta) = \begin{cases} \frac{\beta}{Lr \sin \theta} & \text{if } \theta \neq 0^\circ \\ (r^2 - L^2/4)^{-1} & \text{if } \theta = 0^\circ \end{cases} \quad \text{line source approximation,} \quad (3)$$

where β is the angle as shown in Fig.1.

2.2 Radial dose function

The radial dose function, $g_X(r)$, accounts for dose fall-off on transverse-plane due to photon scattering and attenuation, and is defined by Eq.(4),

$$g_X(r) = \frac{\dot{D}(r, \theta_0) G_X(r_0, \theta_0)}{\dot{D}(r_0, \theta_0) G_X(r, \theta_0)}. \quad (4)$$

The subscript “X” represents whether a point source, “P”, or line source, “L” is used in transforming the data.

2.3 2D anisotropy function

The 2D anisotropy function, $F(r, \theta)$, is defined as

$$F(r, \theta) = \frac{\dot{D}(r, \theta) G_L(r, \theta_0)}{\dot{D}(r, \theta_0) G_L(r, \theta)}. \quad (5)$$

The Geometry function G_L is the formula in case of the line source.

2.4 $g_L(r)$ and $F(r, \theta)$ tables

$g_X(r)$ and $F(r, \theta)$ are investigated by the experiment and the Monte Carlo simulations in each point or line sources. We use a high-intensity ^{192}Ir source which is the microSelectron-HDR new design type. Each values of this radial dose function $g(r)$ and the 2D anisotropy function $F(r, \theta)$ are tabulated by G.M.Daskalov [2].

3 Measurement method

We measured ^{192}I source intensities. We used the ^{192}I microSelectron-HDR new design type, the ionization chamber PTW N30013 which has 0.6 cm^3 detectable volume and Mix-Dp phantoms (Fig. 2). The ionization chamber was fixed in fact when intensities were measured. This is a same

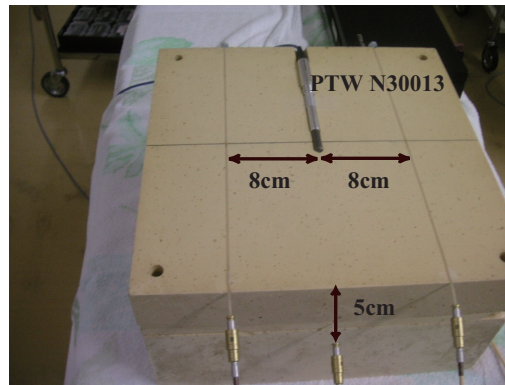


Figure 2: The picture shows the experiment in which the absorbed dose in the Mix-Dp phantom plate is measured. The ionization chamber is used PTW N30013. The distances are 5cm and 8cm.

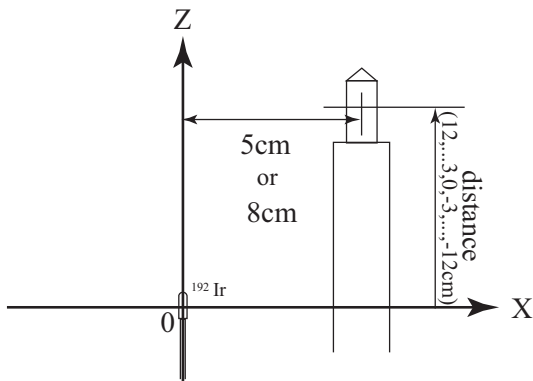


Figure 3: A positional relationship of ^{192}Ir source and the ion chamber. The distance X is 5 cm or 8 cm. The Z distance is from -12 cm to 12 cm.

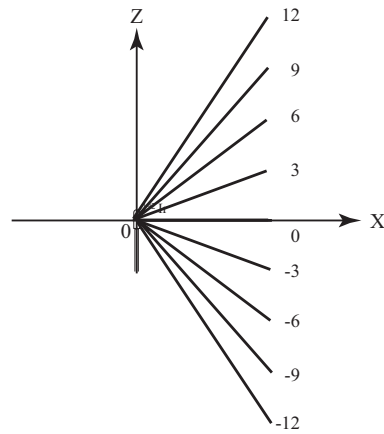


Figure 4: A sketch of the positional relationship of ^{192}Ir source and the ion chamber. Solid lines are distances r . Numbers show Z coordinates. Table 1 and Table 2 show angles θ and distances r .

situation that the source is fixed and the ionization chamber is moved as shown in Fig. 3. We had measured by 3 cm in the Z distance from -12 cm to 12 cm and X distance 5 cm and 8 cm as shown in Fig. 3 and Fig. 4. Especially Fig. 4 shows chambers position in the center of the source.

Numbers in Fig. 4 shows Z coordinates. Angles θ and distances r in Fig. 1 each distance Z show

Table 1: Angles θ and distances r . ($X=5.00$ cm)

distance Z (cm)	-12	-9	-6	-3	0	3	6	9	12
θ (deg.)	22.62	29.06	39.81	59.04	90.00	120.96	140.19	150.95	157.38
distance r (cm)	13.00	10.30	7.81	5.83	5.00	5.83	7.81	10.30	13.00

Table 2: Angles θ and distances r . ($X=8.00$ cm)

distance Z (cm)	-12	-9	-6	-3	0	3	6	9	12
θ (deg.)	33.69	41.63	53.13	69.44	90.00	110.56	126.87	138.37	146.31
distance r (cm)	14.42	12.04	10.00	8.54	8.00	8.54	10.00	12.04	14.42

in Table 1(distance $X=5$ cm) and Table 2(distance $X=8$ cm).

4 EGS5 simulation

4.1 Simulation conditions

For the EGS5 simulating, the following parameters are considered in various regions or mediums, sampling of angular distributions of photoelectrons, K and L edge fluorescent photons, K and L Auger electrons, Rayleigh scattering, linearly polarized photon scattering, incoherent scattering and Doppler broadening of Compton scattering energies. We continued the simulations until the cut off kinetic energy 1 keV for one track. As other conditions, the emission rate of ^{192}Ir is 2.072.

4.2 Absolute dose in simulation

We measure charge in an ionization chamber. Though measured charges contain same systematical errors, the absorbed dose calculated by the charge is thought to be reliable. Because the ionization chamber is calibrated by ^{60}Co in National Institute of Radiological Sciences. We need to simulate an absolute dose for comparison with the reliable measurement. Ir metal density is greater ($=22.4$

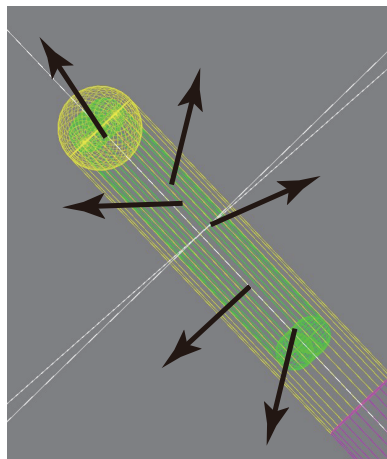


Figure 5: Gamma rays are emitted in all over the ^{192}Ir volume in the EGS5 simulation. We count them out of the stainless capsule of the ^{192}Ir source. The rate is 0.88029.

g/cm^3). So a survival probability of gamma-ray going from the inside the metal is smaller than 0.9.

We check the survival probability using EGS5 Monte Carlo simulation considering with a structure of a ^{192}Ir source and a stainless capsule. The value is 0.88029. We gain the absolute dose also with the emission rate 2.072 following equations,

$$\text{Absolute dose (Gy/sec.)} = \text{Using radioactivity (Bq)} \times \text{Simulation value (Gy/incident)} \times 2.072/0.88029. \quad (6)$$

5 Results

5.1 Comparison with experimental results and EGS5 simulations

We measured absolute doses in Mix-Dp phantoms at the distance $X=5$ cm and $X=8$ cm. The point source was moved in the distance Z from -12 cm to 12 cm by 3 cm. We measured them with a 0.6 cm³ ionization chamber in 60 second time. A radiation intensity of the source is 381.058 GBq. Results are shown as doses per one second (Gy/sec.). Fig. 6 shows absolute doses at $X=5$ cm

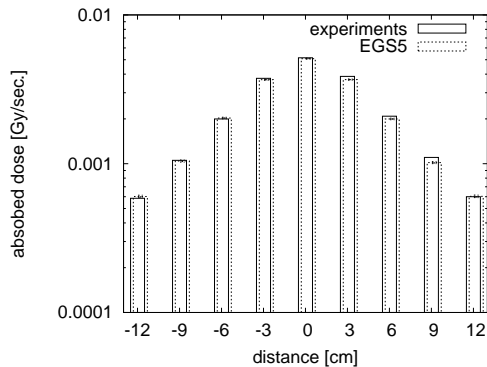


Figure 6: Absolute doses at $X=5$ cm. Horizontal axis “distance” means Z distance in Fig. 1. Solid lines represent experimental results. Dashed lines represent EGS5 simulations.

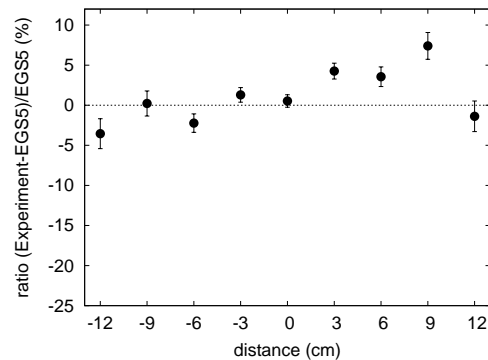


Figure 7: Ratios of (experimental results - EGS5 results)/EGS5 results at $X=5$ cm. Horizontal axis “distance” means Z distance.

$Z=-12 \sim 12$ cm. Fig. 7 shows the deviation between experimental results and EGS5 simulations as ratios. Table 3 shows absolute doses of experimental and EGS5 simulation results. Fig. 8 shows

Table 3: Absolute doses at $X=5$ cm. “distance Z ” represents Z distance in Fig. 1. Units of experiment and EGS5 simulation results are $\times 10^{-3}$ Gy/sec.

distance Z (cm)	-12	-9	-6	-3	0
Exp.	0.5856 ± 0.0004	1.0528 ± 0.004	1.9980 ± 0.0009	3.7485 ± 0.0017	5.1493 ± 0.0014
EGS5	0.602 ± 0.012	1.042 ± 0.016	2.028 ± 0.024	3.672 ± 0.033	5.082 ± 0.040
distance Z (cm)	3	6	9	12	
Exp.	3.8624 ± 0.0026	2.0868 ± 0.0010	1.1015 ± 0.0004	0.5998 ± 0.0005	
EGS5	3.675 ± 0.035	1.999 ± 0.024	1.018 ± 0.016	0.603 ± 0.012	

absolute doses at $X=5$ cm $Z=-12 \sim 12$ cm. Fig. 9 shows the deviation between experimental results and EGS5 simulations as ratios. Table 4 shows absolute doses of experimental and EGS5 simulation results. As compared with $X=5$ cm (Fig. 6 or Fig. 7) and $X=8$ cm (Fig. 8 or Fig. 9), discrepancies of experiments and simulations are large at $X=8$ cm and large distance Z . At $X=8$ cm and $Z=\sim \pm 12$ cm, discrepancies are within 10% as shown in Fig. 9.

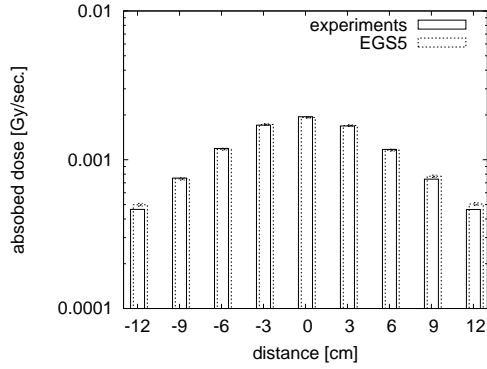


Figure 8: Absolute doses at X=8 cm. Horizontal axis “distance” means Z distance in Fig. 1. Solid lines represent experimental results. Dashed lines represent EGS5 simulations.

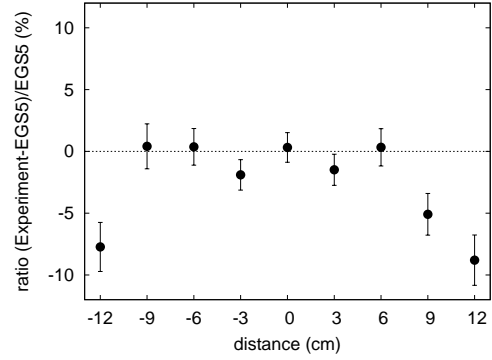


Figure 9: Ratios of (experimental results – EGS5 results)/EGS5 results at X=8 cm. Horizontal axis “distance” means Z distance.

Table 4: Absolute doses at X=8 cm. “distance Z” represents Z distance in Fig. 1. Units of experiment and EGS5 simulation results are $\times 10^{-3}$ Gy/sec.

distance Z (cm)	-12	-9	-6	-3	0
Exp.	0.4634 ± 0.0005	0.7527 ± 0.011	1.1901 ± 0.0004	1.7072 ± 0.0009	1.9462 ± 0.0004
EGS5	0.498 ± 0.011	0.744 ± 0.013	1.176 ± 0.017	1.726 ± 0.022	1.925 ± 0.023

distance Z (cm)	3	6	9	12
Exp.	1.6861 ± 0.0013	1.1728 ± 0.0006	0.7406 ± 0.0004	0.4634 ± 0.0005
EGS5	1.698 ± 0.022	1.160 ± 0.017	0.774 ± 0.014	0.504 ± 0.011

5.2 Comparison with TG-43 calculations and EGS5 simulations

We can calculate a dose at a point using TG-43 equations [1]. However a simulation can only calculate a dose with some volume. As a comparison with a point, a volume with simulation

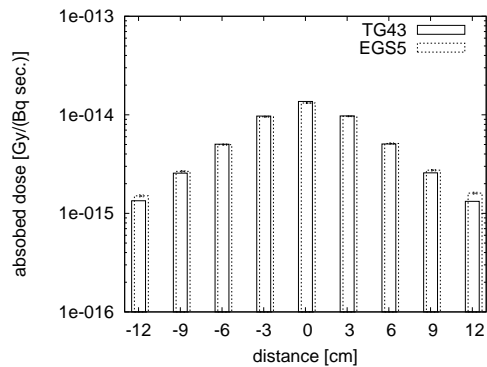


Figure 10: Absolute dose calculations and simulations at X=5 cm. Horizontal axis “distance” means Z distance in Fig. 1. Solid lines represent TG-43 calculations. Dashed lines represent EGS5 simulations.

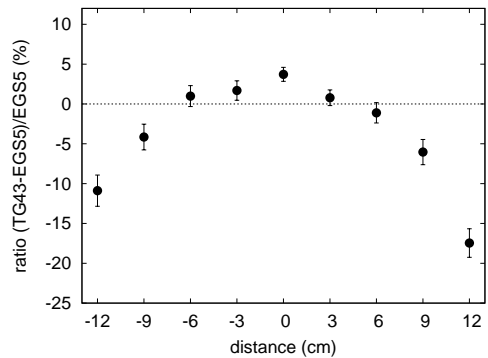


Figure 11: Ratios of (TG-43 results – EGS5 results)/EGS5 results at X=5 cm. Horizontal axis “distance” means Z distance.

may be small, but a volume may be large in statistic errors. We summed simulating events into

concentric lines around the radiation source. Specifically, the volume is $1 \text{ mm}^2 \times 2\pi r$. “ r ” represents a distance from the source. Simulated results in water are shown as doses per one second per one Bq (Gy/(Bq sec.)). Fig. 10 and Fig. 11 show comparisons with the TG-43 calculation and the EGS5 simulation at X=5 cm. Fig. 12 and Fig. 13 show comparisons with the TG-43 calculation

Table 5: Absolute dose calculations and simulations at X=5 cm. “distance Z” represents Z distance in Fig. 1. Units of TG-43 calculation and EGS5 simulation results are $\times 10^{-15}$ Gy/(Bq sec.).

distance Z (cm)	-12	-9	-6	-3	0
TG-43	1.342	2.559	5.033	9.716	13.66
EGS5	1.506 ± 0.033	2.670 ± 0.045	4.984 ± 0.065	9.555 ± 0.115	13.170 ± 0.111

distance Z (cm)	3	6	9	12
TG-43	9.750	5.062	2.576	1.325
EGS5	9.674 ± 0.094	5.119 ± 0.066	2.742 ± 0.046	1.605 ± 0.035

and the EGS5 simulation at X=8 cm. At Z= \sim 0 cm, the EGS5 simulations and the TG-43

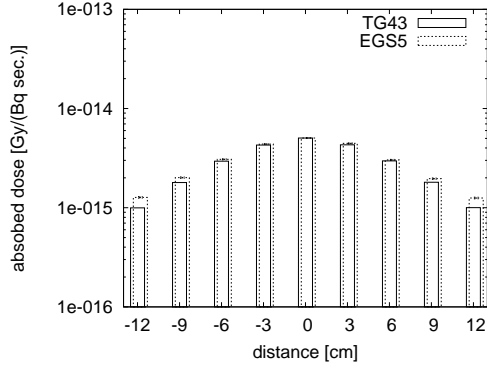


Figure 12: Absolute dose calculations and simulations at X=8 cm. Horizontal axis “distance” means Z distance in Fig. 1. Solid lines represent TG-43 calculations. Dashed lines represent EGS5 simulations.

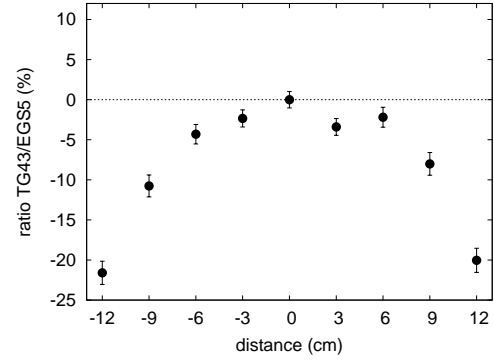


Figure 13: Ratios of (TG-43 results – EGS5 results)/EGS5 results at X=8 cm. Horizontal axis “distance” means Z distance.

Table 6: Absolute dose calculations and simulations at X=8 cm. “distance Z” represents Z distance in Fig. 1. Units of TG-43 calculation and EGS5 simulation results are $\times 10^{-15}$ Gy/(Bq sec.).

distance Z (cm)	-12	-9	-6	-3	0
TG-43	0.997	1.795	2.944	4.280	5.045
EGS5	1.271 ± 0.023	2.012 ± 0.031	3.077 ± 0.039	4.383 ± 0.048	5.045 ± 0.051

distance Z (cm)	3	6	9	12
TG-43	4.303	2.967	1.806	1.002
EGS5	4.455 ± 0.048	3.033 ± 0.039	1.963 ± 0.030	1.253 ± 0.024

calculations are good agreement each other. However the differences become as the distance from Z=0 cm increases. For example, The difference is \sim 20% at Z= \pm 12 cm and X= 8 cm. Table 5 and table 6 show absolute doses of TG-43 calculation and EGS5 simulation results. We gain

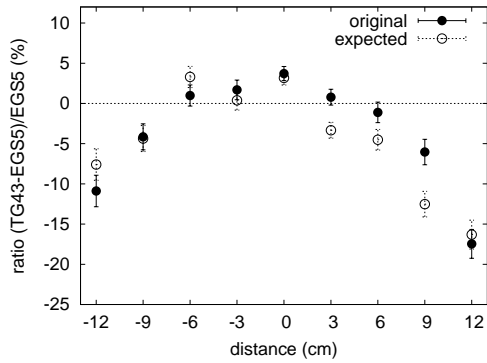


Figure 14: Ratios of (TG-43 results – EGS5 results)/EGS5 results at X=5 cm. Horizontal axis “distance” means Z distance. Solid circles are the same results in Fig. 11. Open circles are compensated ratios based on a deviation between the experimental values and EGS5 simulations in Fig. 6 or Fig. 7.

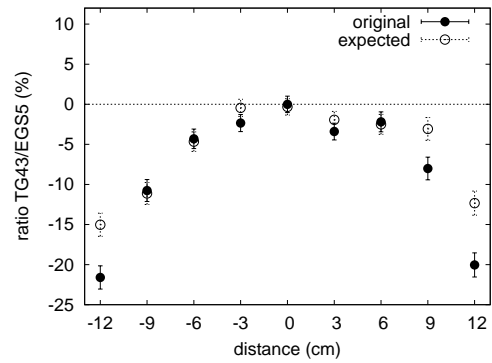


Figure 15: Ratios of (TG-43 results – EGS5 results)/EGS5 results at X=8 cm. Horizontal axis “distance” means Z distance. Solid circles are the same results in Fig. 11. Open circles are compensated ratios based on a deviation between the experimental values and EGS5 simulations in Fig. 8 or Fig. 9.

comparisons with experimental and EGS5 results. From the discrepancies, we can gain expected values if doses are measured with an ionized chamber. The open circles in Fig. 14 and Fig. 15 are compensated difference between EGS5 simulation and TG-43 calculations using ratios in Fig. 7 and Fig. 9. (The difference between experimental and EGS5 results become 0 modified the same way.) The difference of the expected open circles does not become small at the distance $Z \sim 12$ cm as shown in Fig. 14 and Fig. 15.

5.3 Comparison with radial dose function $g_L(r)$

From equation (4), We can estimate the radial dose function $g_L(r)$ using EGS5 simulations. Fig. 16

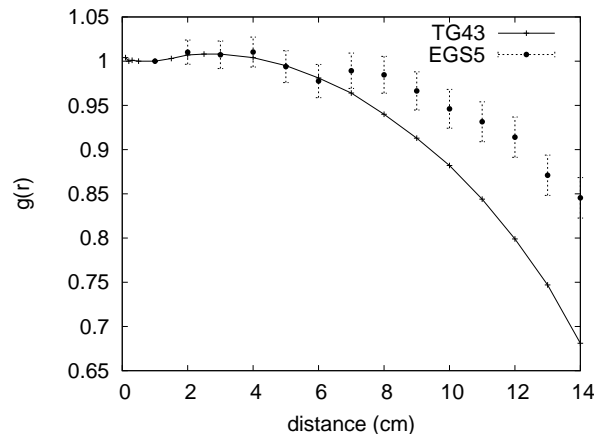


Figure 16: The vertical axis represents the radial dose function $g_L(r)$ and the horizontal axis is distance r as shown in the equation (4). The line shows $g_L(r)$ in TG-43 and plots show $g_L(r)$ with $\dot{D}(r, \theta)$ simulated in EGS5. We simulate in a $(100 \text{ cm})^3$ cubic water phantom.

shows $g_L(r)$ of TG-43 calculations [2] and EGS5 simulations. EGS5 simulations are calculated in a $(100 \text{ cm})^3$ cubic water phantom. The line shows the TG-43 calculations [2] and plots show EGS5

simulations. Up to 6 cm, they are in good agreement, however from 6 cm, the difference became greater. The difference is caused by $\dot{D}(r, \theta_0)/\dot{D}(r_0, \theta_0)$ of $g_L(r)$. At $Z=0$ cm ($\theta = 90^\circ$), comparisons are in good agreement, but they have $\pm 5\%$ differences. For example, the ratio $\dot{D}(r, \theta_0)/\dot{D}(r_0, \theta_0)$ for TG-43 at $X=5$ cm is 0.040202 and the ratio for EGS5 is 0.040162. The ratio for TG-43 at $X=8$ cm is 0.014839, whereas the ratio for EGS5 is 0.015546. The discrepancy is 4.7% as shown in Fig. 16.

6 Conclusion

We compare the EGS5 simulation, experimental results and the TG-43 calculations. At $Z=0$ cm, they are in good agreement each other, however at $Z \sim \pm 12$ cm, they are not in agreement. The comparison with experiments and the EGS5 simulations show the difference less than 10% at $Z \sim \pm 12$ cm. The comparison with TG-43 calculations and the EGS5 simulations show the difference around 20% at $Z \sim \pm 12$ cm. The radial dose function $g_L(r)$ using EGS5 simulations is in good agreement with TG-43 calculations up to 6 cm. From 6 cm, the difference of $g_L(r)$ becomes larger. The line of $g_L(r)$ is in good agreement in case using a 30 cm diameter spherical water phantom [4, 3]. Our result $g_L(r)$ in a $(100 \text{ cm})^3$ cubic phantom is similar to them in a $(80 \text{ cm})^3$ cubic phantom [3] or 50 cm diameter spherical phantom [4]. As compared with EGS5 simulations and TG-43 calculations, EGS5 simulations are better than TG-43 calculations at large distance and $\sim 0^\circ$ or $\sim 180^\circ$. In clinical case, results in limited phantom (~ 30 cm) may be more reliable because the distance is similar to a body scale. We conclude that the treatment planning with TG-43 calculations is done correctly around the distance up to 6 cm and around 90° .

References

- [1] M. J. Rivard et.al., Med. Phys. **31** 3,633(2004).
- [2] G. M. Daskalov, E. Löffler, J. F. Williamson, Med. Phys. **25** 11, 2200(1998).
- [3] R. E. P. Taylor and D. W. O. Rogers, Med.Phys. **35** 11,4933(2008).
- [4] P. Karaikos, A. Angelopoulos, L.Sakelliou, Med. Phys. **25** 10,1975(1998).
- [5] A. Angelopoulos, P. Baras and L. Sakellio, Med. Phys. **27** 11,2521(2000).
- [6] P. Karaikos, A. Angelopoulos, P. Baras, L.Sakelliou, Med. Phys. **26** 8,1498(1999).

FUNDAMENTAL STUDY FOR 3-DIMENSIONAL DOSE VERIFICATION FROM COMPTON SCATTERED PHOTONS USING EGS SIMULATION

Takumi Kodama, Atsushi Myojoyama, and Hidetoshi Saitoh

*Graduate School of Human Health Sciences, Tokyo Metropolitan University,
Tokyo, 116-8551, Japan
e-mail: kodama-takumi@hs.tmu.ac.jp*

Abstract

In recent years, Intensity Modulated Radiation Therapy is in popular. This technique is able to form suitable 3-dimensional dose distribution and irradiate target volume intensively. If dose distribution doesn't lie on the target, normal tissue might be exposed by high dose, so we should verify agreement of irradiation field and location of target volume 3-dimensionally. The Image Guided Radiation Therapy allows verification of target volume and organs at risk before irradiation, however there is a problem that normal tissue is exposed by extra radiation. Therefore new tools which can verify irradiation field and dose distribution 3-dimensionally is demanded. We aimed at Compton Camera as a 3-dimensional dose verification tool without extra radiation exposure. In this report, physical properties of scattered photons and the possibility of dose reconstruction from scattered photons was investigated by the EGS Monte Carlo simulation. As a result, it is confirmed that irradiation field shape can be recognized by reconstruction using simple back projection and sinogram which was sampled around water phantom.

1. Introduction

In recent years, Intensity Modulated Radiation Therapy (IMRT) is in popular [1]. This technique is able to form suitable 3-dimensional dose distribution and irradiate target volume intensively. If dose distribution doesn't lie on the target, normal tissue might be exposed by high dose. So we should verify agreement of irradiation field and location of target volume 3-dimensionally by using radiographic film, 2-dimensional array detector and/or electronic portal imaging device (EPID). The Image Guided Radiation Therapy (IGRT) allows verification of target volume and organs at risk before irradiation.

However there is a problem that normal tissue is exposed by extra radiation for verification. Therefore new tools which can verify irradiation field and dose distribution 3-dimensionally is demanded.

We aimed at Compton scattered photons which generated from irradiated volume during radiotherapy, and possibility of Compton Camera [2-4] as a 3-dimensional dose verification tool without extra radiation exposure. To investigate possibility of Compton camera using scattered photons, physical properties of scattered photons and the possibility of dose reconstruction from scattered photons was investigated by the EGS Monte Carlo simulation [5, 6] in this report.

2. Materials and Methods

2.1 Scatter angle and energy of scattered photons

If photon is scattered by Compton interaction at angle of θ to incident direction, energy of scattered photon $h\nu'$ is calculated by the following formula.

$$h\nu' = \frac{h\nu}{1 + \frac{h\nu}{m_e c^2} (1 - \cos\theta)} \quad (1)$$

where $h\nu$ is energy of incident photon, m_e is electron rest mass and c is light velocity. When 6 MV photons from medical linear accelerator are scattered at angle of $\theta = 45, 90$ and 135 degree, energy spectrum of scattered photons are shown in Fig. 1. Fig. 1 (a) shows energy spectrum of photon beam generated from ordinary 6 MV linac and Fig. 1 (b) shows energy spectrum of scattered photons calculated by formula (1). Spectrum has narrower range at an obtuse scatter angle than spectrum at acute scatter angle.

In this report, 90 degree is selected as scatter angle for simple geometry and 2 MeV mono energy photons is used as incident beam because which generate 0.4 MeV photons after 90 degree scatter.

2.2 Possibility of Compton camera for reconstruction of irradiation field

To investigate possibility of Compton camera using photons sampled at any direction, scattered photons from water phantom were sampled by the EGS Monte Carlo simulation. The simulation geometry is shown Fig. 2. Water phantom ($30 \text{ cm} \times 30 \text{ cm} \times 30 \text{ cm}$) was irradiated by $10 \text{ cm} \times 10 \text{ cm}$ square field vertically. When scattered photons go out water phantom and pass through the slit collimator, energy and coordinates where Compton interactions take place were stored in the simulation. Slit collimator has 0.5 cm gap and 10 cm depth. In this report, 2 MeV mono energy photons were generated and 90 degree is selected as scatter angle.

2.3 Investigation of optimum aperture size and reconstruction of irradiation field

To detect scattered photons at angle of 90 degree selectively, optimum aperture size for parallel hole collimator was investigated. The simulation geometry is shown in Fig. 3. Water phantom was irradiated by pencil beam vertically. In this report, rectangular hole collimator was employed. Hole width 0.5 cm and hole depth 10 cm were fixed and simulation were performed for 0.1, 0.5 and 1.0 cm hole height.

To reconstruct field width in high spatial resolution and efficiency, optimum aperture width was investigated. The simulation geometry is shown in Fig. 4. In this simulation, water phantom was irradiated by line beam vertically. Simulations were performed for 0.5 cm and 1.0 cm in width and height was fixed to 0.1 cm.

To investigate possibility of field reconstruction, scattered photon profiles were sampled at every 1 degree around the water phantom. The simulation geometry was shown in Fig. 5. Water phantom was irradiated by $10 \text{ cm} \times 10 \text{ cm}$ square field vertically. Sinogram was constructed using profiles of scattered photons and irradiated field was reconstructed by simple back projection.

3. Results and Discussion

3.1 Possibility of Compton camera for reconstruction of irradiation field

Fig. 6 shows energy spectrum of scattered photons which passed through the slit hole collimator. The peak of fluence can be observed at 0.407 MeV. This result shows that sampled photons were almost

single scattered photons.

Fig. 7 (a) shows the 2-D frequency distribution as a function of coordinates where Compton scatter takes place of sampled photons passed through the slit collimator. And Fig. 7 (b) shows number of sampled photons along horizontal axis of Fig. 7 (a). The irradiation field 10 cm×10 cm can be observed. Since almost sampled photons scattered in irradiation field, there is some potential of reconstruction of irradiated field using scattered photons.

Fig. 8 shows (a) the 2-D frequency distribution as a function of coordinates where Compton scatter takes place and (b) number of sampled photons along horizontal axis but when using energy window of 0.407 ± 0.01 MeV. The irradiated field can be observed clearly than simulation without energy window. This shows energy window has the possibility to improve signal noise ratio.

3.2 Investigation of optimum aperture size and reconstruction of irradiation field

Fig. 9 shows energy spectra of scattered photons passed through the hole that has aperture height 0.1 cm, 0.5 cm and 1.0 cm. The peak of fluence can be observed at 0.407 MeV, and scattered photons at angle of 90 degree were detected selectively as thinner.

Fig.10 shows profiles of scattered photons passed through the hole that has aperture width (a) 0.5 cm and (b) 1.0 cm. The irradiation field can be observed clearly at 0.5 cm than 1.0 cm.

Fig.11 shows irradiation field which reconstructed from profiles of scattered photons. It was noisy but irradiation field of 10 cm×10 cm can be recognized.

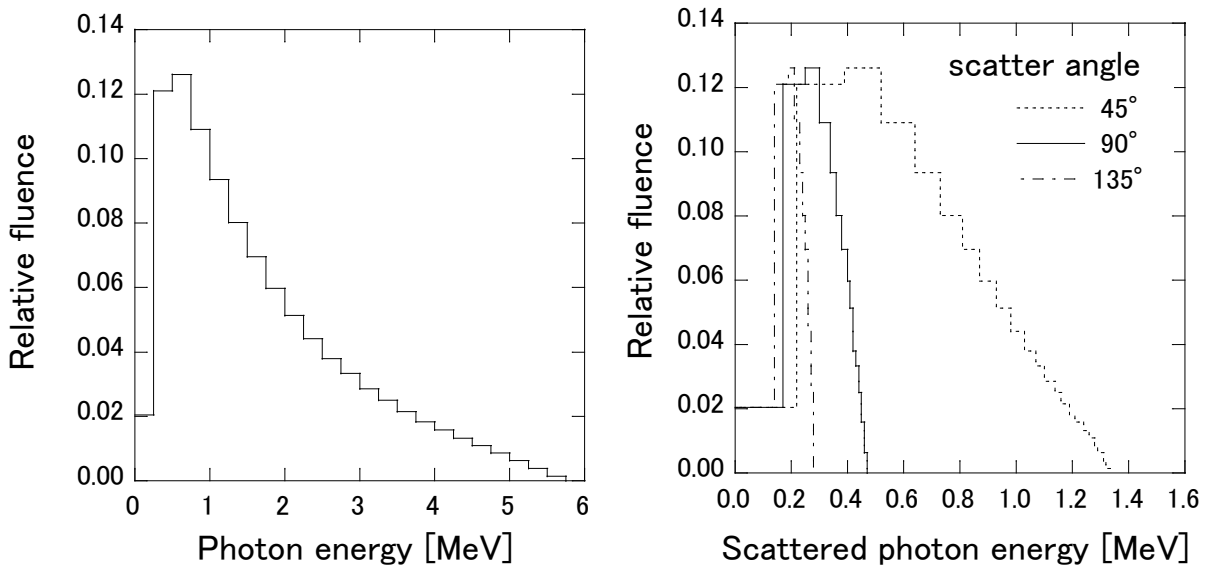
4. Conclusion

Since sampled photons were almost single scattered photons, possibility of Compton camera for reconstruction of irradiated field was confirmed. And there is possibility that energy window can improve signal noise ratio. Scattered photons at angle of 90 degree were detected selectively as aperture depth is thinner and irradiated field can be observed clearly at 0.5 cm aperture width.

The possibility that irradiation field can be reconstructed from profiles of scattered photons was indicated. However optimum aperture shape and size to detect scattered photons for any sampling angle selectively, and/or adequate angle should be studied to observe irradiation field. And optimum sampling and reconstruction algorithm should be studied to observe irradiation field.

References

- 1) AAPM Report No. 82, "Guidance document on delivery, treatment planning, and clinical implementation of IMRT: Report of the IMRT subcommittee of the AAPM radiation therapy committee," The American Association of Physicists in Medicine, Maryland. Vol. 30, No. 8, pp.2089-2115 (2003).
- 2) J. H. Lee, C. S. Lee, "Monte Carlo Study on the Imaging Resolution and Sensitivity of a Compton Camera," Korean Phys. Soc. **49**, pp. 97-102 (2006).
- 3) Lucas C. Parra, "Reconstruction of cone-beam projections from Compton scattered data," IEEE Transactions on Nuclear Science. **47**, No.4, pp.1543-1550 (2000).
- 4) Michael J. Cree, Philip J. Bones, "Towards Direct Reconstruction from a Gamma Camera Based on Compton Scattering," IEEE Transactions on Medical Imaging. **13**, No.2, pp. 398-407 (1994).
- 5) H. Hirayama, Y. Namito, A. F. Bielajew et al., "The EGS5 Code System", SLAC Report number: SLAC-R-730 and KEK Report number: 2005-8, (2010).
- 6) Report No. PIRS-701: *The EGSnrc Code System: Monte Carlo Simulation of Electron and Photon Transport*. National Research Council of Canada, Ottawa, (2002).



(a) An example energy spectrum of 6 MV photon beam (b) Energy spectra for several scattering angles

Fig. 1 Energy spectrum of 6 MV photon beam generated by ordinary linac and energy spectrum of scattered photons for several scattering angles

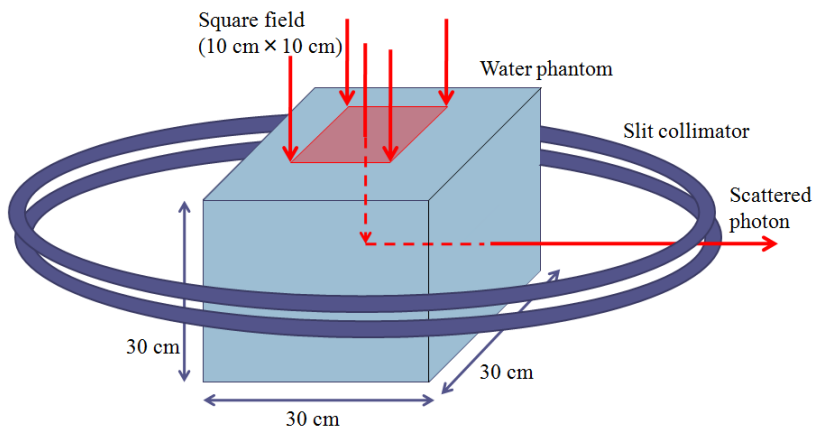


Fig. 2 Simulation geometry for investigation of possibility of Compton camera

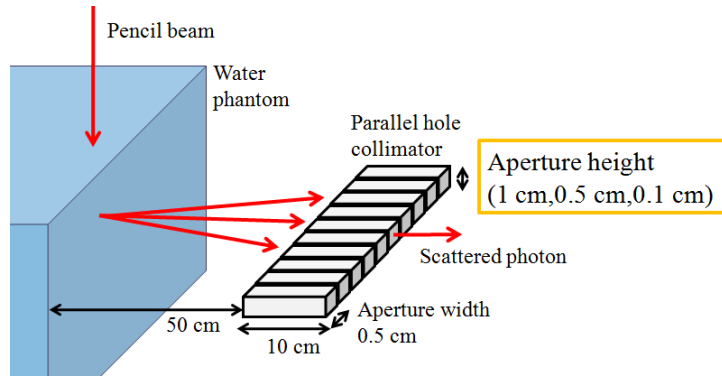


Fig. 3 Simulation geometry for investigation of optimum aperture height to detect scattered photons at angle of 90 degree selectively

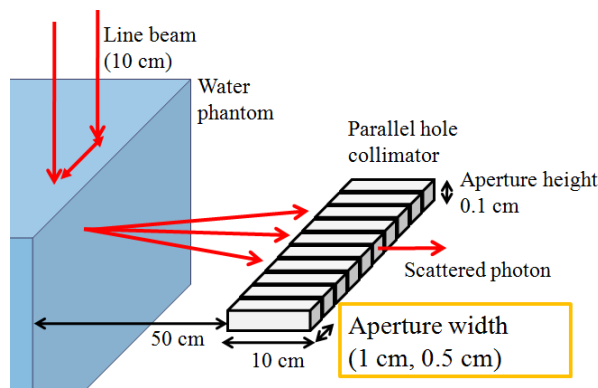


Fig. 4 Simulation geometry for investigation of optimum aperture width to reconstruct field width in high spatial resolution and efficiency

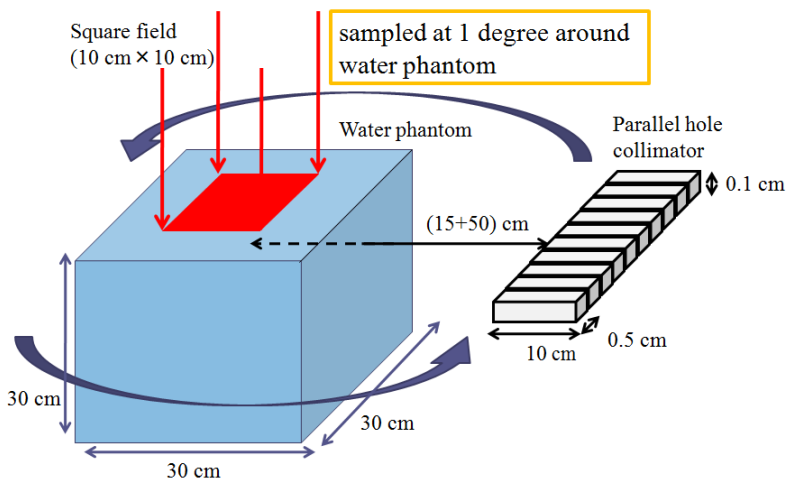


Fig. 5 Simulation geometry for investigation of possibility of field reconstruction from scattered photon profiles sampled around water phantom

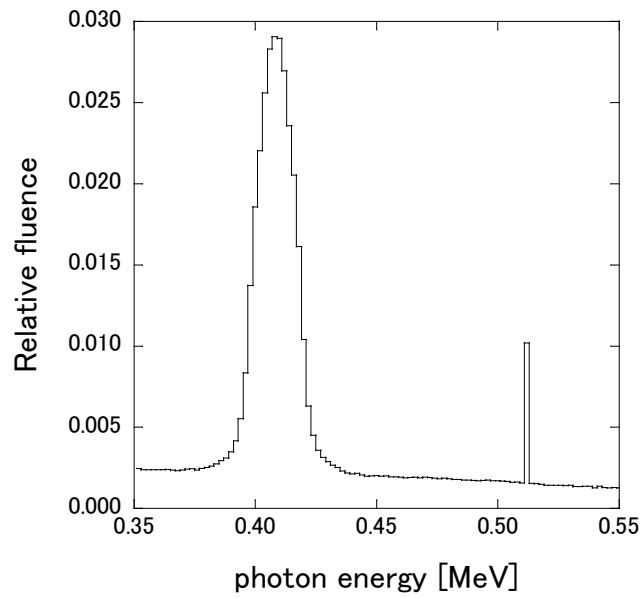
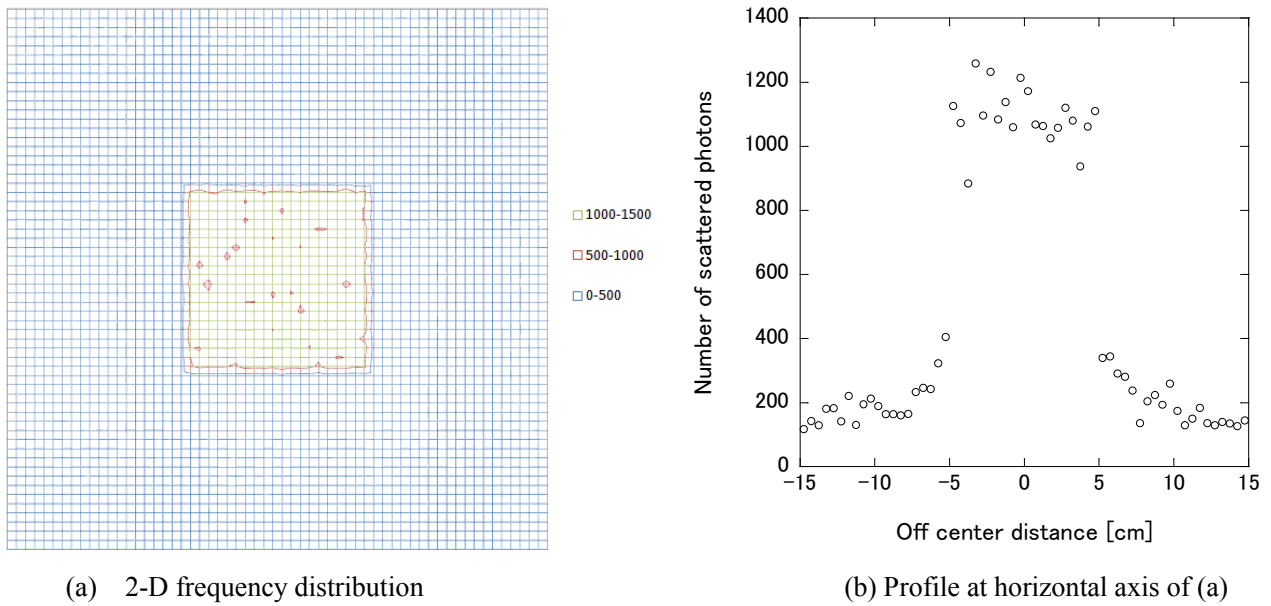


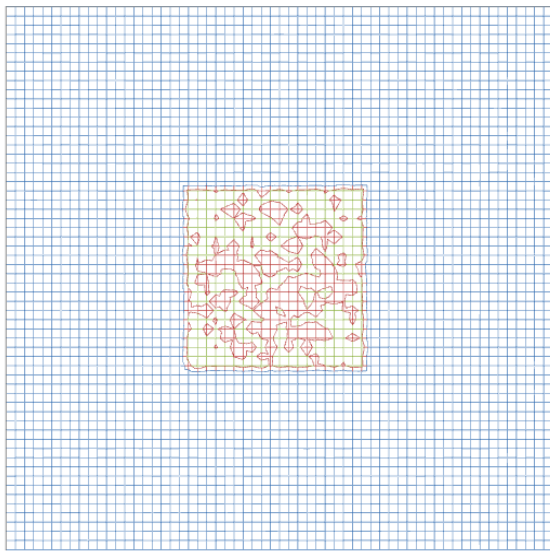
Fig. 6 Energy spectrum of scattered photons which passed through the slit collimator



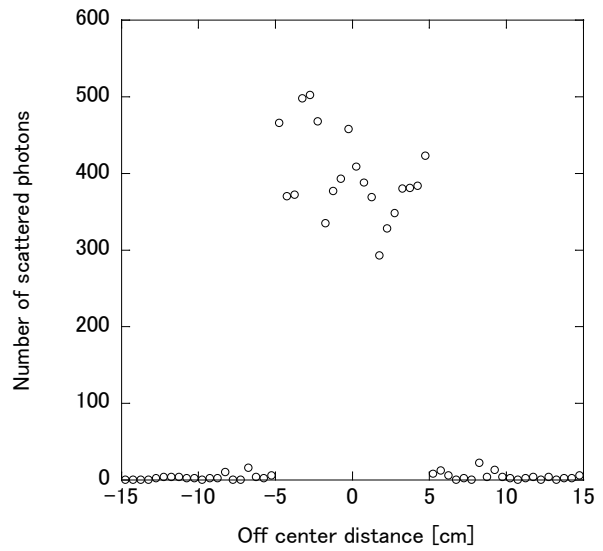
(a) 2-D frequency distribution

(b) Profile at horizontal axis of (a)

Fig. 7 2-D frequency distribution as a function of coordinates where Compton scatter takes place of sampled photons passed through the slit collimator and profile at horizontal axis of (a)



(a) 2-D frequency distribution



(b) Profile at horizontal axis of (a)

Fig. 8 2-D frequency distribution of coordinates where Compton scatter takes place of sampled photons passed through the slit collimator and profile at horizontal axis of (a) using energy window of 0.407 ± 0.01 MeV

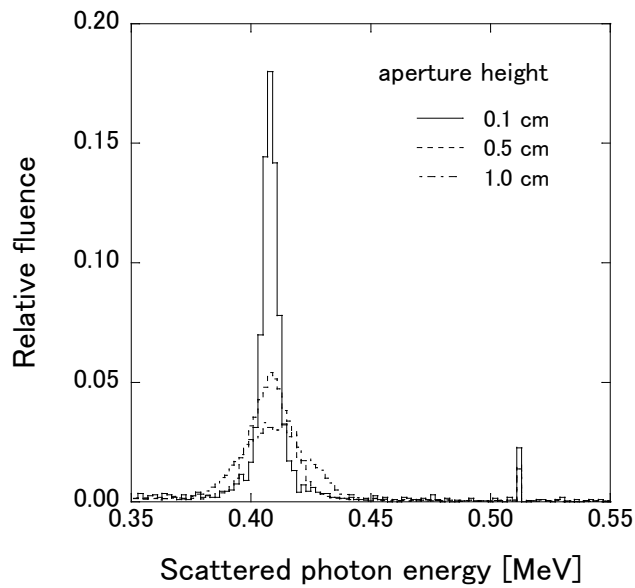


Fig. 9 Energy spectra of sampled photons for several aperture height

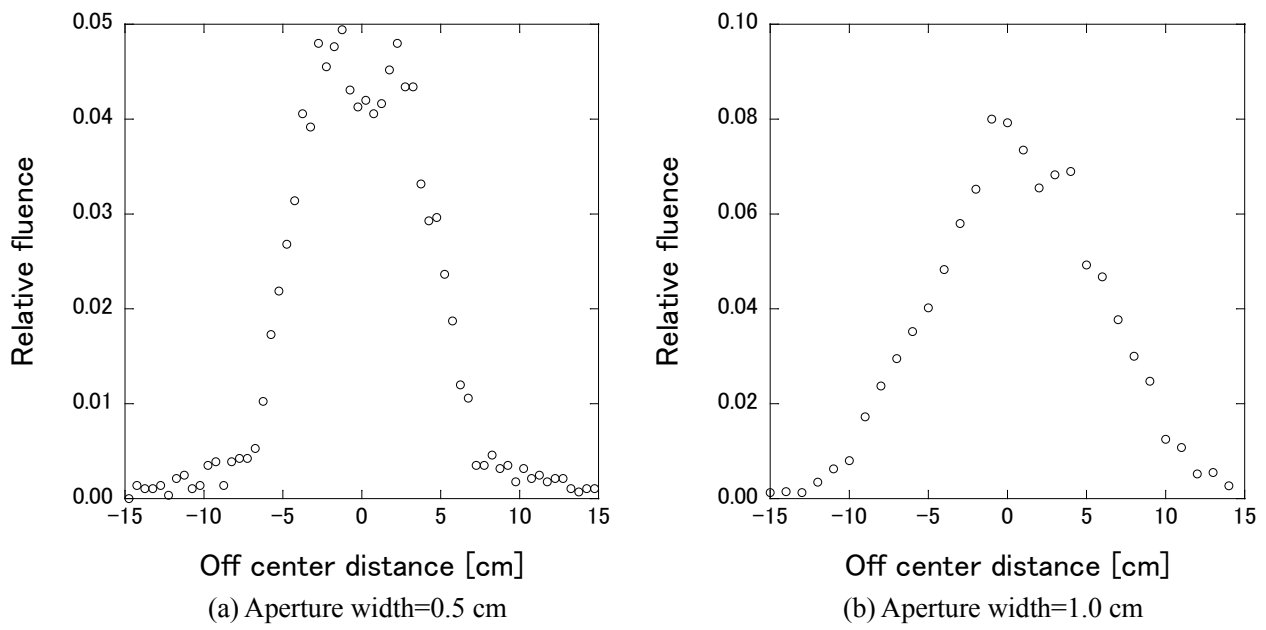


Fig. 10 Relative scattered photon fluence as a function of off center distance for several aperture width

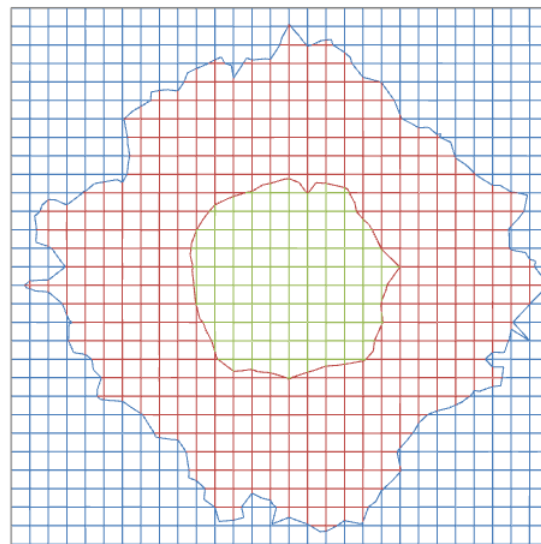


Fig. 11 Reconstructed radiation field on perpendicular plane to incident beam

Investigation of influence by gold crown to radiation therapy in oral cavity

Y.Igarashi¹, Y.Ito², T.Shimozato³, M.Komori³, Y.Obata³

¹Department of Radiological Technology, Graduate School of Medicine, Nagoya University

1-1-20 Daiko-Minami, Higashi-ku, Nagoya, Japan

²Department of radiology, Nagoya University Hospital

³Nagoya University School of Health Science

e-mail: igarashi.yukinori@g.mbox.nagoya-u.ac.jp

Abstract

In a radiotherapy of head and neck tumors, the oral cavity is frequently included in the irradiation field. In the case with the gold crown of the teeth, the dose was increased locally because of the scattered radiation. The acute inflammation was caused on the mucosa of the oral cavity at the vicinity of the gold crown more than the other mucosa by the radiation therapy. The purpose of this work is to study effects of the scattered radiation due to the gold crown comparing the relative dose to the progress and perpendicular directions to the beam axis using Monte Carlo (MC) simulation. The Electron Gamma Shower code version 5 (EGS5) was used for MC simulation. 4MV photon beam was irradiated with 5 x 5 cm² field size. The relative dose of the progress direction to the beam axis was up to 13.66 % in the near distance from the surface, and up to 3.66 % in the remote distance from the surface. Also, the relative dose of perpendicular direction was up to 30.51 % in the front of the gold crown, and down to nearly -10 % in the behind of that. These results are thought to be caused by the backscatter radiation, the front scatter radiation, the lateral scatter radiation, the lack of the secondary electron equilibrium ,and etc.

1. Introduction

In case of a performing radiotherapy with a high density substance (such as Ti), it has been reported that the dose enhancement and the dose reduction were caused by the scatter radiation [1-7]. In the radiotherapy, a radiation treatment planning system (RTPS) is used for the dose calculation inside patients. However, the calculation of the RTPS is not available for the vicinity of high-Z and high-density substances, and the result of the calculation is overestimated or underestimated as illustrated in Fig.1 [8].

In the radiotherapy of the head and neck tumors, the oral cavity is often included in the irradiation field. In the case with the gold crown given by the dental treatment, the oral mucosa coming into contact with gold crown is burned and inflamed by the influence of the scattered radiation, and the result of that creates an ulcer sometimes. Therefore, it is thought that to investigate the degree of the scatter is valuable in terms of the toxicity.

The purpose of this study is to investigate by obtaining the relative dose using Monte Carlo (MC)

simulation the degree of the dose increment and reduction by the gold crown and the degree of the dose differences in case with and without gold crown using a simple oral model with two opposed fields irradiation.

2. Material and methods

2.1 Measurement of oral geometry by measurement tools in RTPS

At first, to approach the clinical situation, the measurement of distance from surfaces of skin to teeth lines was performed using the CT images of patient who receives radiotherapy of oral cavity [9]. The results were obtained by the measurement tools in the RTPS. The way of the measurement is shown in Fig.2. In the CT images, the distance from the surface of skin to the teeth lines and the distance from the teeth lines to the surface of skin were measured. The places of the measurement are also shown in Fig.2. The subjects of the measurement are fifteen men and fifteen women. The results of this are shown in Table.1.

2.2 Monte Carlo calculations

The Electron Gamma Shower code version 5 (EGS5) was used for MC simulation. The simulation geometries were constructed from the results in Table.1 and are shown in Fig.3 and Fig.4. Table 2 shows the composition of the density of the materials. Data acquisition regions for the progressing direction to the beam axis were allocated in the phantom and each voxel size was $0.5 \times 0.5 \times 0.1 \text{ cm}^3$. Also, data acquisition regions for to the beam axis perpendicular direction were allocated as well and each voxel size was $0.1 \times 0.5 \times 0.1 \text{ cm}^3$. Energy spectrum was quoted from published data for 4 MV photon beams of Varian [10]. The cut-off energies for the transport calculation of electron (ECUT) and photon (PCUT) in this study were set to 521 keV and 10 keV, respectively. Statistical uncertainties of the MC simulations were less than 1.0 % for each voxel in the progressing direction to the beam axis and also less than 1.0 % for each voxel in the perpendicular direction to the beam axis for the isodose level greater than or equal to 50 %.

3. Results and discussion

3.1 The relative dose of progress direction to beam axis

Fig.5 and Fig.6 show the results of the relative dose in the vertical direction for men. The normalization was done by the dose at the center of phantom. In Fig.5, the dose enhancement was seen in front of the gold crown. In Fig.6, a little dose enhancement was also seen in front of the teeth. Fig.7 and Fig.8 show the comparison of the relative dose with and without the gold crown for men and women, respectively. Fig.9 and Fig.10 show the comparison of the relative dose in the parallel direction for men and women, respectively. The difference between the calculation results of EGS5 is defined as follows:

$$difference = \frac{D_{gold} - D_{teeth}}{D_{teeth}} \times 100[\%]$$

The differences of the calculation results were +13.66 % in the near distance from the surface, and +3.66 % in the remote distance from the surface. Including the other cases, the differences were shown in Table 3.

3.2 The relative dose of perpendicular direction to beam axis

Fig.11 and Fig.12 show the results of the relative dose in the vertical direction for men in front of the gold crown or a row of teeth, respectively. The normalization was done by the dose at the center of x axis. Fig.13 shows the comparison of both results, and the maximum difference was +30.51 %. Fig.14 and Fig.15 show the results in the back of the gold crown and a row of teeth, respectively. Fig.16 shows the comparison of those results, and the dose reduction is seen in the position of -0.55cm and 0.55cm. The differences of these cases in the each position were -9.44 %, -9.89 %, respectively. The results of women's case were also shown in Fig.17 and Fig.18. The maximum difference in front of the gold crown was +15.05%, and the differences in the back of that in the each position were -9.45%, -9.19%, respectively.

4. Conclusions

The degrees of the dose enhancement and the dose reduction with and without the gold crown were investigated in this work. The relative doses in the progress direction and in the perpendicular direction to the beam axis were obtained using the MC simulation. In comparison of the relative dose in the progressing direction to the beam axis, the dose enhancement in front of the gold crown was seen. Also, in comparison of the relative dose in the perpendicular direction to the beam axis, the dose enhancement or the dose reduction were seen. These results were caused by the influence of the backscatter radiation, the frontscatter radiation, the lateral scatter radiation, the lack of secondary electron equilibrium, and etc.

References

- 1) Otto A. Sauer, "Calculation of dose distributions in the vicinity of high-Z interfaces for photon beams." *Med. Phys.* **22**, 1685-1690 (1995)
- 2) X. Allen Li, James C. H Chu, et al., "Dose enhancement by a thin foil of high-Z material: A Monte Carlo study." *Med Phys.* **26**, 1245-1251 (1999)
- 3) L. Sung-Yen, C. Tieh-chi, L. Jao-Peerng and L. Mu-Tai, "effect of a metal hip prosthesis on the radiation dose in therapeutic photon beam irradiations." *Appl. Radiat. Isot.* **57**, 17-23 (2002)
- 4) Asghar Mesbahi, Farshad Seyed Nejad, "Dose attenuation effect of hip prostheses in a 9-MV photon beams: commercial treatment planning system versus Monte Carlo calculations." *Radiat. Med.* **25**, 529-535 (2007)
- 5) Bernd Reitemeier, Annette Schmidt, Dietmar Lehmann, et al., "Evaluation of a device for attenuation of electron release from dental restorations in a therapeutic radiation field." *The journal of prosthetic density*, **87**, 323-327 (2002)
- 6) Wolfram U. Laub, Fridtjof Nusslin, "Monte Carlo dose calculations in the treatment of a pelvis with implant and comparison with pencil-beam calculations." *Med. Dos.* **28**, 229-233 (2003)
- 7) Pail J. Keall, Jeffrey V. Siebers, Robert Jeral, et al., "Radiotherapy dose calculations in the presence of hip prostheses." *Med. Dos.* **28**, 107-112 (2003)
- 8) Siarhel Spirydovich et al., "High density materials and radiotherapy planning: Comparison of the dose predictions using superposition algorithm and fluence map Monte Carlo method with radiochromic film measurements." *Radiother Oncol.* **81**, 309-314 (2006)

- 9) David W. Chin, Nathaniel Treister, Robert A. Cormack, et al., “Effect of dental restorations and prostheses on radiotherapy dose distribution: a Monte Carlo study.” Med. Phys. **10**, 80-89 (2009)
- 10) D. Sheikh-Bagheri and D. W. O. Rogers, “Monte Carlo calculation of nine megavoltage photon beam spectra using the BEAM code.” Med. Phys. **29**, 391-402 (2002)

Table1. The results of measurement

man	A	B	C	D	woman	A	B	C	D
1	2.21	11.27	2.45	8.84	1	1.76	10.21	2.7	6.97
2	2.22	12.71	2.51	8.65	2	1.95	11.68	2.45	7.03
3	1.2	10.88	1.38	6.15	3	1.88	8.31	2.51	6.77
4	1.64	9.31	2.01	5.59	4	1.86	8.32	2.51	6.33
5	1.39	10.73	1.44	7.28	5	1.95	12.15	2.78	7.59
6	1.38	11.92	1.76	7.02	6	1.82	10.88	2.82	7.98
7	1.78	11.27	2.57	6.09	7	1.66	9.1	1.88	6.84
8	1.51	11.81	2.13	6.08	8	0.98	7.7	1.51	4.33
9	1.63	9.38	2.07	6.33	9	1.24	7.9	1.51	4.01
10	1.56	10.04	1.88	6.58	10	1.37	11.35	2.32	7.27
11	1.46	11.72	1.88	8.03	11	1.43	11.24	2.26	6.72
12	1.55	12.08	2.38	6.27	12	1.55	9.73	2.38	5.58
13	1.6	11.91	2.26	6.84	13	1.25	8.7	2.08	4.73
14	1.53	12.31	2.08	8.04	14	1.19	9.42	1.94	5.7
15	1.44	10.25	2.01	6.65	15	1.17	9.69	2.09	6.93
Average	1.6	11.2	2.1	7.0	Average	1.5	9.8	2.2	6.3
SD	0.271	1.013	0.343	0.966	SD	0.314	1.394	0.399	1.154

Table2 The compositions of the materials

Materials	Element composition (%)	Density [g/cm ³]
Water	H(33.33) ,O(66.67)	1
PG-12	Au(12.0), Pd(20.0), Ag(54.0), Cu(12.0), Zn(1.00), Ru(1.00)	11
BM-HA	H(10.2), O(41.4), P(18.5), Ca(39.9)	3.225

Table3. The degree of the dose differences in case with and without gold crown

man	(A)+(B)		(C)+(D)	
thickness of the gold	near from the surface	remote from the surface	near from the surface	remote from the surface
1.0mm	13.66%	3.66%	12.12%	4.68%
woman	(A)+(B)		(C)+(D)	
thickness of the gold	near from the surface	remote from the surface	near from the surface	remote from the surface
1.0mm	13.05%	3.40%	10.58%	4.33%

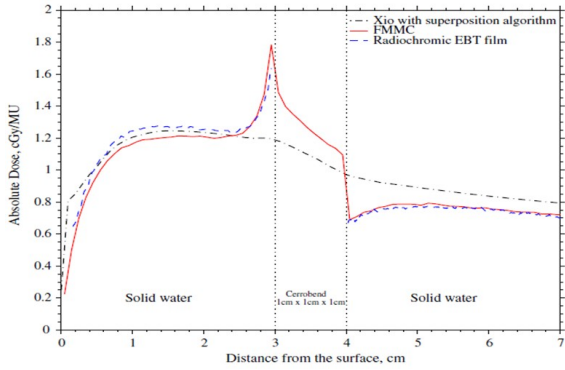


Fig1. The examples of the dose calculation

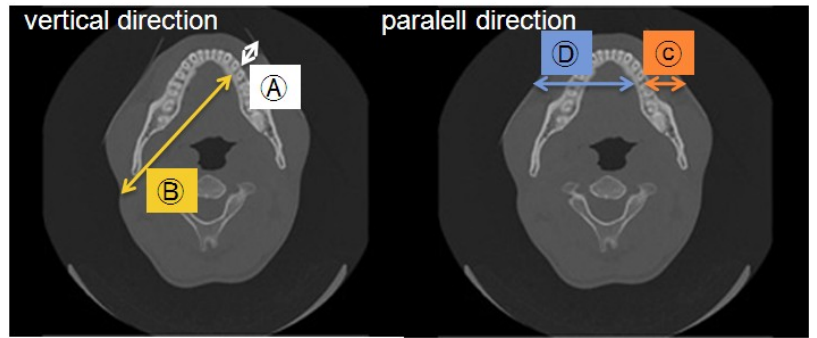


Fig2. Two directions of the measurement of the distance

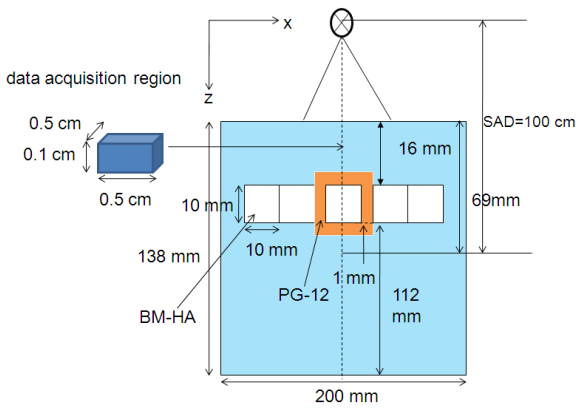


Fig.3 The geometry of MC simulation for the progress direction to the beam axis

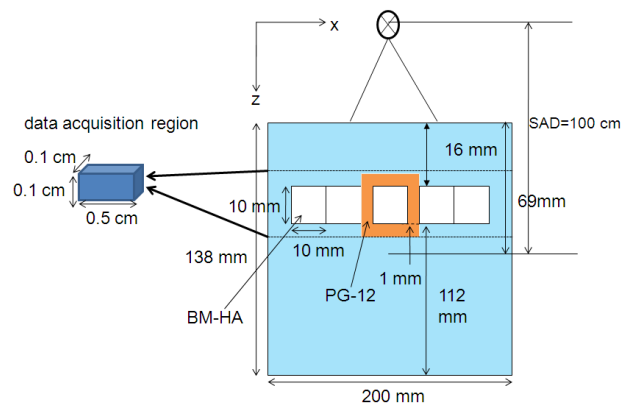


Fig.4 The geometry of MC simulation for the perpendicular direction to the beam axis

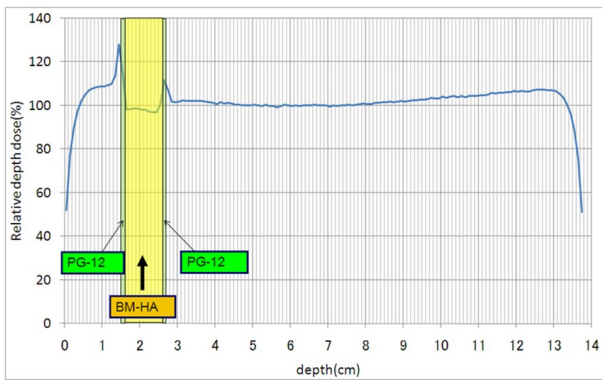


Fig.5 The relative dose of progress direction to beam axis for men with the gold crown in the vertical direction

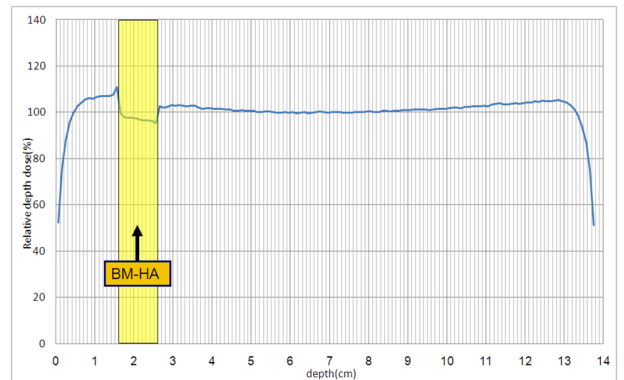


Fig.6 The relative dose of progress direction to beam axis for men without the gold crown in the vertical direction

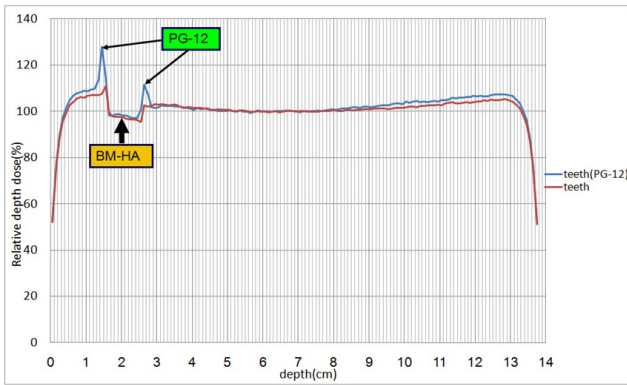


Fig.7 The comparison of relative dose with and without the gold crown for men

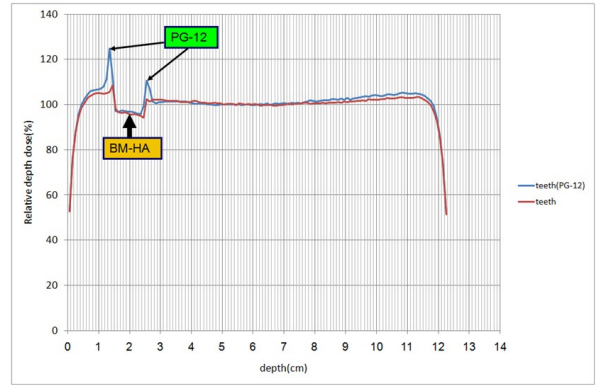


Fig.8 The comparison of relative dose with and without the gold crown for women

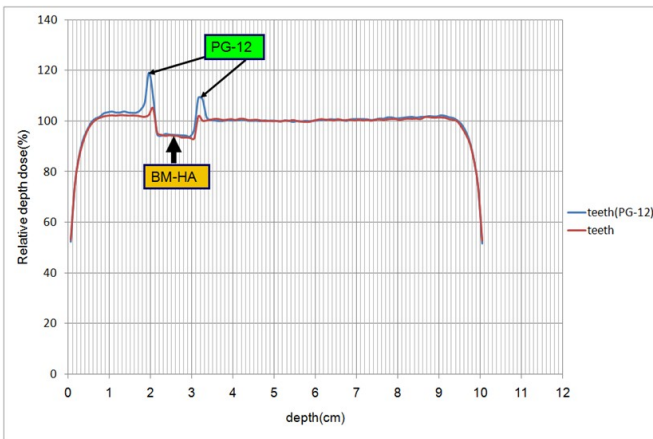


Fig.9 The comparison of relative dose with and without the gold crown for men in parallel direction

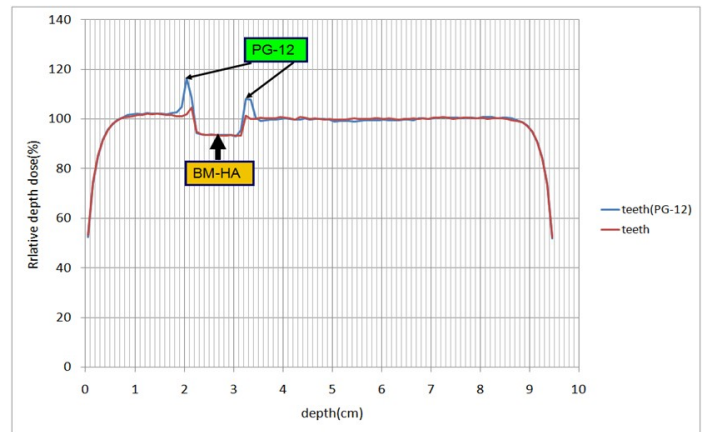


Fig.10 The comparison of relative dose with and without the gold crown for women in parallel direction

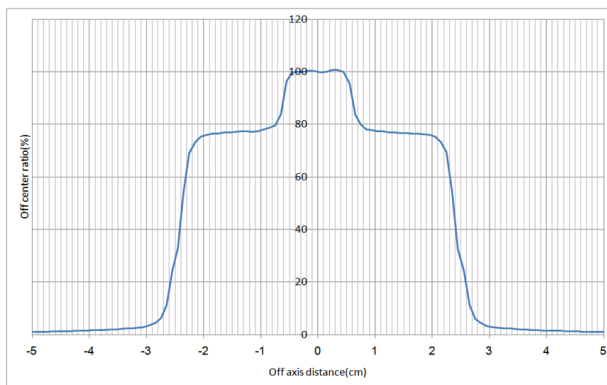


Fig.11 The relative dose of perpendicular direction to the beam axis for men in front of the gold crown

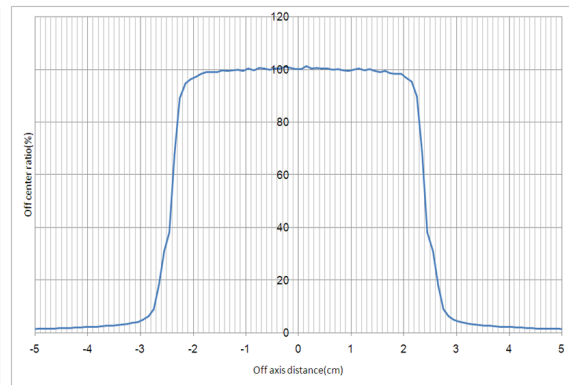


Fig.12 The relative dose of perpendicular direction to the beam axis for men in front of a row of teeth

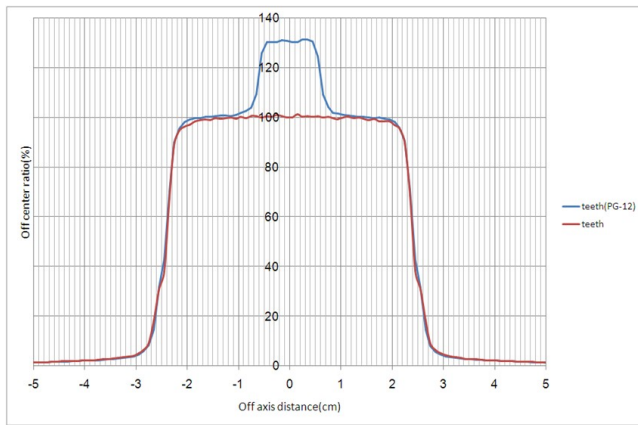


Fig.13 The comparison of relative dose with and without the gold crown for men

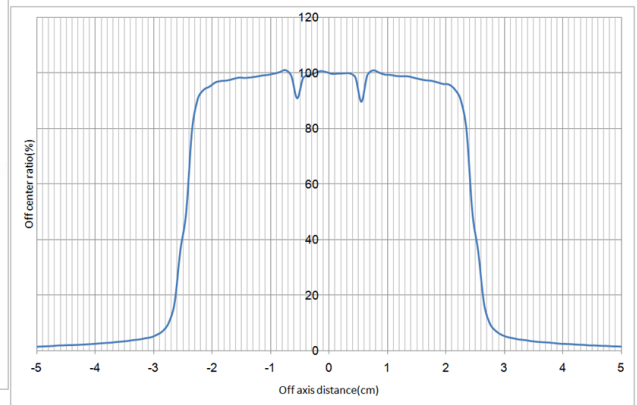


Fig.14 The relative dose of perpendicular direction to the beam axis for men in the back of the gold crown

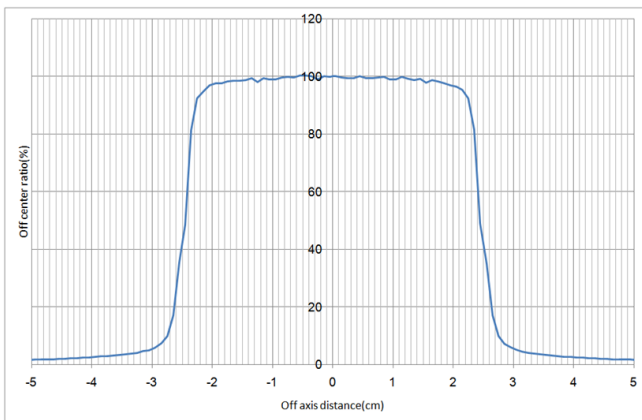


Fig.15 The relative dose of perpendicular direction to the beam axis for men in the back of a row of teeth

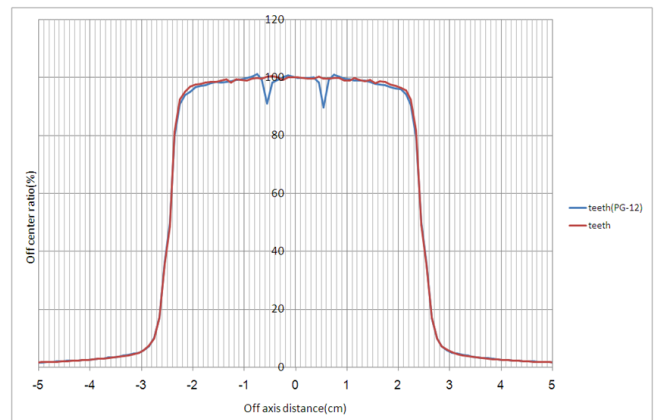


Fig.16 The comparison of relative dose with and without the gold crown for men

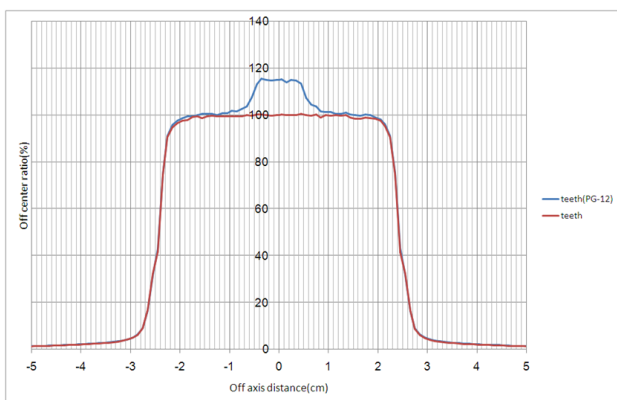


Fig.17 The comparison of relative dose with and without the gold crown for women

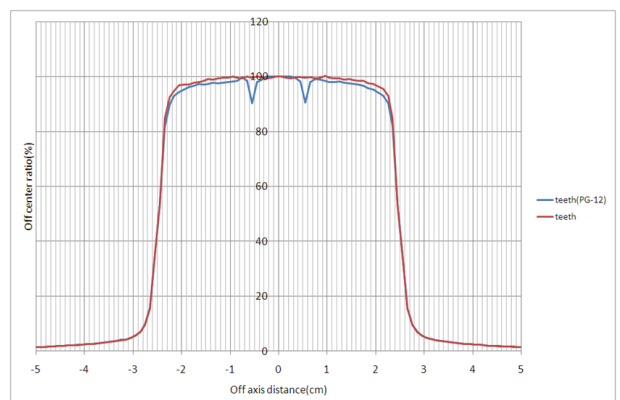


Fig.18 The comparison of relative dose with and without the gold crown for women

ELECTRON ABSORBED FRACTIONS AND S VALUES IN A MOUSE VOXEL PHANTOM

A. Mohammadi¹ and S. Kinase¹

¹Japan Atomic Energy Agency,
2-4 Shirakata, Shirane, Tokai-mura, Naka-gun, Ibaraki 319-1195, Japan
e-mail: mohammadi.akram@jaea.go.jp

Abstract

Electron absorbed fractions (AFs) and S values were evaluated in a voxel mouse phantom for preclinical evaluations of radiopharmaceuticals. The sources were considered to be mono-energetic in the electron energy range 10 keV to 4 MeV. The radiation transport was simulated using the Monte Carlo method. Consequently, it was confirmed that the electron AFs were dependent on the volume, density and geometry of the source/target organs. The electron AFs for organ self-absorption, i.e., target is source, decreased with increasing electron energy, which proved that it is certainly not always appropriate in small organs to assume a 100% localized electron energy absorption. The electron AFs for organ cross-fire depended on electron energy emitted by source and the geometries of source and target. In addition, S values in the major organs of the mouse phantom were tabulated for ¹³¹I, ¹⁵³Sm, ¹⁸⁸Re, ⁹⁰Y and ¹¹¹In using the results of the photon and electron AFs. Comparison of S values in abdominal organs for only β -spectrum of the nuclides demonstrated that β -only S values increased with increasing mean energy of β -spectrum of the nuclides. The results of this study will be useful in determining the dose to the organs for mice similar in size to the mouse in this study.

1. Introduction

Mice are frequently used in the development of new radiopharmaceuticals. Biodistribution and radiation toxicity studies of the agents are performed on mice to extrapolate preclinical results to human. Since more radiopharmaceuticals for therapy applications are tested on these animals, calculating accurate dose estimates for them has become important and indispensable. Organ doses of mice can be estimated from S values (Gy/Bq.s), mean absorbed dose to a target organ per unit cumulated activity in the source organ, using the Medical Internal Radiation Dose (MIRD) method. The S values can be calculated from absorbed fractions (AFs), fraction of energy emitted by a radiation source that is absorbed in a target organ, or specific absorbed fractions (kg^{-1}), absorbed fractions in a target per mass of target. To accomplish reliable mice dosimetry, the authors have evaluated photon specific absorbed fractions [1, 2] and photon-only S values [2] in a mouse voxel phantom. The objective of this study is evaluation of electron absorbed fractions and S values for the voxel mouse which was used in the previous work. Electron absorbed fractions were evaluated in the mouse phantom using the Monte Carlo method in the energy range 10 keV to 4 MeV then S values for ¹³¹I, ¹⁵³Sm, ¹⁸⁸Re, ⁹⁰Y and ¹¹¹In were tabulated for major organs.

2. Materials and Methods

2.1 Digimouse voxel phantom

The Digimouse voxel phantom was used [3]. The phantom was developed using co-registered micro-CT and color cryosection images of a normal nude male mouse at the University of Southern California. A matrix of 380×992×208 elements, with a voxel size of 0.1 mm was constructed. The 21 organs segmented from these data are: whole brain, external cerebrum, cerebellum, olfactory bulbs, striatum, medulla, masseter muscles, eyes, lachrymal glands, heart, lungs, liver, stomach, spleen, pancreas, adrenal glands, kidneys, testes, bladder, skeleton and skin.

2.2 Absorbed fractions

Electron AFs were evaluated for the Digimouse phantom by EGS4 [4] in conjunction with UCSAF [5], an EGS4 user code. In the EGS4-UCSAF code, the transport of electrons in the phantom was simulated and the correlations between primary and secondary particles are included. Elemental composition and density of the simulated organs were assumed the same as human tissues and they were taken from the Oak Ridge National Laboratory (ORNL) report [6]. Three different tissues were considered for the mouse organs including skeleton (1.40 g/cm³), soft tissue (1.04 g/cm³) and lungs (0.296 g/cm³). The mass of each organ was calculated from the number of voxels of the organ and the organ density. The volume and mass of organs of the Digimouse are given in **Table 1**.

All the organs were considered as targets and major organs were assumed as sources. Each source organ was evaluated separately in order to calculate the AFs from the absorbed energy within the organs. The source was distributed uniformly with isotropic emission in the major organs. Mono-energetic electrons were simulated for the desired source organs. Electron energies were 10, 15, 20, 30, 40, 30, 50, 100, 200, 500, 1000, 2000 and 4000 keV. The photon and electron cut-offs energy were set to 1 keV and the electron histories were run at numbers sufficient (3×10^6) to reduce uncertainties (fractional standard deviation [FSDs]) less than 5%. The cross section data for photons and electrons were taken from PHOTX [7, 8] and ICRU report 37 [9], respectively.

2.3 S values

S values in the major organs were calculated for the Digimouse phantom using electron and photon AFs. ¹³¹I, ¹⁵³Sm, ¹⁸⁸Re, ⁹⁰Y and ¹¹¹In were considered as interested nuclides for internal dosimetry. The photon AFs were taken from the authors' work [1, 2]. The AFs were converted to S values considering energies of emitted photons, electrons and β-spectra from the nuclides. The photons, electrons and β-spectra emitted for ¹³¹I, ¹⁵³Sm, ¹⁸⁸Re, ⁹⁰Y and ¹¹¹In were extracted from decay data [10]. **Table 2** shows mean and maximum energies of β-spectra for ¹³¹I, ¹⁵³Sm, ¹⁸⁸Re and ⁹⁰Y. β-only S values were also calculated using the electron AFs for the desired nuclides to demonstrate the effect of emitted electrons or photons on amount of S values .

3. Results and discussion

3.1 Absorbed fractions

Electron AFs in 13 identified organs including skeleton, eyes, medulla, external cerebrum, cerebellum, heart, stomach, spleen, pancreas, liver, kidneys, adrenal glands and lungs of the Digimouse were calculated at discrete initial electrons from 10 to 4000 keV. The electron AFs in the major organs for six source organs are given in **Table 3**. The AFs values set to zero when the FSDs exceed 5% to decrease uncertainty of calculating S values for the nuclides.

From table 3 it can be seen that electron AFs for organ self-absorption, target is source, decrease with increasing electron energy which proves that it is certainly not always appropriate in mouse organs to assume a 100% localized electron energy absorption (the standard MIRD assumption model for human). **Figure 1** compares electron AFs for organ self-absorption in the liver, stomach, heart, spleen and lungs. AFs in the liver have the highest values for all energies since the liver is the biggest organ among the organs in Figure 1. Differences between AFs in the stomach and heart, the organs with the same volume, are attributed to the effect of organ shape and geometry on AFs. Large differences between electron AFs in the lungs and spleen, the organs with very close masses, in Figure 1 demonstrates that electron AFs are dependent on organ density. **Figure 2** shows AFs for organ cross-fire in adjacent organs, i.e., skin, stomach, pancreas, liver and kidneys and in second-adjacent organs such as heart and lungs as source was in the spleen.

Electron AFs for second adjacent organs are very small for all energies although for adjacent organs it depends on energy and geometry of source and target.

Figure 3 shows a favorable comparison of electron AFs for organ self-absorption and cross-fire in liver and stomach reported by Bitar *et al.* [11] and Stabin *et al.* [12] with those observed in this work. The mass of liver in Bitar *et al.* and Stabin *et al.* studies were 1.83, 0.78 g, respectively. The electron AFs for low energy electrons, in which electron range is very smaller than organ dimensions, for organ self-absorption in three studies are 100% irrespective of mass differences. However, in the case that the electron range is comparable with organ dimensions, the differences are appeared between the results. The differences between the results of three studies for organ self-absorption and cross-fire are attributed to differences in the individual mouse organ volumes, densities and geometries. The electron AFs calculated in this work will be useful in obtaining the organ dose for mice similar in size to the Digimouse phantom.

3.2 S values

β -only S values in the liver, spleen, heart and kidneys of the Digimouse phantom for ^{131}I , ^{153}Sm , ^{188}Re and ^{90}Y are given in **Table 4**. From the table it can be seen that β -only S values for organ self-absorption and cross-fire increase with increasing mean energy of β -spectrum for the nuclides. Comparison of β -only S values and S values for all emissions in the liver and heart as source was in the liver are given in **Table 5**. The differences between two S values depend the fractions and the energies of electrons and photons emitted from the nuclides, ex., S value for all emissions in the heart for ^{131}I is more than twice of β -only S value. S values in the major organs of the Digimouse considering all particles emitted from ^{131}I , ^{153}Sm , ^{188}Re , ^{90}Y and ^{111}In are given in **Table 6**. Comparison of S values for organ cross-fire in the table shows validity of the reciprocal dose principle. **Figures 4** and **5** compare S value calculated for five nuclides in this study with values reported by Bitar *et al.* [11] and Stabin *et al.* [12] in liver and heart for organ self-absorption and cross-fire. The mass of heart in Bitar *et al.* and Stabin *et al.* studies are 0.28 and 0.14 g. Large differences can be observed between S values obtained for self-absorption for heart (or liver) owing to large difference between volume and density of heart (or liver) in three studies (Figure 4). The S values for organ cross-fire from Bitar *et al.* [11] study are very close to this work however there are large differences between this work and Stabin *et al.* [12] results which are attributed to the different geometry of the mouse phantoms.

4. Conclusions

The absorbed fractions (AFs) for electrons in the organs of the Digimouse phantom were evaluated using EGS4-UCSAF code. The new set of electron AFs were tabulated for the electron energies from 10 keV to 4 MeV in order to evaluate mouse organ doses in preclinical experiments of new radiopharmaceuticals. In this work, it was confirmed that a 100% localized electron energy absorption in source is particularly inaccurate for mouse organs. S values for ^{131}I , ^{153}Sm , ^{188}Re , ^{90}Y and ^{111}In were calculated in the major organs of the Digimouse phantom. Organ dose evaluation for a mouse should be performed in a voxel phantom of that mouse with the Monte Carlo method since electron AFs and S values are strongly dependent on volume, density and the geometry of the organs.

Acknowledgments

The authors would like to thank Dr. Ishioka, the group leader of medical radioisotope application group, Japan Atomic Energy Agency, for her support to this work.

References

- 1) A. Mohammadi and S. Kinase, "Monte Carlo simulations of photon specific absorbed fractions in a mouse voxel phantom," Prog. Nucl. Sci. Tech. (in press)
- 2) A. Mohammadi and S. Kinase, "Simulations of photon specific absorbed fractions in a mouse voxel phantom," KEK Proceedings 2009-6, 70-77 (2009)

- 3) B. Dogdas, D. Stout, A. F. Chatziioannou and R. M. Leahy, "Digimouse: a 3D whole body mouse atlas from CT and cryosection data," *Phys. Med. Biol.* 52, 577 (2007).
- 4) W. R. Nelson, H. Hirayama and D. W. O. Rogers, "The EGS4 Code System," SLAC-265 (1985).
- 5) S. Kinase, M. Zankl, *et al.*, "Evaluation of specific absorbed fractions in voxel phantoms using Monte Carlo simulation," *Radiat. Prot. Dosi.* 105, 557 (2003).
- 6) M. Cristy, K. F. Eckerman, "Specific absorbed fractions of energy at various ages from internal photon sources", Report ORNL/TM-8381: Vol. 1-7 (Oak Ridge National Laboratory, Oak Ridge, Tennessee) (1987).
- 7) "Photon Interaction Cross Section Library," DLC-136/PHOTX, contributed by National Institute of Standards and Technology (1989).
- 8) Y. Sakamoto, "Photon cross section data PHOTX for PEGS4," KEK Proceedings 93-15, 77-82(in Japanese).
- 9) "Stopping Powers for Electrons and Positrons," ICRU Report 37 International Commission on Radiation Units and Measurements (1984).
- 10) A., Endo and Y. Yamaguchi (2001), "Compilation of Nuclear Decay Data Used for Dose Calculation Revised Data for Radionuclides Listed in ICRP Publication 38", JAERI-Data/Code 2001-004.
- 11) A. Bitar, A. Lisbona, P. Thedrez, C. S. Maurel, D. L. Forestier, J. Barbet and M. Bardies, "A voxel-based mouse for internal dose calculations using Monte Carlo simulations (MCNP)," *Phys. Med. Biol.* 52, 1013 (2007).
- 12) M. G. Stabin, T. E. Peterson, G. E. Holburn and M. A. Emmons, "Voxel-based mouse and rat models for internal dose calculations," *J. Nucl. Med.* 47, 655 (2006).

Table 1 The volume and mass of organs of the Digimouse

Organ	Volume (cm ³)	Mass (g)
Skin	1.67×10 ¹	1.74×10 ¹
Skeleton	1.18×10 ⁰	1.66×10 ⁰
Eyes	5.61×10 ⁻³	5.83×10 ⁻³
Medulla	4.58×10 ⁻²	4.76×10 ⁻²
Striatum	2.60×10 ⁻²	2.71×10 ⁻²
Olfactory bulbs	1.85×10 ⁻²	1.92×10 ⁻²
External cerebrum	1.37×10 ⁻¹	1.42×10 ⁻¹
Cerebellum	3.06×10 ⁻²	3.18×10 ⁻²
Heart	2.23×10 ⁻¹	2.32×10 ⁻¹
Rest of the brain	1.59×10 ⁻¹	1.65×10 ⁻¹
Masseter muscles	1.07×10 ⁻¹	1.12×10 ⁻¹
Lachrymal glands	3.04×10 ⁻²	3.16×10 ⁻²
Bladder	1.90×10 ⁻¹	1.97×10 ⁻¹
Testis	1.49×10 ⁻¹	1.55×10 ⁻¹
Stomach	2.26×10 ⁻¹	2.35×10 ⁻¹
Spleen	1.39×10 ⁻¹	1.44×10 ⁻¹
Pancreas	4.47×10 ⁻²	4.65×10 ⁻²
Liver	2.01×10 ⁰	2.09×10 ⁰
Kidneys	4.95×10 ⁻¹	5.15×10 ⁻¹
Adrenal glands	5.71×10 ⁻³	5.94×10 ⁻³
Lungs	4.17×10 ⁻¹	1.24×10 ⁻¹

Table 2 Mean and maximum energies of β -spectrum for ¹³¹I, ¹⁵³Sm, ¹⁸⁸Re, and ⁹⁰Y

Nuclide	Mean energy (keV)	Max energy (keV)
¹³¹ I	182	806
¹⁵³ Sm	225	810
¹⁸⁸ Re	763	2120
⁹⁰ Y	934	2281

Table 3 Electron absorbed fractions (AFs) in major organs of the Digimouse phantom (1/2)

Source organ : Heart									
Energy (keV)	Heart	Bladder	Stomach	Spleen	Pancreas	Liver	Kidneys	Adrenal	Lungs
10	1.0×10 ⁰	0.0×10 ⁰	0.0×10 ⁰	0.0×10 ⁰	0.0×10 ⁰	0.0×10 ⁰	0.0×10 ⁰	0.0×10 ⁰	0.0×10 ⁰
15	1.0×10 ⁰	0.0×10 ⁰	0.0×10 ⁰	0.0×10 ⁰	0.0×10 ⁰	0.0×10 ⁰	0.0×10 ⁰	0.0×10 ⁰	0.0×10 ⁰
20	1.0×10 ⁰	0.0×10 ⁰	0.0×10 ⁰	0.0×10 ⁰	0.0×10 ⁰	1.1×10 ⁻⁴	0.0×10 ⁰	0.0×10 ⁰	0.0×10 ⁰
30	1.0×10 ⁰	0.0×10 ⁰	0.0×10 ⁰	0.0×10 ⁰	0.0×10 ⁰	2.3×10 ⁻⁴	0.0×10 ⁰	0.0×10 ⁰	2.1×10 ⁻⁴
50	9.9×10 ⁻¹	0.0×10 ⁰	0.0×10 ⁰	0.0×10 ⁰	0.0×10 ⁰	6.2×10 ⁻⁴	0.0×10 ⁰	0.0×10 ⁰	4.9×10 ⁻⁴
100	9.8×10 ⁻¹	0.0×10 ⁰	0.0×10 ⁰	0.0×10 ⁰	0.0×10 ⁰	1.8×10 ⁻³	0.0×10 ⁰	0.0×10 ⁰	1.5×10 ⁻³
200	9.5×10 ⁻¹	0.0×10 ⁰	0.0×10 ⁰	0.0×10 ⁰	0.0×10 ⁰	5.3×10 ⁻³	0.0×10 ⁰	0.0×10 ⁰	7.7×10 ⁻³
500	8.1×10 ⁻¹	0.0×10 ⁰	0.0×10 ⁰	0.0×10 ⁰	0.0×10 ⁰	2.4×10 ⁻²	0.0×10 ⁰	0.0×10 ⁰	4.1×10 ⁻²
1000	5.8×10 ⁻¹	0.0×10 ⁰	0.0×10 ⁰	0.0×10 ⁰	0.0×10 ⁰	6.2×10 ⁻²	0.0×10 ⁰	0.0×10 ⁰	5.7×10 ⁻²
2000	2.8×10 ⁻¹	0.0×10 ⁰	2.7×10 ⁻⁴	0.0×10 ⁰	0.0×10 ⁰	1.0×10 ⁻¹	0.0×10 ⁰	0.0×10 ⁰	4.1×10 ⁻²
4000	1.3×10 ⁻¹	0.0×10 ⁰	4.9×10 ⁻³	1.0×10 ⁻³	2.6×10 ⁻⁴	8.5×10 ⁻²	1.4×10 ⁻³	8.9×10 ⁻⁵	1.8×10 ⁻²
Source organ : Liver									
Energy (keV)	Heart	Bladder	Stomach	Spleen	Pancreas	Liver	Kidneys	Adrenal	Lungs
10	0.0×10 ⁰	0.0×10 ⁰	0.0×10 ⁰	0.0×10 ⁰	0.0×10 ⁰	1.0×10 ⁰	0.0×10 ⁰	0.0×10 ⁰	0.0×10 ⁰
15	0.0×10 ⁰	0.0×10 ⁰	0.0×10 ⁰	0.0×10 ⁰	0.0×10 ⁰	1.0×10 ⁰	0.0×10 ⁰	0.0×10 ⁰	0.0×10 ⁰
20	0.0×10 ⁰	0.0×10 ⁰	0.0×10 ⁰	0.0×10 ⁰	0.0×10 ⁰	1.0×10 ⁰	0.0×10 ⁰	0.0×10 ⁰	0.0×10 ⁰
30	0.0×10 ⁰	0.0×10 ⁰	0.0×10 ⁰	0.0×10 ⁰	0.0×10 ⁰	1.0×10 ⁰	0.0×10 ⁰	0.0×10 ⁰	1.3×10 ⁻⁴
50	0.0×10 ⁰	0.0×10 ⁰	2.5×10 ⁻⁴	0.0×10 ⁰	0.0×10 ⁰	9.9×10 ⁻¹	1.5×10 ⁻⁴	0.0×10 ⁰	3.1×10 ⁻⁴
100	2.0×10 ⁻⁴	0.0×10 ⁰	7.1×10 ⁻⁴	0.0×10 ⁰	0.0×10 ⁰	9.8×10 ⁻¹	4.4×10 ⁻⁴	0.0×10 ⁰	8.6×10 ⁻⁴
200	6.1×10 ⁻⁴	0.0×10 ⁰	2.2×10 ⁻³	1.7×10 ⁻⁴	2.7×10 ⁻⁴	9.6×10 ⁻¹	1.4×10 ⁻³	1.2×10 ⁻⁴	2.5×10 ⁻³
500	2.7×10 ⁻³	0.0×10 ⁰	1.0×10 ⁻²	8.6×10 ⁻⁴	1.1×10 ⁻³	8.6×10 ⁻¹	6.3×10 ⁻³	5.5×10 ⁻⁴	6.8×10 ⁻³
1000	6.9×10 ⁻³	0.0×10 ⁰	2.1×10 ⁻²	2.2×10 ⁻³	1.5×10 ⁻³	7.1×10 ⁻¹	1.5×10 ⁻²	9.5×10 ⁻⁴	9.5×10 ⁻³
2000	1.1×10 ⁻²	0.0×10 ⁰	2.6×10 ⁻²	4.5×10 ⁻³	1.7×10 ⁻³	4.9×10 ⁻¹	2.1×10 ⁻²	8.5×10 ⁻⁴	1.0×10 ⁻²
4000	9.5×10 ⁻³	1.1×10 ⁻³	1.6×10 ⁻²	5.0×10 ⁻³	1.8×10 ⁻³	2.6×10 ⁻¹	2.0×10 ⁻²	5.2×10 ⁻⁴	6.5×10 ⁻³
Source organ : Lungs									
Energy (keV)	Heart	Bladder	Stomach	Spleen	Pancreas	Liver	Kidneys	Adrenal	Lungs
10	0.0×10 ⁰	0.0×10 ⁰	0.0×10 ⁰	0.0×10 ⁰	0.0×10 ⁰	0.0×10 ⁰	0.0×10 ⁰	0.0×10 ⁰	1.0×10 ⁰
15	0.0×10 ⁰	0.0×10 ⁰	0.0×10 ⁰	0.0×10 ⁰	0.0×10 ⁰	4.8×10 ⁻⁴	0.0×10 ⁰	0.0×10 ⁰	1.0×10 ⁰
20	1.8×10 ⁻⁴	0.0×10 ⁰	0.0×10 ⁰	0.0×10 ⁰	0.0×10 ⁰	9.9×10 ⁻⁴	0.0×10 ⁰	0.0×10 ⁰	9.9×10 ⁻¹
30	3.9×10 ⁻⁴	0.0×10 ⁰	0.0×10 ⁰	0.0×10 ⁰	0.0×10 ⁰	2.2×10 ⁻³	0.0×10 ⁰	0.0×10 ⁰	9.9×10 ⁻¹
50	9.1×10 ⁻⁴	0.0×10 ⁰	0.0×10 ⁰	0.0×10 ⁰	0.0×10 ⁰	5.2×10 ⁻³	0.0×10 ⁰	0.0×10 ⁰	9.7×10 ⁻¹
100	2.7×10 ⁻³	0.0×10 ⁰	0.0×10 ⁰	0.0×10 ⁰	0.0×10 ⁰	1.5×10 ⁻²	0.0×10 ⁰	0.0×10 ⁰	9.1×10 ⁻¹
200	1.4×10 ⁻²	0.0×10 ⁰	0.0×10 ⁰	0.0×10 ⁰	0.0×10 ⁰	4.2×10 ⁻²	0.0×10 ⁰	0.0×10 ⁰	7.6×10 ⁻¹
500	7.6×10 ⁻²	0.0×10 ⁰	0.0×10 ⁰	0.0×10 ⁰	0.0×10 ⁰	1.2×10 ⁻¹	0.0×10 ⁰	0.0×10 ⁰	3.9×10 ⁻¹
1000	1.1×10 ⁻¹	0.0×10 ⁰	0.0×10 ⁰	0.0×10 ⁰	0.0×10 ⁰	1.6×10 ⁻¹	0.0×10 ⁰	0.0×10 ⁰	1.8×10 ⁻¹
2000	7.4×10 ⁻²	0.0×10 ⁰	2.8×10 ⁻³	5.6×10 ⁻⁵	0.0×10 ⁰	1.7×10 ⁻¹	0.0×10 ⁰	0.0×10 ⁰	8.2×10 ⁻²
4000	3.2×10 ⁻²	0.0×10 ⁰	6.2×10 ⁻³	1.7×10 ⁻³	4.6×10 ⁻⁴	1.0×10 ⁻¹	4.3×10 ⁻³	1.7×10 ⁻⁴	3.8×10 ⁻²

AFs were set to zero when statistical uncertainty exceeds 5%.

Table 3 Electron absorbed fractions (AFs) in major organs of the Digimouse phantom (2/2)

Source organ : Kidneys									
Energy (keV)	Heart	Bladder	Stomach	Spleen	Pancreas	Liver	Kidneys	Adrenal	Lungs
10	0.0×10 ⁰	0.0×10 ⁰	0.0×10 ⁰	0.0×10 ⁰	0.0×10 ⁰	0.0×10 ⁰	1.0×10 ⁰	0.0×10 ⁰	0.0×10 ⁰
15	0.0×10 ⁰	0.0×10 ⁰	0.0×10 ⁰	0.0×10 ⁰	0.0×10 ⁰	0.0×10 ⁰	1.0×10 ⁰	0.0×10 ⁰	0.0×10 ⁰
20	0.0×10 ⁰	0.0×10 ⁰	0.0×10 ⁰	0.0×10 ⁰	0.0×10 ⁰	1.1×10 ⁻⁴	1.0×10 ⁰	0.0×10 ⁰	0.0×10 ⁰
30	0.0×10 ⁰	0.0×10 ⁰	0.0×10 ⁰	0.0×10 ⁰	1.5×10 ⁻⁴	2.6×10 ⁻⁴	1.0×10 ⁰	0.0×10 ⁰	0.0×10 ⁰
50	0.0×10 ⁰	0.0×10 ⁰	0.0×10 ⁰	0.0×10 ⁰	3.4×10 ⁻⁴	6.0×10 ⁻⁴	9.9×10 ⁻¹	0.0×10 ⁰	0.0×10 ⁰
100	0.0×10 ⁰	0.0×10 ⁰	0.0×10 ⁰	0.0×10 ⁰	1.0×10 ⁻³	1.8×10 ⁻³	9.8×10 ⁻¹	0.0×10 ⁰	0.0×10 ⁰
200	0.0×10 ⁰	0.0×10 ⁰	0.0×10 ⁰	3.7×10 ⁻⁴	2.7×10 ⁻³	5.5×10 ⁻³	9.5×10 ⁻¹	0.0×10 ⁰	0.0×10 ⁰
500	0.0×10 ⁰	0.0×10 ⁰	6.6×10 ⁻⁵	3.8×10 ⁻³	9.2×10 ⁻³	2.6×10 ⁻²	8.3×10 ⁻¹	4.4×10 ⁻⁴	0.0×10 ⁰
1000	0.0×10 ⁰	0.0×10 ⁰	2.1×10 ⁻³	1.1×10 ⁻²	1.4×10 ⁻²	6.1×10 ⁻²	6.0×10 ⁻¹	1.3×10 ⁻³	0.0×10 ⁰
2000	0.0×10 ⁰	1.3×10 ⁻⁴	1.3×10 ⁻²	1.5×10 ⁻²	1.2×10 ⁻²	8.6×10 ⁻²	3.0×10 ⁻¹	1.2×10 ⁻³	0.0×10 ⁰
4000	6.7×10 ⁻⁴	4.2×10 ⁻³	1.1×10 ⁻²	8.8×10 ⁻³	5.6×10 ⁻³	8.2×10 ⁻²	1.4×10 ⁻¹	6.4×10 ⁻⁴	9.7×10 ⁻⁴
Source organ : Spleen									
Energy (keV)	Heart	Bladder	Stomach	Spleen	Pancreas	Liver	Kidneys	Adrenal	Lungs
10	0.0×10 ⁰	0.0×10 ⁰	0.0×10 ⁰	1.0×10 ⁰	0.0×10 ⁰	0.0×10 ⁰	0.0×10 ⁰	0.0×10 ⁰	0.0×10 ⁰
15	0.0×10 ⁰	0.0×10 ⁰	0.0×10 ⁰	1.0×10 ⁰	0.0×10 ⁰	0.0×10 ⁰	0.0×10 ⁰	0.0×10 ⁰	0.0×10 ⁰
20	0.0×10 ⁰	0.0×10 ⁰	1.5×10 ⁻⁴	1.0×10 ⁰	0.0×10 ⁰	0.0×10 ⁰	0.0×10 ⁰	0.0×10 ⁰	0.0×10 ⁰
30	0.0×10 ⁰	0.0×10 ⁰	3.1×10 ⁻⁴	1.0×10 ⁰	1.6×10 ⁻⁴	1.2×10 ⁻⁴	0.0×10 ⁰	0.0×10 ⁰	0.0×10 ⁰
50	0.0×10 ⁰	0.0×10 ⁰	7.6×10 ⁻⁴	9.9×10 ⁻¹	4.2×10 ⁻⁴	2.9×10 ⁻⁴	0.0×10 ⁰	0.0×10 ⁰	0.0×10 ⁰
100	0.0×10 ⁰	0.0×10 ⁰	2.2×10 ⁻³	9.7×10 ⁻¹	1.2×10 ⁻³	8.4×10 ⁻⁴	2.3×10 ⁻⁴	0.0×10 ⁰	0.0×10 ⁰
200	0.0×10 ⁰	0.0×10 ⁰	6.5×10 ⁻³	9.1×10 ⁻¹	3.7×10 ⁻³	2.6×10 ⁻³	1.3×10 ⁻³	0.0×10 ⁰	0.0×10 ⁰
500	0.0×10 ⁰	0.0×10 ⁰	3.4×10 ⁻²	6.9×10 ⁻¹	1.6×10 ⁻²	1.2×10 ⁻²	1.4×10 ⁻²	2.8×10 ⁻⁴	0.0×10 ⁰
1000	0.0×10 ⁰	0.0×10 ⁰	8.0×10 ⁻²	3.9×10 ⁻¹	2.7×10 ⁻²	3.1×10 ⁻²	4.0×10 ⁻²	9.7×10 ⁻⁴	0.0×10 ⁰
2000	0.0×10 ⁰	0.0×10 ⁰	8.0×10 ⁻²	1.8×10 ⁻¹	2.0×10 ⁻²	6.4×10 ⁻²	5.4×10 ⁻²	7.6×10 ⁻⁴	4.4×10 ⁻⁵
4000	1.6×10 ⁻³	0.0×10 ⁰	3.6×10 ⁻²	8.5×10 ⁻²	8.8×10 ⁻³	7.2×10 ⁻²	3.1×10 ⁻²	4.6×10 ⁻⁴	1.4×10 ⁻³
Source organ : Pancreas									
Energy (keV)	Heart	Bladder	Stomach	Spleen	Pancreas	Liver	Kidneys	Adrenal	Lungs
10	0.0×10 ⁰	0.0×10 ⁰	0.0×10 ⁰	0.0×10 ⁰	1.0×10 ⁰	0.0×10 ⁰	0.0×10 ⁰	0.0×10 ⁰	0.0×10 ⁰
15	0.0×10 ⁰	0.0×10 ⁰	0.0×10 ⁰	0.0×10 ⁰	1.0×10 ⁰	0.0×10 ⁰	3.5×10 ⁻⁴	0.0×10 ⁰	0.0×10 ⁰
20	0.0×10 ⁰	0.0×10 ⁰	0.0×10 ⁰	2.3×10 ⁻⁴	1.0×10 ⁰	2.2×10 ⁻⁴	7.3×10 ⁻⁴	0.0×10 ⁰	0.0×10 ⁰
30	0.0×10 ⁰	0.0×10 ⁰	0.0×10 ⁰	5.1×10 ⁻⁴	9.9×10 ⁻¹	5.1×10 ⁻⁴	1.6×10 ⁻³	0.0×10 ⁰	0.0×10 ⁰
50	0.0×10 ⁰	0.0×10 ⁰	1.9×10 ⁻⁴	1.2×10 ⁻³	9.8×10 ⁻¹	1.2×10 ⁻³	3.9×10 ⁻³	0.0×10 ⁰	0.0×10 ⁰
100	0.0×10 ⁰	0.0×10 ⁰	6.2×10 ⁻⁴	3.6×10 ⁻³	9.5×10 ⁻¹	3.6×10 ⁻³	1.1×10 ⁻²	0.0×10 ⁰	0.0×10 ⁰
200	0.0×10 ⁰	0.0×10 ⁰	2.6×10 ⁻³	1.1×10 ⁻²	8.6×10 ⁻¹	1.2×10 ⁻²	3.0×10 ⁻²	0.0×10 ⁰	0.0×10 ⁰
500	0.0×10 ⁰	0.0×10 ⁰	1.7×10 ⁻²	4.9×10 ⁻²	5.4×10 ⁻¹	4.8×10 ⁻²	1.0×10 ⁻¹	1.0×10 ⁻⁴	0.0×10 ⁰
1000	0.0×10 ⁰	0.0×10 ⁰	4.5×10 ⁻²	8.3×10 ⁻²	2.5×10 ⁻¹	6.8×10 ⁻²	1.6×10 ⁻¹	1.1×10 ⁻³	0.0×10 ⁰
2000	0.0×10 ⁰	0.0×10 ⁰	6.1×10 ⁻²	6.1×10 ⁻²	1.1×10 ⁻¹	7.9×10 ⁻²	1.3×10 ⁻¹	9.1×10 ⁻⁴	0.0×10 ⁰
4000	1.4×10 ⁻³	2.6×10 ⁻³	2.9×10 ⁻²	2.7×10 ⁻²	5.4×10 ⁻²	8.2×10 ⁻²	6.2×10 ⁻²	5.2×10 ⁻⁴	1.2×10 ⁻³

AFs were set to zero when statistical uncertainty exceeds 5%.

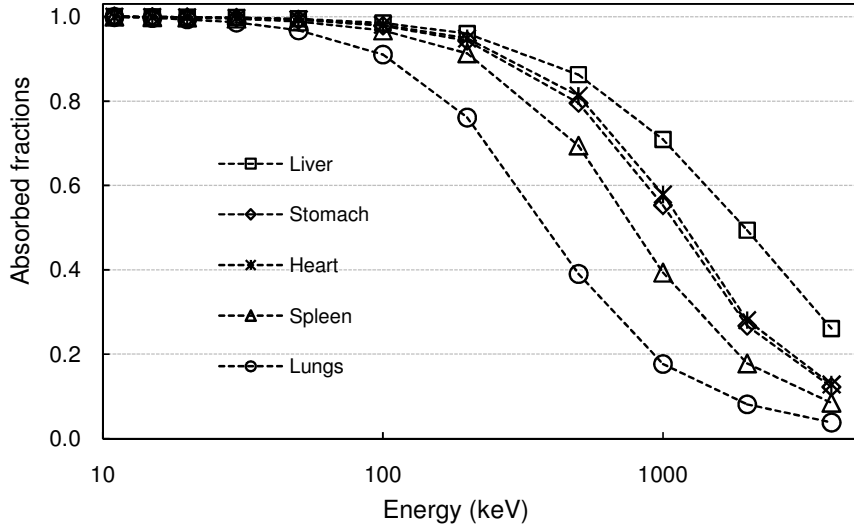


Figure 1. Comparison of electron absorbed fractions (AFs) for organ self-absorption in some organs.

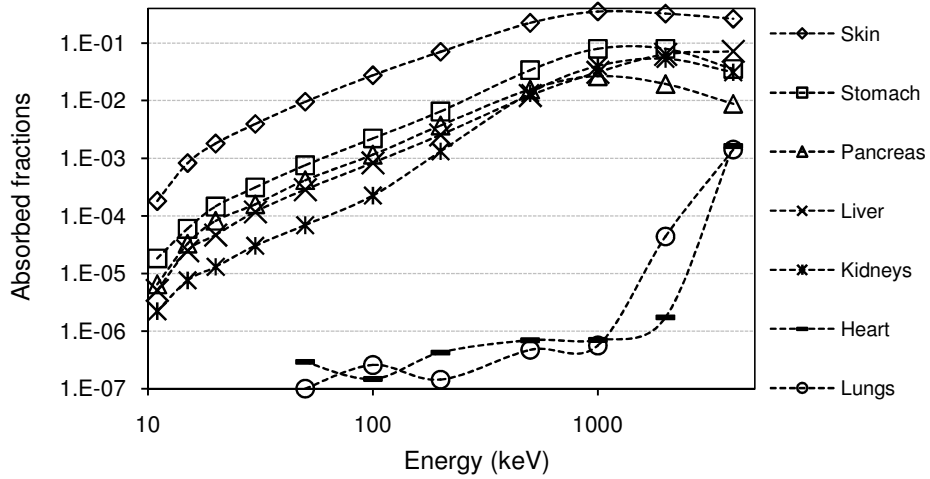


Figure 2. Comparison of electron absorbed fractions (AFs) for organ cross-fire in some organs (source = spleen).

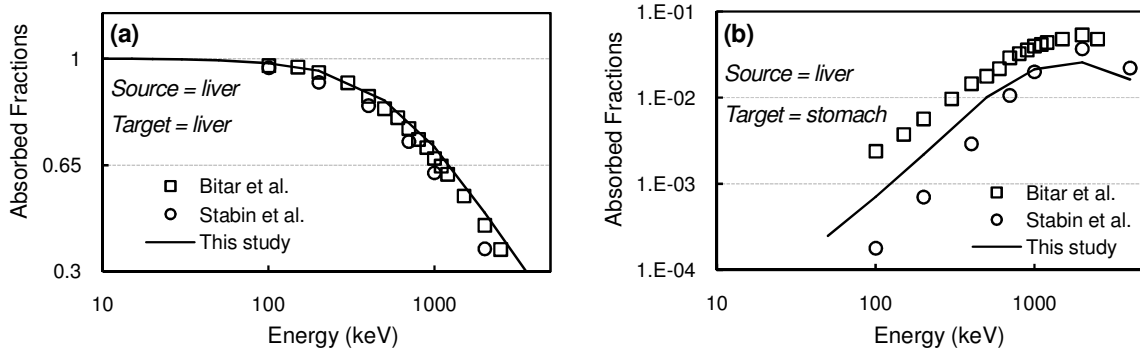


Figure 3. Comparison of electron absorbed fractions (AFs) for this study with Bitar *et al.*[11] and Stabin *et al.*[12] studies in (a) liver and (b) stomach (source = liver).

Table 4 β -only S values ($\mu\text{Gy}/\text{MBq}\cdot\text{s}$) in some organs of the Digimouse phantom for ^{131}I , ^{153}Sm , ^{188}Re and ^{90}Y

Nuclide	Target	Source organs			
		Liver	Spleen	Heart	Kidneys
^{131}I	Liver	1.28×10^1	7.16×10^{-2}	1.43×10^{-1}	1.50×10^{-1}
	Spleen	7.02×10^{-2}	1.70×10^2	0.00×10^0	2.65×10^{-1}
	Heart	1.43×10^{-1}	0.00×10^0	1.13×10^2	0.00×10^0
	Kidneys	1.51×10^{-1}	2.64×10^{-1}	0.00×10^0	5.13×10^1
^{153}Sm	Liver	1.56×10^1	1.19×10^{-1}	2.35×10^{-1}	2.47×10^{-1}
	Spleen	1.18×10^{-1}	2.02×10^2	0.00×10^0	4.82×10^{-1}
	Heart	2.35×10^{-1}	0.00×10^0	1.37×10^2	0.00×10^0
	Kidneys	2.49×10^{-1}	4.78×10^{-1}	0.00×10^0	6.21×10^1
^{188}Re	Liver	4.17×10^1	1.91×10^0	3.57×10^0	3.33×10^0
	Spleen	1.92×10^0	3.62×10^2	0.00×10^0	8.75×10^0
	Heart	3.57×10^0	0.00×10^0	3.05×10^2	0.00×10^0
	Kidneys	3.32×10^0	8.76×10^0	0.00×10^0	1.42×10^2
^{90}Y	Liver	4.78×10^1	2.84×10^0	5.14×10^0	4.62×10^0
	Spleen	2.86×10^0	3.78×10^2	1.74×10^{-4}	1.22×10^2
	Heart	5.14×10^0	1.79×10^{-4}	3.28×10^2	0.00×10^0
	Kidneys	4.61×10^0	1.22×10^1	0.00×10^0	1.54×10^2

Table 5 Comparison of β -only S values ($\mu\text{Gy}/\text{MBq}\cdot\text{s}$) and S values for all emissions in liver and heart of the Digimouse phantom for ^{131}I , ^{153}Sm , ^{188}Re and ^{90}Y (source = liver)

Nuclide	Target	β -only	All emissions
^{131}I	Liver	1.28×10^1	1.40×10^1
	Heart	1.43×10^{-1}	3.06×10^{-1}
^{153}Sm	Liver	1.56×10^1	1.95×10^1
	Heart	2.35×10^{-1}	2.74×10^{-1}
^{188}Re	Liver	4.17×10^1	4.30×10^1
	Heart	3.57×10^0	3.59×10^0
^{90}Y	Liver	4.78×10^1	4.78×10^1
	Heart	5.14×10^0	5.14×10^0

Table 6 S values ($\mu\text{Gy}/\text{MBq}\cdot\text{s}$) in major organs of the Digimouse phantom for ^{111}In , ^{131}I , ^{153}Sm , ^{188}Re and ^{90}Y

Nuclide : ^{111}In								
	Source organs							
Target	Heart	Stomach	Spleen	Pancreas	Liver	Kidneys	Adrenal	Lungs
Heart	2.68×10^1	9.87×10^{-2}	5.45×10^{-2}	5.08×10^{-2}	2.24×10^{-1}	4.10×10^{-2}	7.49×10^{-2}	1.06×10^0
Stomach	9.85×10^{-2}	2.62×10^1	9.57×10^1	7.01×10^1	3.98×10^1	2.27×10^1	3.53×10^1	1.17×10^1
Spleen	5.46×10^{-2}	9.53×10^1	4.01×10^1	1.41×10^0	1.78×10^1	3.36×10^1	4.05×10^1	6.53×10^2
Pancreas	5.00×10^{-2}	6.98×10^1	1.42×10^0	1.15×10^2	2.27×10^1	9.08×10^1	4.55×10^1	5.51×10^2
Liver	2.25×10^1	3.98×10^1	1.79×10^1	2.27×10^1	3.31×10^0	2.14×10^1	5.38×10^1	3.40×10^1
Kidneys	4.06×10^{-2}	2.29×10^1	3.39×10^1	9.09×10^1	2.15×10^1	1.23×10^1	5.72×10^1	5.38×10^2
Adrenal	1.26×10^{-2}	3.48×10^1	4.19×10^1	4.38×10^1	5.06×10^1	5.58×10^1	8.31×10^2	2.32×10^2
Lungs	1.10×10^0	1.20×10^1	6.70×10^2	5.91×10^2	3.51×10^1	5.46×10^{-2}	1.17×10^1	3.95×10^1
Nuclide : ^{131}I								
Heart	1.22×10^2	7.87×10^{-2}	4.62×10^{-2}	4.33×10^{-2}	3.06×10^{-1}	3.54×10^{-2}	6.01×10^{-2}	4.86×10^0
Stomach	7.98×10^{-2}	1.19×10^2	2.44×10^0	1.32×10^0	8.23×10^{-1}	1.69×10^{-1}	2.51×10^{-1}	9.11×10^2
Spleen	4.50×10^{-2}	2.45×10^0	1.82×10^2	5.37×10^0	2.03×10^{-1}	5.19×10^{-1}	6.88×10^{-1}	5.26×10^2
Pancreas	4.22×10^{-2}	1.31×10^0	5.39×10^0	5.04×10^2	4.76×10^{-1}	3.44×10^0	4.83×10^{-1}	4.58×10^2
Liver	3.06×10^{-1}	8.23×10^{-1}	2.05×10^1	4.74×10^1	1.40×10^1	3.07×10^{-1}	1.55×10^0	1.08×10^0
Kidneys	3.54×10^{-2}	1.70×10^1	5.18×10^1	3.43×10^0	3.08×10^{-1}	5.53×10^1	1.06×10^0	4.53×10^2
Adrenal	0.00×10^0	2.56×10^1	6.87×10^1	4.73×10^1	1.52×10^0	1.07×10^0	3.32×10^3	0.00×10^0
Lungs	4.88×10^0	8.91×10^{-2}	5.46×10^{-2}	4.82×10^{-2}	1.09×10^0	4.53×10^{-2}	8.87×10^{-2}	1.61×10^2
Nuclide : ^{153}Sm								
Heart	1.71×10^2	1.76×10^{-2}	1.00×10^{-2}	9.48×10^{-3}	2.74×10^{-1}	7.73×10^{-3}	1.34×10^{-2}	6.81×10^0
Stomach	1.73×10^{-2}	1.67×10^2	3.08×10^0	1.49×10^0	9.46×10^{-1}	4.41×10^{-2}	6.16×10^{-2}	2.05×10^2
Spleen	1.00×10^{-2}	3.09×10^0	2.56×10^2	7.33×10^0	1.46×10^{-1}	5.39×10^{-1}	8.22×10^{-1}	1.16×10^2
Pancreas	9.39×10^{-3}	1.48×10^0	7.36×10^0	7.11×10^2	5.22×10^{-1}	4.53×10^0	4.29×10^{-1}	1.05×10^2
Liver	2.76×10^{-1}	9.43×10^{-1}	1.49×10^1	5.27×10^1	1.95×10^1	2.86×10^{-1}	1.97×10^0	1.34×10^0
Kidneys	7.83×10^{-3}	4.40×10^{-2}	5.37×10^{-1}	4.52×10^0	2.88×10^{-1}	7.77×10^1	1.31×10^0	9.90×10^{-3}
Adrenal	0.00×10^0	6.09×10^{-2}	8.48×10^{-1}	4.27×10^{-1}	1.94×10^0	1.31×10^0	4.74×10^3	0.00×10^0
Lungs	6.84×10^0	2.15×10^{-2}	1.24×10^{-2}	1.16×10^{-2}	1.35×10^0	1.07×10^{-2}	2.12×10^{-2}	2.30×10^2
Nuclide : ^{188}Re								
Heart	3.16×10^2	3.18×10^{-2}	6.25×10^{-3}	5.86×10^{-3}	3.59×10^0	4.81×10^{-3}	8.19×10^{-3}	4.79×10^1
Stomach	2.91×10^{-2}	3.01×10^2	3.65×10^1	2.22×10^1	1.03×10^1	1.95×10^0	3.50×10^0	2.42×10^1
Spleen	6.24×10^{-3}	3.65×10^1	3.79×10^2	5.91×10^1	1.94×10^0	8.79×10^0	1.53×10^1	1.34×10^2
Pancreas	5.82×10^{-3}	2.21×10^1	5.90×10^1	8.48×10^2	3.74×10^0	3.34×10^1	1.69×10^1	6.26×10^3
Liver	3.60×10^0	1.03×10^1	1.93×10^0	3.75×10^0	4.30×10^1	3.35×10^0	1.70×10^1	8.78×10^0
Kidneys	4.81×10^{-3}	1.95×10^0	8.80×10^0	3.34×10^1	3.35×10^0	1.47×10^2	2.15×10^1	6.11×10^{-3}
Adrenal	0.00×10^0	3.50×10^0	1.56×10^1	1.70×10^1	1.70×10^1	2.15×10^1	4.21×10^3	6.59×10^4
Lungs	4.88×10^1	2.24×10^{-1}	1.30×10^{-2}	6.56×10^{-3}	8.87×10^0	6.21×10^{-3}	5.25×10^{-2}	2.38×10^2
Nuclide : ^{90}Y								
Heart	3.28×10^2	5.24×10^{-2}	1.80×10^{-4}	1.49×10^{-4}	5.14×10^0	0.00×10^0	3.80×10^{-4}	5.79×10^1
Stomach	4.58×10^{-2}	3.10×10^2	4.80×10^1	3.10×10^1	1.38×10^1	3.56×10^0	6.75×10^0	5.38×10^1
Spleen	1.75×10^{-4}	4.79×10^1	3.78×10^2	7.27×10^1	2.87×10^0	1.22×10^1	1.98×10^1	1.55×10^2
Pancreas	1.43×10^{-4}	3.08×10^1	7.26×10^1	8.07×10^2	4.84×10^0	4.16×10^1	2.23×10^1	2.49×10^4
Liver	5.15×10^0	1.38×10^1	2.84×10^0	4.86×10^0	4.78×10^1	4.62×10^0	2.16×10^1	1.12×10^1
Kidneys	0.00×10^0	3.53×10^0	1.23×10^1	4.16×10^1	4.61×10^0	1.54×10^2	2.82×10^1	2.11×10^4
Adrenal	3.78×10^{-4}	6.73×10^0	2.00×10^1	2.24×10^1	2.16×10^1	2.82×10^1	3.73×10^3	7.05×10^4
Lungs	5.93×10^1	4.99×10^{-1}	1.44×10^{-2}	2.48×10^{-4}	1.13×10^1	1.99×10^{-4}	9.96×10^{-2}	2.22×10^2

S values were set to zero when it was $< 10^{-4}$

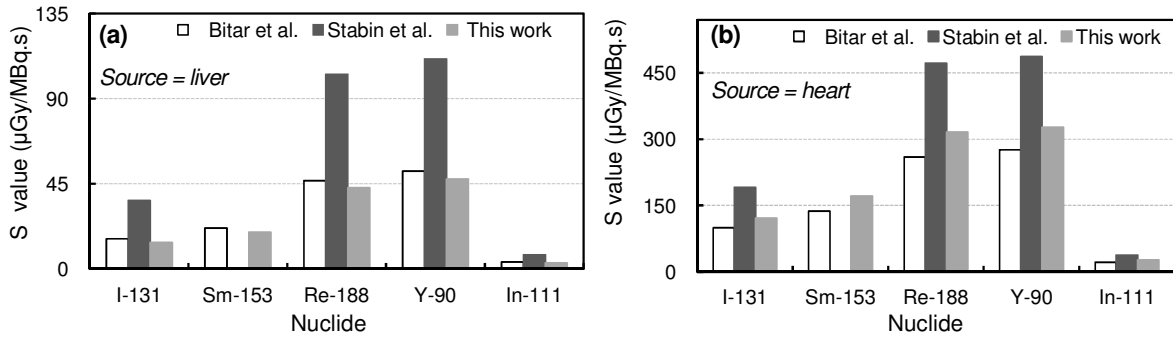


Figure 4. Comparison of S values (μGy/MBq.s) for organ self-absorption for ^{131}I , ^{153}Sm , ^{188}Re , ^{90}Y and ^{111}In in this work with Bitar *et al.* [11] and Stabin *et al.* [12] studies for (a) source=liver and (b) source=heart.

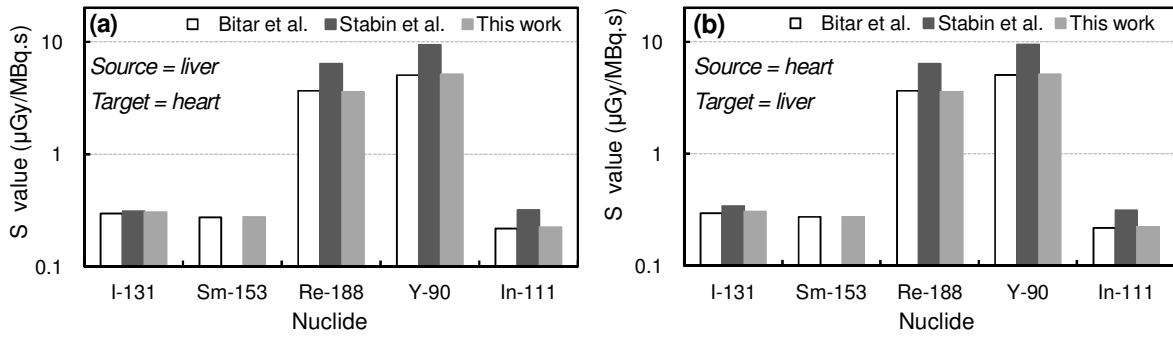


Figure 5. Comparison of S values (μGy/MBq.s) for cross-irradiation for ^{131}I , ^{153}Sm , ^{188}Re , ^{90}Y and ^{111}In in this work with Bitar *et al.* [11] and Stabin *et al.* [12] studies for (a) Source=liver and target=heart. (b) Source=heart and target=liver.

CALCULATION OF DOSE EQUIVALENT FOR POSITRONS USING THE MONTE CARLO CODE EGS5

T. Kato¹, K. Aoki², S. Yokoyama², K. Minami², H. Yashima³, A. Taniguchi³, T. Nakamura⁴,
and H. Hirayama⁵

¹ *Toyohashi Municipal Hospital*

50, Hachikennishi, Aotake, Toyohashi, Aichi 441-8570, Japan

² *Fujita Health University of Health Sciences,*

1-93, Denrakugakubo, Kutsukake, Toyoake, Aichi 470-1192, Japan

³ *Kyoto University Research Reactor Institute,*

2-1010, Asashironishi, Kumatori, Sennan, Osaka 590-0494, Japan

⁴ *Nagoya Central Hospital,*

3-7-7, Taikou, Nakamura, Nagoya, Aichi 453-0801, Japan

⁵ *High Energy Accelerator Research Organization (KEK),*

1-1, Oho, Tsukuba, Ibaraki 305-0801, Japan

e-mail: sumi0704@fujita-hu.ac.jp

Abstract

Medical staff face the risk of chronic exposure to the annihilation photons generated by the positrons emitted from the radiopharmaceutical 2-deoxy-2-[¹⁸F]fluoro-D-glucose (¹⁸F-FDG) while administering it to patients for positron emission tomography (PET). In order to assess doses for this exposure, an EGS5 user code, UCF18DOSE, was developed to calculate the dose equivalent rates for positron. The energy spectra of positrons and photons used in the dose calculations were confirmed by the good agreement between the calculated pulse height distribution for a ¹⁸F point source and measurements recorded on scintillation counters. The dose rates calculated for a ¹⁸F-FDG line source were compared with those measured by a personal dosimeter at tissue depths of 70 μ m and 1 cm. There is qualitative agreement between those results.

1. Introduction

The radiopharmaceutical 2-deoxy-2-[¹⁸F] fluoro-D-glucose (¹⁸F-FDG) is used in positron emission tomography (PET) for determining the location of malignant tumours and diagnosis of cardiac conditions. ¹⁸F emits positrons with a maximum energy of 0.633 MeV, which when annihilated, generate two 0.511 MeV photons per positron. Thus, these photons constitute the main source of chronic radiation exposure for the medical staff at these facilities [1,2]. In addition, our measurements have shown that the dose equivalent at 70 μ m depth was greater at points closer to a syringe containing ¹⁸F-FDG, which could be significant for nurses [3].

The objective of this study is to estimate the dose received by medical staff in the field where positrons and photons are exist such as PET examination facilities. The conversion coefficients from fluence to dose equivalent can be calculated using an EGS5 [4] user code called UCICRPM, because the values for positrons have not yet been determined. Here we describe a newly developed user code, UCF18DOSE, for estimating the dose received by medical staff from

positrons and annihilation photons emerging from a straight line source. The results of trial calculations of the dose equivalents at tissue depths of 70 μm and 1 cm are presented. The energy spectrum of the particles used in the calculation was confirmed by comparison with the estimates of UCF18SPECT and the measurements at the field where positrons emitted from radionuclides exist. The estimates calculated by the developed code were compared with dose equivalents measured near a straight-line ^{18}F source.

2. Measurement and calculation methods

2-1 Estimation of dose equivalent by calculation and measurement

An EGS5 user code, UCF18DOSE, was developed in order to calculate the dose rates at tissue depths of 70 μm and 1 cm in the vicinity of a straight line source of ^{18}F . Figure 1 shows the geometry of the radiation field. The region of interest is air (dimensions: 4.0 cm wide \times 1.0 cm deep \times 4.0 cm high). It was arranged parallel with the floor at a height of 40 cm and at a distance of 20 cm, 40 cm and 60 cm from the center of the line source. This geometry is in agreement with the geometry of the experimental field. For this code, the dose rate was calculated by using the following parameters: the changing energy spectrum due to the energy deposition in air and various materials around the source, and the conversion coefficients.

The personal dose equivalent rates at 70 μm and 1 cm depths were measured. The activity of a straight line source of ^{18}F in a polybutadiene tube (length: 1120 mm, outside diameter: 2.1, mm and inside diameter: 1.1 mm) with 1.4 ml ^{18}F -FDG is about 97.4 MBq at the start of a measurement. The personal dose meter employs a silicon semiconductor detector (DOSE³, Chiyoda Technol. Co., Tokyo).

2-2 Confirmation of energy spectrum

The energy spectra of ^{18}F used in the above calculation were confirmed by comparing the energy pulse height of a ^{18}F point source calculated by UCF18SPEC and that measured by using the NaI(Tl) and plastic scintillation counters. In the calculation, the geometry of the radiation field and counters was as indicated in Figure 2. This geometry is in agreement with the geometry of the experimental field. The regions of crystal for NaI(Tl) counter and polyvinyltoluene for plastic counter were regarded as those of interest for positrons and photons. The calculated energy spectra were normalized to unit activity (Bq) and unit energy bin width (MeV).

The energy spectra of the positrons and annihilation photons were measured by using a NaI(Tl) scintillation counter (Type: S-2361, Ohyo Koken Kogyo Co., Ltd.) and a plastic scintillation counter (NE102A, Ohyo Koken Kogyo Co., Ltd.) with a photomultiplier tube (Hamamatsu Photonics K. K.). A ^{18}F point source was made by dropping 1 μl of ^{18}F -FDG on a filter paper (height: 5.5 cm, width: 8.5 cm width; ADVANTEC, 5A, Toyo Roshi Kaisha, Ltd.) which was kept on a small plastic tray of thickness 0.043 mm. The activity of the point source was 30.5 kBq at the start of the measurement of a dose. The surface of NaI(Tl) scintillation counter or plastic scintillation counter was set up at a distance of 5 cm from the source.

The characteristic spread of spectra for detectors was simulated by a FORTRAN program, GAUSS. The full widths at half maximum (FWHM) for the NaI(Tl) and the plastic counters were obtained from the measured results of the total absorption peak and the Compton edge of a point source of ^{137}Cs , respectively. These values obtained for NaI(Tl) and plastic scintillation counters were 0.124 MeV and 0.0485 MeV, respectively.

2-3 Calculation of dose conversion coefficients for positrons

The conversion coefficients for monoenergetic positrons were calculated by using UCICRPM, an EGS5 user code developed to convert the fluence of particles at the body surface into the dose. UCICRPM is derived from UCICRP, an EGS4 user code [5]. The UCICRPM estimates of the conversion coefficients for monoenergetic electrons at tissue depths of 70 μm and 1 cm ($H'(0.07,0^\circ)/\Phi$ and $H'(10,0^\circ)/\Phi$) lie within about 10 % of the values reported in ICRP Publication 74 [6]. In the dose estimates for photon by UCF18DOSE, The conversion coefficients were used in ICRP Publ. 74. The conversion coefficients for positrons are described in detail in another paper [7].

3. Results and Discussion

3-1 Energy spectrum of the radionuclide ^{18}F

Figure 3 shows the pulse height distributions at 5 cm from a ^{18}F point source as calculated by UCF18SPEC and measured by using the plastic scintillation counter. The calculated peak values correspond with the measured values. As a result, there was relatively good agreement between the calculated and the measured values, except for the values lower than 0.1 MeV. The reason for the difference in the lower-energy area could be because the plastic scintillation counter had a minimum detection limit to reduce electric noise. The pulse height distribution calculated by UCF18SPEC and that measured by the NaI(Tl) scintillation counter are shown in Figure 4. The calculated values also correspond to the measured values, showing that the energy spectra used in the dose calculation by UCF18DOSE can be computed with a high degree of precision.

3-2 Equivalent dose rates for positrons

The contributions of positrons and photons to the total dose equivalent rates at 70 μm and 1 cm depths at 20 cm, 40 cm and 60 cm are indicated in Figures 5 and 6. The contribution of positrons to the total dose equivalent rate at 70 μm depth at 20 cm is about 70%. It decreases to about 50% and 25% at 40 and 60 cm, respectively. Photons make a great contribution to the total dose equivalent rates, as shown in Figure 6. Positrons emitted from ^{18}F do not reach a tissue depth of 1 cm, and only have a maximum penetration of about 2 mm in tissue.

The dose equivalent rates at 70 μm and 1 cm depths per unit activity measured by the dosimeter were 0.245 $\text{pSv min}^{-1} \text{Bq}^{-1}$ and 0.0597 $\text{pSv min}^{-1} \text{Bq}^{-1}$, respectively, at 20 cm from the ^{18}F tube line source. These dose rates decreased with increasing distance. Both the calculated and measured results show a tendency to decrease with increased distance, though the measured results at 70 μm and 1 cm at 20 cm were about 2.1 and 1.7 times higher than the calculated results for the total of positrons and photons at the same distance, respectively. This difference between the calculated and the measured results would be supposed that the model of the normally broad incident beam were used in the calculation of conversion coefficients. For a comparison between the calculated and the measured results, it is necessary to reproduce the detailed detector geometry of the dosimeter (used for dose measurement), in the calculation.

4. Conclusions

An EGS 5 user code, UCF18DOSE, was developed to assess the dose received by medical staff at PET examination facilities. The energy spectrum needed for the dose calculation was calculated by an EGS 5 user code, UCF18SPEC, and compared with the energy pulse height measured by NaI(Tl) and plastic scintillation counters. The conversion coefficients used in UCF18DOSE were calculated by the UCICRPM code. The calculated and the measured energy spectra were in good agreement, confirming that UCF18SPEC could be used for the calculation of the energy spectra. UCF18DOSE estimated that the contribution of positrons to total dose equivalent rate at 70 μm depth was about 70% at a distance of 20 cm from a straight tube source. The ratio of positrons decreased with distance. Positrons do not significantly contribute to the total dose equivalent rate at 1 cm depth. The calculated total dose equivalent rate at both 70 μm and 1 cm were smaller than the measured results. From this result, the details of the structure and the material of the dosimeter would be important for calculation purposes.

Acknowledgments

This study was begun under the supervision of the late Dr. Kazutaka Ejiri, associate professor at Fujita Health University. We acknowledge his guidance and pray that his soul may rest in peace.

References

- 1) K. Minami, K. Ejiri, H. Toyama, Y. Saito, K. Nishikawa, S. Sawara, K. Kawabata, A. Tsuruta, Y. Tsuruta, and K. Katada, Occupational radiation exposure from ^{18}F -FDG in a PET clinic. Japanese Association for Cancer Detection and Diagnosis. 14. 177-181 (2007).
- 2) G. Brix, U. Lechel, G. Glatting, S. I. Ziegler, W. Muenzing, S. P. Mueller, and T. Beyer, Radiation exposure of patients undergoing whole-body dual-modality ^{18}F -FDG PET/CT examinations. J. Nucl. Med. 46, 608-613 (2005).
- 3) T. Kato, K. Ejiri, and K. Minami, Positron leak from a syringe and a tube used for F-18-FDG medication. Eur. J. Nucl. Med. Mol. Imaging. 35, 383-384 (2008).
- 4) H. Hirayama, Y. Namito, A. F. Bielajew, S. J. Wilderman, and W. R. Nelson, The EGS5 code system. SLAC-730, Stanford Linear Accelerator (2004).
- 5) H. Hirayama, Calculation of absorbed dose at 0.07, 3.0 and 10.0 mm depths in a slab phantom for monoenergetic electrons. Radiat. Prot. Dosim. 51, 107-124 (1994).
- 6) ICRP. 1977 Recommendations of the International Commission on Radiological Protection. ICRP Publication 74 (Oxford: Pergamon Press) (1996). ISBN-13: 978-0-08-042739-3.
- 7) T. Kato, S. Yokoyama, K. Ejiri, K. Minami, H. Yashima, A. Taniguchi, T. Nakamura, H. Hirayama, Calculation of Direction Dose Equivalent due to the Positron Emitters Using the Monte Carlo Code EGS5. The Third Asian and Oceanic Congress on Radiation Protection Proceedings, 7, p-23, CD-ROM, (2010) (closed).

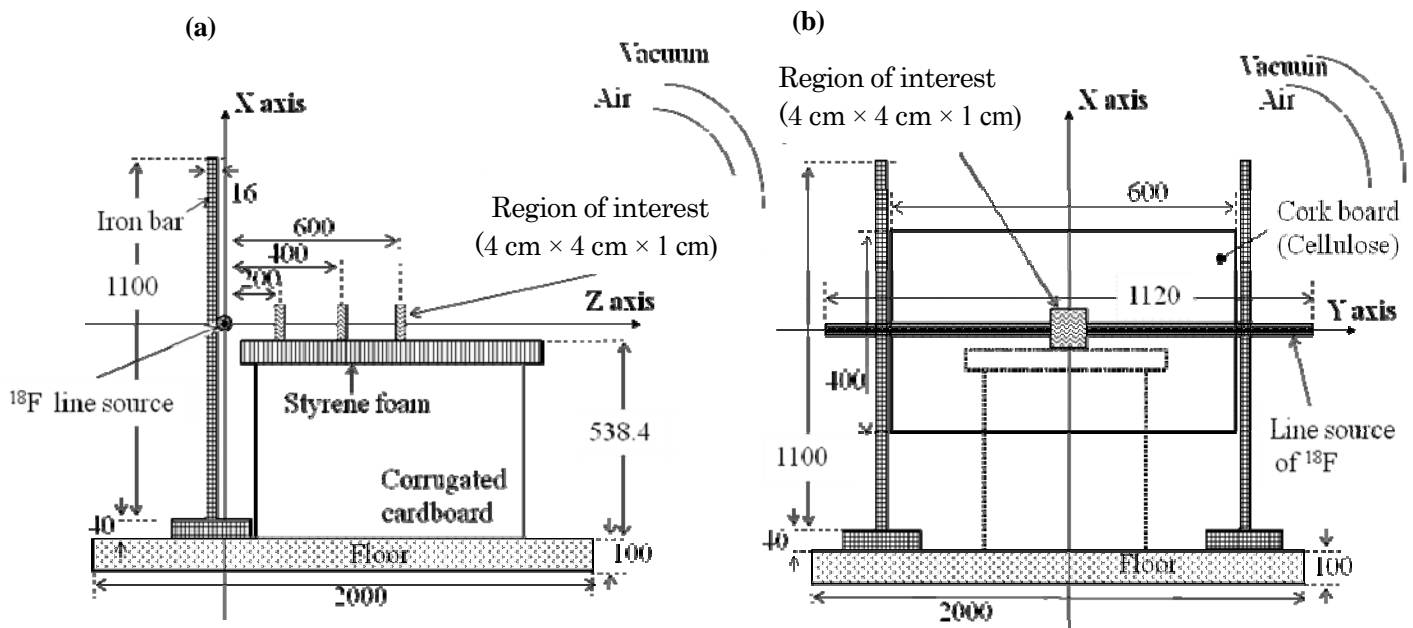


Figure 1. The geometric condition for UCF18DOSE. All dimensions are in millimeters. All the structures are in an air-filled ball with a radius of 3000 mm. (a) Short axis view and (b) Long axis view of ^{18}F line source.

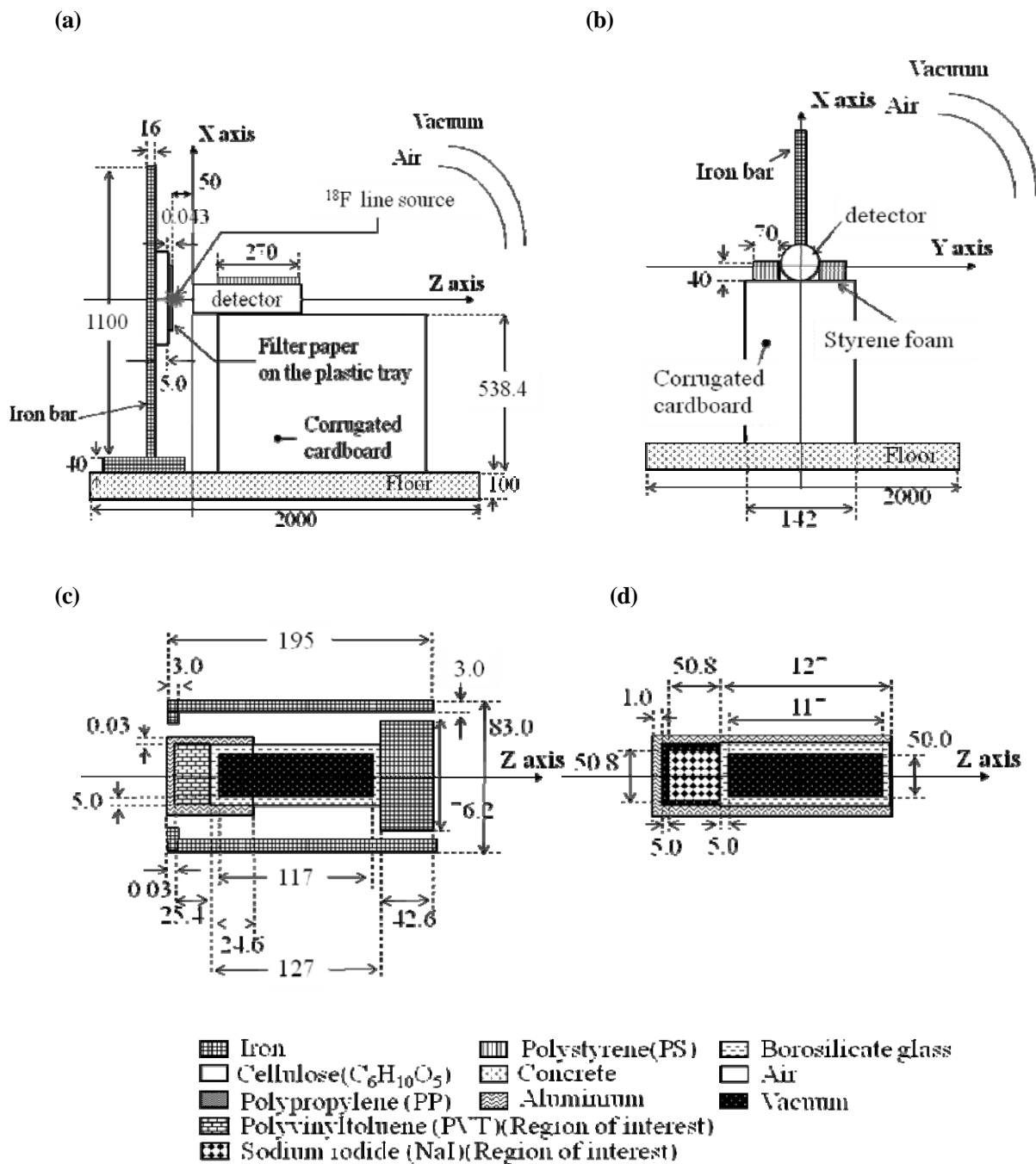


Figure 2. The geometric condition for UCF18SPECT. All dimensions are in millimeters. All the structures are in an air-filled ball with a radius of 3000 mm. (a) long axis view and (b) short axis view of the detector. (c) geometry of plastic scintillation counter and (d) geometry of NaI(Tl) scintillation counter.

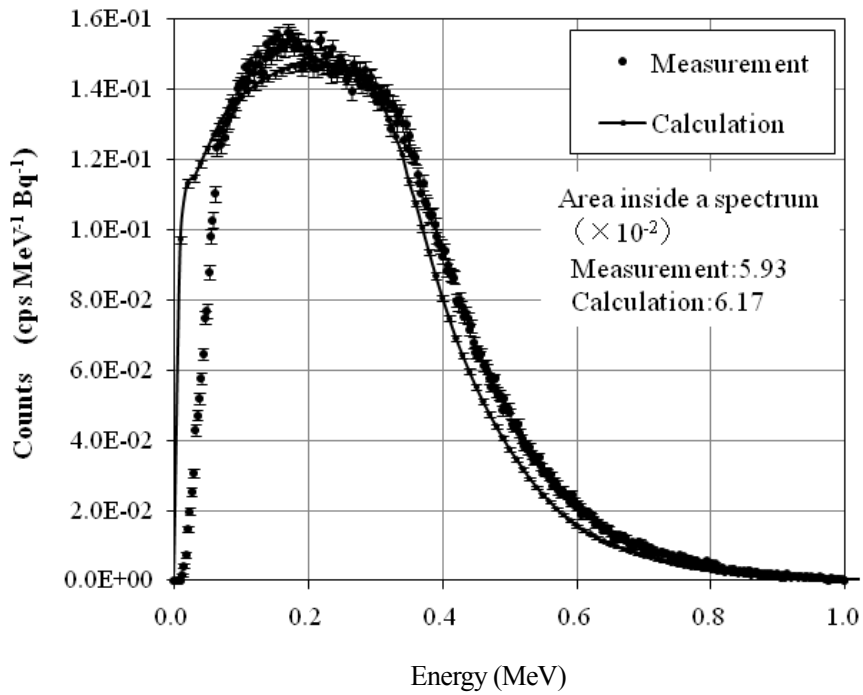


Figure 3. Calculated and measured pulse height distribution (plastic scintillation counter).

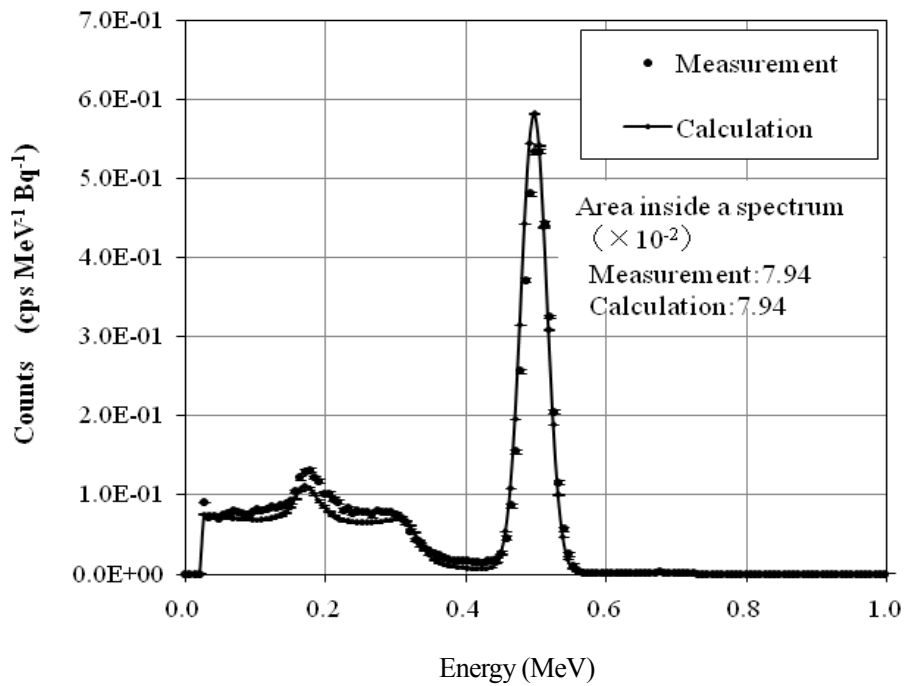


Figure 4. Calculation and measured pulse height distribution (NaI(Tl) scintillation counter).

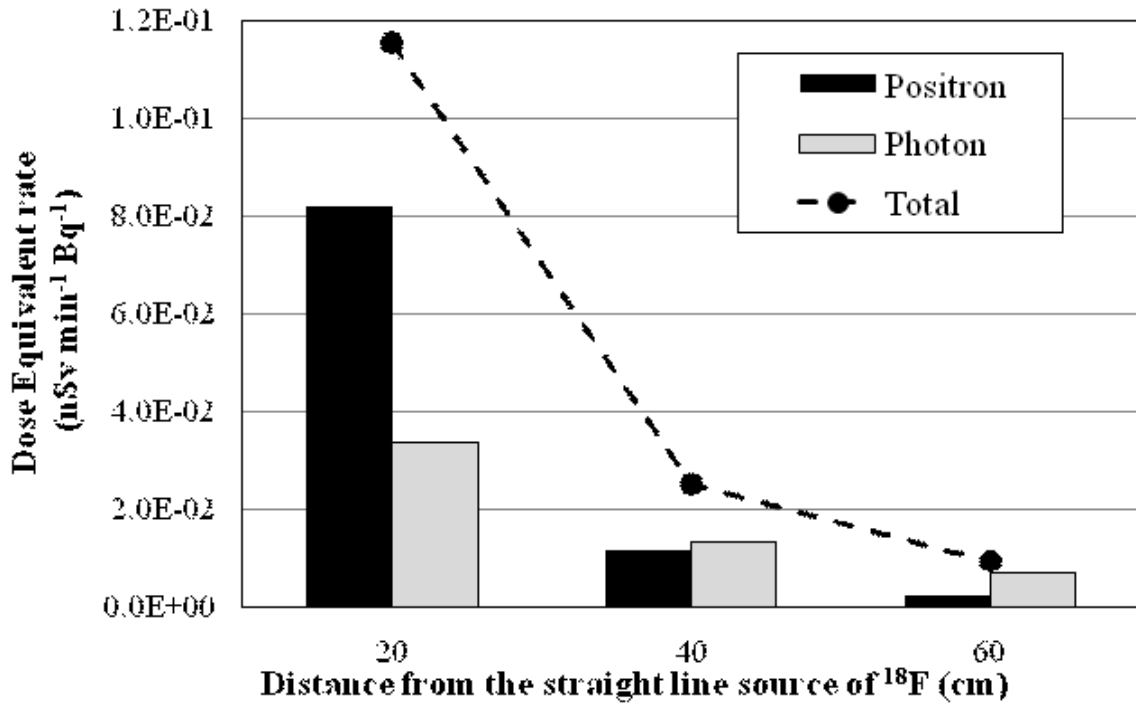


Figure 5. Dose equivalent rates for positrons and photons at 70 μ m depth of tissue.

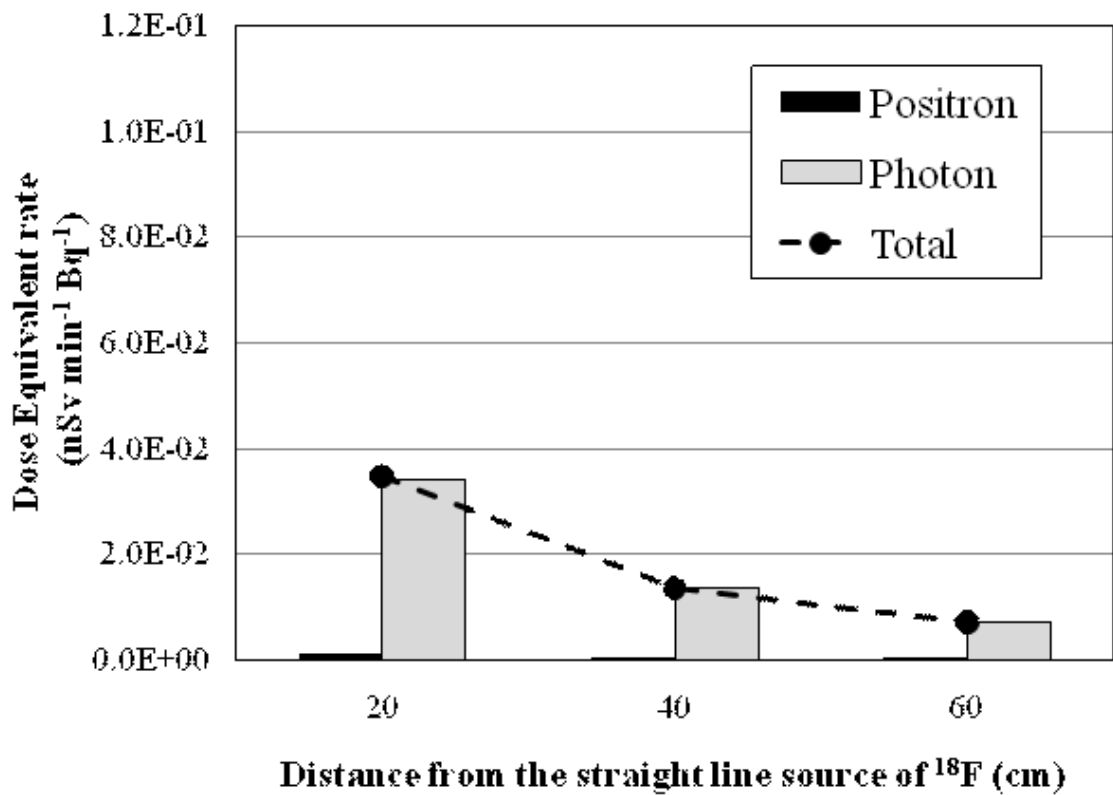


Figure 6. Dose equivalent rates for positrons and photons at 1 cm depth of tissue.

Estimation of patient exposure doses using anthropomorphic phantom undergoing X-ray CT examination

Y. Morishita¹, S. Koyama²

¹Department of Radiological Technology, Graduate School of Medicine, Nagoya University

1-1-20 Daikou-Minami, Higashi-ku, Nagoya, Japan

²Nagoya University School of Health Sciences

e-mail: morishita.yuki@e.mbox.nagoya-u.ac.jp

Abstract

The purpose of this study is to calculate accurate radiation exposure doses in patient using voxel phantom and incorporating specific effects of x-ray radiation in x-ray CT examination. In x-ray CT, a special filter called beam-shaping filter is positioned in front of x-ray tube. As the other factor, CT table reduces radiation dose. These factors were measured and incorporated in simulation code of Electron Gamma Shower version 5 (EGS5). Difference of measurement and calculation based on CT Dose Index (CTDI) in an acrylic cylindrical phantom was within 2.8 %. Detailed dose distribution in the voxel anthropomorphic phantom was obtained using the simulation. Measurement and calculation of organ doses denoted the same tendency of the location in the phantom, but near the end of scan area the calculation value was smaller than the measurement value. In the measurement, organ dose was underestimated by partial irradiation of the organ at the border of scan area.

1. Introduction

The dosage of x-ray radiation from CT (Computed Tomography) scanner has been estimated recently by using a Monte Carlo simulation. The purpose of this study is to calculate accurate radiation dose in patient from CT examination using voxel phantom. In the calculation, scanner-specific descriptions that include filtration designs, an x-ray tube orbital overlap and absorption of the CT table are necessary. For example, a special filter called “beam-shaping filter” which is positioned in front of the x-ray tube of the CT units causes less uniform x-ray fan beam. We took into account the effect of the filter based on measured data in the simulation.

The simulated exposure dosage figures are different between westerner and Japanese, because the model size of Japanese is smaller than westerner. Accordingly, a standard Japanese Model phantom used for in-phantom dosimetry system was developed by using the voxel phantom from CT DICOM(Digital Imaging and Communication in Medicine) format data. The calculation data was compared with measurements.

2. Materials and Methods

2.1 Overview

All simulations were performed using the EGS5 (Electron Gamma Shower ver.5) Monte Carlo code. For measurements and simulations, a Non-helical X-ray CT unit TCT-300 (Toshiba Medical Systems, Tochigi, JAPAN) was used.

2.2 Effect of beam-shaping filter

A typical CT scanner is equipped with x-ray beam filtration that includes the beam-shaping filter. The attenuations across the fan beam were different due to the filter. The beam-shaping filter is used to adjust the beam quality of x-rays after passing through a patient. There is no such published data on the design of beam-shaping filter, which may vary considerably from scanner to scanner. For estimation of the beam-shaping filter, two types of measurements were obtained: [a] Aluminum Half Value Layer (AL HVL) and [b] dose profiles, namely, attenuation of beam-shaping filter. We measured aluminum Half Value Layer (AL HVL) and dose value after passing through the filter and incorporated change of energy spectrums and photon number based on measured values in the simulation. New type of semiconductor dosimeter called Rapidose(Radcal, Monrovia, CA) was used for the measurements (Figure 1). Rapidose has functions that can measure dose and Al HVL at the same time and it is suitable for measurement of relatively high energy x-ray such as x-ray CT. In the measurement of the effect of beam-shaping filter, x-ray tube was positioned on the 0:00 direction on its orbital. Along a fan beam of x-ray CT, Rapidose was moved from 0 degree (downward vertical beam) up to 19 degrees (downward oblique beam) and measured at every one degree. It is assumed that the attenuation profile in the axial plane is symmetric about the central ray, so only measuring the half of the filter's attenuation is sufficient. In the simulation, photon number at each beam angle along the fan beam was determined by dose profiles and energy spectrums were generated by Birch's formula (Figure 2) based on AL HVL measured on each angle.

2.3 Specific factors related to a CT device

There are much further specific factors that are related to the CT scanner. Non-helical CT scanner has x-ray tube orbital overlap that causes overlap of x-ray exposure on the patient, resulting in an increase in radiation dose. For example, the irradiation from x-ray tube starts from 0 degree and stops at 360 plus extra degrees. The overlap angle was adjusted in the simulation to match the measured dose values in a acrylic cylindrical phantom because the information of the actual overlap angles wasn't published by the manufacturer. In our trials, x-ray tube rotation was estimated at 376 degrees including overlap of +/-8 degrees.

CT table top is usually made of carbon fiber due to its strength and low x-ray attenuation properties. The table was composed of density adjusted carbon in the simulation because the manufacture has not also published information on its actual density and composition. The density of the carbon was adjusted to correspond with the actual dose ratio table(+)/(-). The effect of attenuation of the table was developed in the simulation. These factors were also incorporated in our simulation code.

2.4 Measurement and calculation of CTDI

Computed Tomography Dose Index (CTDI) measured by using a CT acrylic cylindrical phantom was used for accuracy verification of our simulation. The CTDI phantom is 15 cm in length with a diameter of 30 cm. CTDI values are shown in air kerma (kinetic energy released in matter ; mGy) in the phantom's center hole and four peripheral holes ($0^\circ, 90^\circ, 180^\circ, 270^\circ$ position) when the x-ray tube rotates around the acrylic phantom. In order to determine the air kerma from CT examination, simulated deposit energies in units of MeV/gram/source particle were converted to air kerma in units of mGy by a conversion factor (C_f) [1]. An in-air normalization method that is based on pencil-chamber exposure reading for a single axial scan was taken at the center of the CT gantry. The conversion factor was defined as

$$C_f = \frac{(CTDI_{100,air, measured\ per\ mAs})}{(CTDI_{100,air, simulated\ per\ mAs})} \quad (1)$$

where $CTDI_{100,air, measured\ per\ mAs}$ is measured by an ion chamber free in air of the x-ray CT isocenter, and $CTDI_{100,air, simulated\ per\ mAs}$ is obtained by simulation.

The absorbed dose D_{ab} is calculated by

$$D_{ab} = D_{sim} \times C_f \quad (2)$$

where D_{sim} is the calculated dose in the simulation.

2.5 Development of voxel phantoms

A voxel phantom was developed based on CT image. Two different types of phantoms were used for calculations. One of them (THRA-1, Kyoto Kagaku Co., Kyoto, JAPAN) is only composed of lung, bone and soft tissue but can obtain organ doses using a number of internal semiconductor dosimeter installed at the position of tissues and organs assigned in the definition of the effective dose by ICRP publication 103 (Figure 3) [2]. The semiconductor dosimeter is implanted in the centroid of the organ and tissue. As a result, a number of organ doses were obtained immediately undergoing the x-ray CT examination. This system is called “in-phantom dosimetry system” and was used to compare measurement and calculation. Measurement and calculation were performed on thoracic scan protocol with a tube voltage of 120kV. The resolution of the axial simulation matrix was decreased from 512×512 to 170×170 to decrease runtime of the simulation. The size of each voxel was $0.1875 \times 0.1875 \times 1.0 \text{ cm}^3$.

Another phantom called CTU-41 (Kyoto Kagaku Co., Kyoto, JAPAN) includes the shapes of organs with individual densities. The average radiation dose to each organ was estimated in CTU-41 phantom. Both “in-phantom dosimetry system” and CTU-41 phantom were scanned by x-ray CT, and image data was output as DICOM format. The organs and tissues were assigned in each voxels using digital value (Hounsfield Unit). Original CT image and converted voxel image were shown in Figure 4. The simulations were performed using these two voxel phantoms.

3. Results and Discussions

3.1 Effects of a beam-shaping filter

Figure 5 shows the dose distribution and energy changes along the beam angle. The effective energy of x-ray beam determined using the measured AL HVL. Relative dose value maintained the same level from 0 degree to ± 4 degree, and after that it rapidly decreased as the angle became bigger. Similarly, effective energy maintained up to ± 4 degree, and then it rapidly increased as the angle became bigger and was saturated up from ± 9 degrees. The cause of the effect was that the thickness of the filter was bigger as the beam angle was bigger.

3.2 Comparison of CTDI between measurement and calculation

Table 1 shows comparison of measurements and calculations of CTDI. The difference between simulation and measurement result was calculated to evaluate the accuracy of the simulation. The agreement between measurements and calculations was within 2.8 %. The CTDI at 0° position was highest due to the x-ray tube orbital overlap and was lowest at 180° position due to the absorption of the CT table. The simulated CTDI values were approximately equal to measured CTDI values. With this result, the x-ray source and the geometry of the x-ray CT could be incorporated in the simulation successfully.

3.3 Result of calculation using voxel phantom

Result of the comparison of measurement and calculation of the in-phantom dosimetry system is shown in Figure 6(a). Locations of the calculation point were accorded with that of semiconductor dosimeters in the in-phantom dosimetry system. Measurement and calculation shown the same tendency on the same location in the phantom, but calculated values were generally slightly greater than measured values.

Figure 6(b) shows comparison of the organ doses between the in-phantom dosimetry system and the CTU-41 phantom. Dose values of the in-phantom dosimetry system were measurement values of centroid of each organ, and those of the CTU-41 phantom were calculation values of average dose of each whole organs converted from deposited energy. Calculated dose of the organ in the scan area such as lung was approximately equal to measurement dose, but the calculation dose of organ placed over the end of scan area such as thyroid resulted in significantly different from measured dose. In the calculation, the deposited energy in whole organ was divided by the organ mass and this value was presented as an average organ dose. When the organ was partially irradiated in the end of the scan area, average organ dose was smaller than the whole-organ irradiated case. In the measurement, the organ dose was presented maximum value as is the case in whole-organ irradiation if the evaluated point as a centroid of the organ fell within the scan area.

4. Conclusions

In this study the effect of the beam-shaping filter was successfully implemented in the simulation. The specific factor of CT unit such as the effect of orbital overlap and the attenuation of CT table was also incorporated in the simulation. Comparison of calculation and measurement by CTDI showed good agreement. The benefit of our method is that the effect of the beam-shaping filter can be incorporated easily if there isn't information like material or shape of the actual beam-shaping filter. Detailed dose distribution in the voxel phantom was obtained using the simulation. Measurement and calculation of organ dose shown the same tendency of each location in the phantom, but the calculation dose of organ placed over the end of scan area such as thyroid resulted in significantly different from measured dose. In the measurement, care should be taken when organ dose is estimated in such organ.

References

- 1) J Gu et al , The development, validation and application of a multi-detector CT(MDCT) scanner model for assessing organ doses to the pregnant and the fetus using Monte Carlo simulations, *Phys. Med. Biol.* 54 (2009) 2699–2717
- 2) K Fujii et al, Radiation dose evaluation in 64-slice CT examinations with adult and paediatric anthropomorphic phantoms, *The British Journal of Radiology*, 82 (2009), 1010–1018



Figure 1. New type of semiconductor dosimeter "Rapidose"

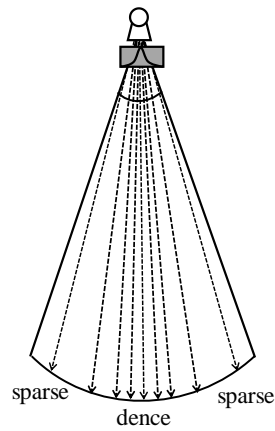


Figure 2. Incident photon number at each beam angle

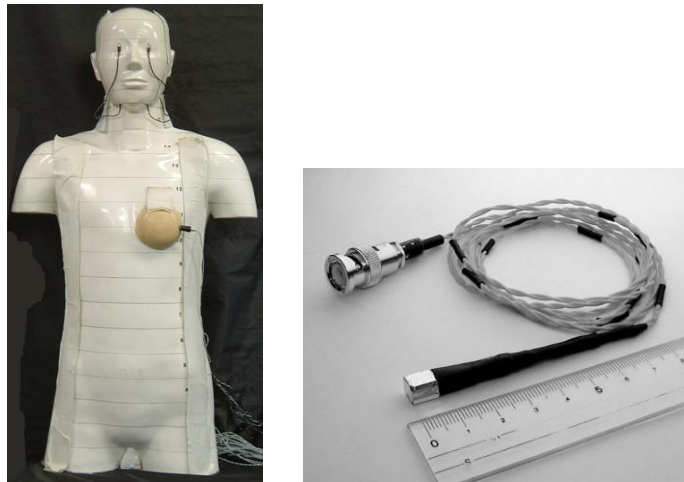


Figure 3. In-phantom dosimetry system.
 (a) The appearance of anthropomorphic phantom
 (b) Semiconductor dosimeter

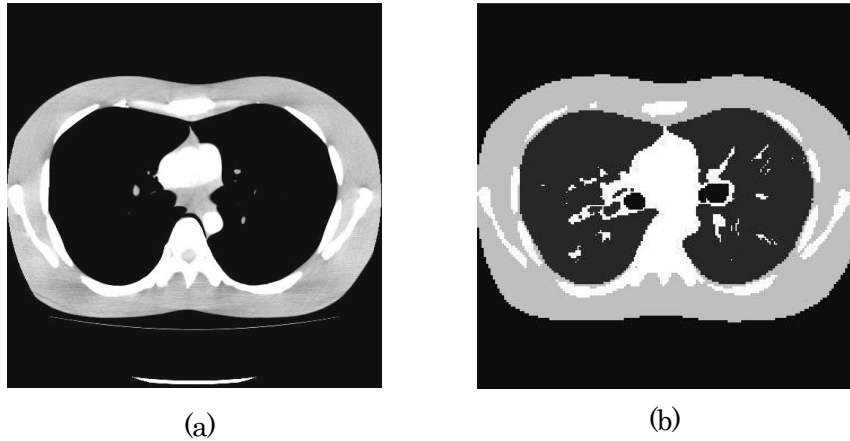


Figure 4. Images of transaxial plane of original DICOM image (a) and voxel phantom (b)

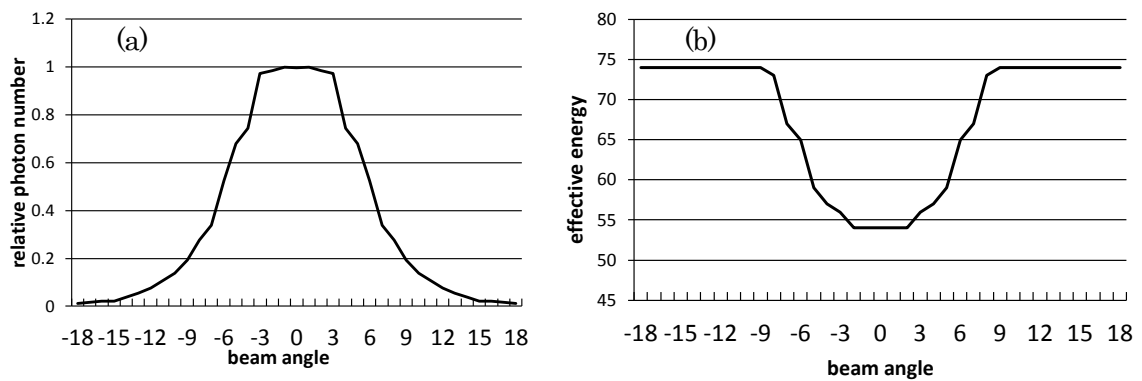


Figure 5. Relative dose and effective energy measured by Rapidose at each beam angle. (a)The relative dose at each beam angle (b)The effective energy calculated by measured Half Value Layer at each beam angle.

Table 1 Comparison of measurements and calculations of the CTDI.

position of the dosimeter	measurement [mGy]	simulation [mGy]	difference [%]
top	21.0	20.8	-1.2
center	11.7	11.5	-1.4
left	16.6	16.5	-0.4
right	16.0	16.5	2.8
bottom	14.8	14.5	-2.4

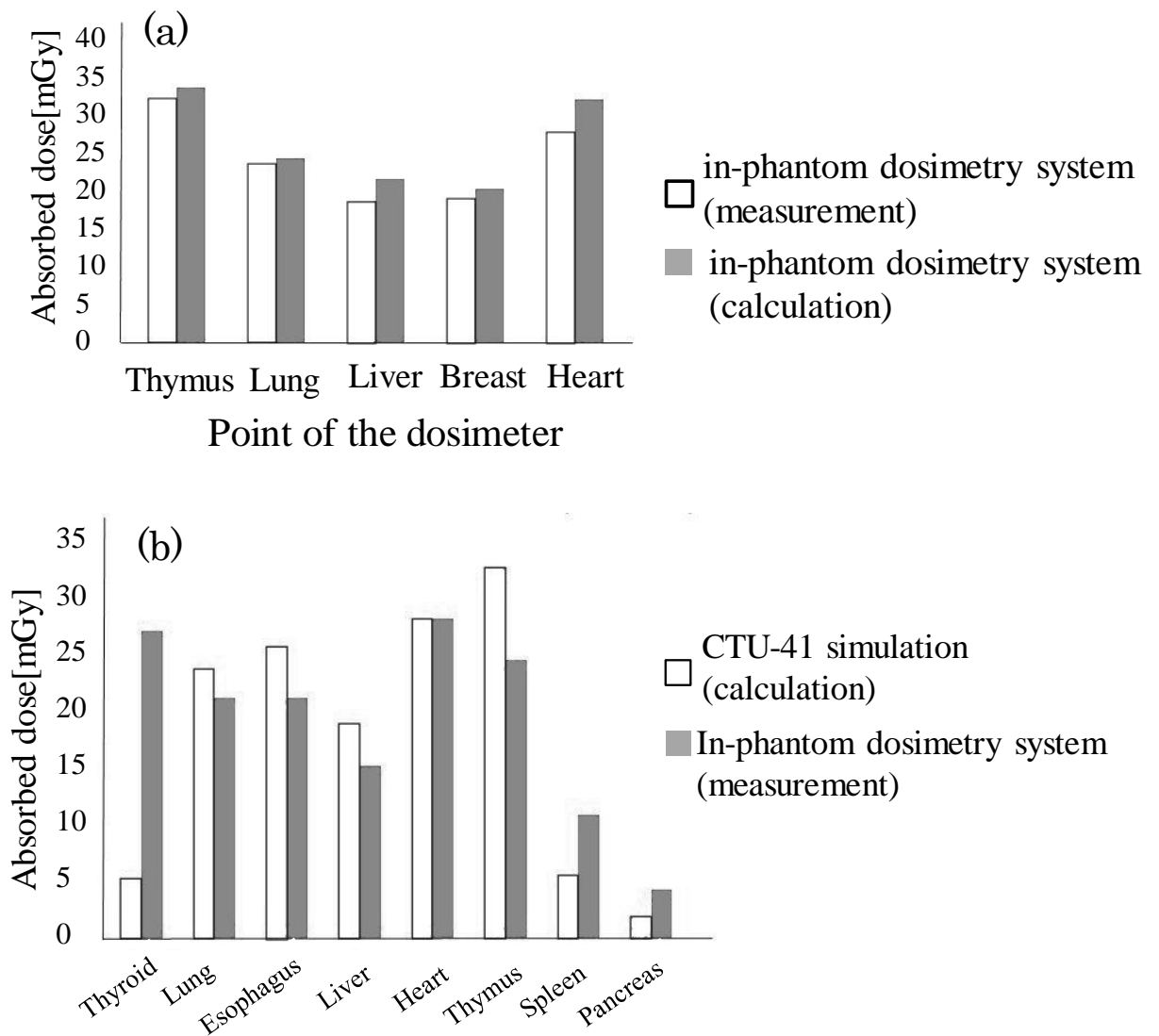


Figure 6. Comparison of measurement and calculation
 (a) point dose evaluation with same phantom (b) whole organ dose versus point dose

MONTE CARLO SIMULATION OF ENERGY DEPOSITION IN IMAGING PLATE

Takahisa Miyata, Hirotaka Rito, Masashi Kajihara, Tomoya Yamauchi, Keiji Oda
Graduate School of Maritime Sciences, Kobe University
5-1-1 Fukae-minamimachi, Higashinada-ku, Kobe 658-0022, Japan

e-mail: 103w526w@stu.kobe-u.ac.jp

Abstract

In order to design a suitable thickness of phosphor layer of an imaging plate, energy deposition by electrons has been simulated with a Monte Carlo code, EGS5. The phosphor layer was divided into smaller region of $0.1 \times 0.1 \text{ mm}^2$, and the energy deposited in each region was calculated by EGS5. The standard deviation of the distribution in the energy deposition could be obtained by a Gaussian fitting, and was compared with the result of measured distribution in photo-stimulated luminescence (PSL) intensity by using a β -ray source. A good agreement was confirmed for various average PSL intensities.

1. Introduction

An imaging plate (IP) is a kind of integral type detectors having the response proportional to the energy absorbed in sensitive layer as well as the OSL dosimeter. A commercially available IP is composed of a cover film, phosphor layer, substrate and magnet layers, among which only the second is sensitive to ionizing particles. Electrons and holes, of which number is proportional to the absorbed energy, were generated in the phosphor layer, and a part of them is stored in trapping centers. This is the step of memory of information on the absorbed dose, and then the information can be confirmed as the luminous intensity of PSL by using a specially designed IP reader.

Several attempts have been made in order to make this type of dosimeter more functional, *i.e.* to derive an information about particle species in addition to the total absorbed dose. The fading method is based on the experimental result that the degree of decrease in PSL after particle irradiation was different among particle species. In the repetition reading method, the intensity of the after-image depends on the type of ionizing particles. These method, however, are not practically applied because much time and effort should be consumed in the procedure of PSL measurement, and the IP reader should be remodeled. Then, a new technique has been proposed with consideration of spatial distribution of PSL intensity.

2. Particle identification based on PSL distribution

It is considered that measured PSL intensity in IP is, in theoretical, proportional to the energy deposited in the phosphor layer. Namely, the average PSL intensity, I_{av} , is expressed by the following equation;

$$I_{av} = fE_d N \quad , \quad (1)$$

where E_d is the deposited energy by each particle, N the number of incident particles, f the conversion factor from the energy deposition to PSL intensity. Let consider the case of uniform irradiation in a relatively large area, *e.g.* $3.2 \times 3.2 \text{ mm}^2$ or larger. If the area is divided into smaller regions, *e.g.* $0.1 \times 0.1 \text{ mm}^2$ or smaller, the number of incident particles in each region should not be the same but deviate around an average value according to the statistical fluctuation. It means that the width of the distribution in PSL intensity depends on E_d in eq. (1) in case of the same I_{av} . In the previous studies [1, 2], experiments of ^{241}Am α -ray, ^{90}Sr β -ray, accelerated proton, ^{137}Cs γ -ray and X-ray irradiation were carried out with various particle fluences. Figure 1 shows the dependence of the standard deviation of local PSL distribution on average PSL intensity. If the distribution in PSL intensity is decided only by the statistical fluctuation of the number of incident particles, relative standard deviation, Σ is obtained by the following formula;

$$\Sigma = \frac{1}{\sqrt{N}} \quad (2)$$

Combining eqs. (1) and (2), the following relation can be derived;

$$\log(\Sigma^2) = -\log I_{av} + \log fE_d \quad (3)$$

The variation of the relative standard deviation with the average PSL intensity can be expressed, in a full-log scale, by a straight line with a slope of -1, and is shown in Fig. 2.

The result suggests only a possibility of particle identification by using the distribution in PSL intensity. From a viewpoint of practical application, however, several considerations have not been made such as the pixel size, the thickness of phosphor layer, and so on. It is the purpose of this study to determine the optimum thickness of IP layer for better resolution of particle identification. In the first step, a Monte Carlo code, EGS5 [3] was employed and the results were checked by comparing with experimental ones in this report.

3. Monte Carlo simulation of energy deposition

A Monte Carlo code, EGS5 was used in this study to compare with experimental results obtained by an imaging plate exposed to β -rays. The electrons incident on the phosphor layer should lose their energy through collisions with constituent atoms along winding trajectories with a considerably long

range. So, some of their kinetic energy should be resultantly deposited apart from incident point. In order to preliminarily check the distance where the energy deposition takes place, a parallel beam of mono-energetic electrons of 0.5 and 1.0 MeV was incident on the hatched region of BaFBr layer in Fig. 3. As is shown in Fig. 4, the effect of crosstalk is about 1 % in the region 4 and less than 0.3 % in region 7, about 400 μm apart from the incident region.

The geometry of Monte Carlo simulation is shown in Fig. 5, where the imaging plate was composed of phosphor of 150 μm thick, substrate of 190 μm thick and magnet layer of 150 μm thick. The phosphor layer of 3.2x3.2 mm wide was subdivided into small elements of 0.1x0.1 mm wide. A disc-type β -ray source at a distance of 0.5 cm from the imaging plate should emit isotropically electrons with an energy distribution. The energy, E_d , deposited in small regions was normalized by the formula that $(E_d - E_{av})/E_{av}$, where E_{av} is the average energy deposition. The distribution of 1024 data in the normalized energy distribution is shown by a solid line in Fig. 6, together with an experimental result using a ^{90}Sr β -ray source represented by a dotted line. A good agreement can be confirmed between two results; which suggests a validity of Monte Carlo calculations.

The standard deviation can be calculated by fitting a Gaussian to respective distributions. Figure 7 shows the dependence of the relative standard deviation on the average PSL intensity or average energy deposition, where circles and triangles represent the results of experiments and Monte Carlo calculations, respectively. These data are plotted again in a full-log scale in Fig. 8, where a nearly straight line with an inclination of -1 can be confirmed. It is considered that a difference between of both results, especially large average PSL intensities, may be attributed to non-uniformity of β -ray source.

4. Conclusion

In the previous studies was proposed a particle identification technique based on the difference in PSL intensity distribution in relatively small regions. It is necessary to pay more attentions to a suitable thickness of sensitive layer of an imaging plate, optimized pixel size, and so on. In this study, the energy deposition by electrons has been simulated with a Monte Carlo code, EGS5. The phosphor layer was divided into small region of 0.1x0.1 mm^2 . The energy deposited by electrons in each region was calculated by EGS5. The standard deviation of the distribution in the energy deposition could be obtained by a Gaussian fitting, and was compared with the result of measured distribution in photo-stimulated luminescence (PSL) intensity by using a ^{90}Sr β -ray source. A good agreement was confirmed for various average PSL intensities.

More calculations for various IP thicknesses will be carried out in the next step, by which an optimum thickness and optimum pixel size will be determined.

References

- [1] K. Oda, K. Tsukahara, E. Tada and T. Yamauchi: "Proposal of New Method for Identifying Radiation Species Based on Distribution of PSL", *Japanese Journal of Radiation Safety Management*, 5 [1], pp.32-38, 2006.
- [2] K. Oda, K. Tsukahara, E. Tada and T. Yamauchi: "Analysis of Distribution of PSL Intensity Recorded in Imaging Plate", *Japanese Journal of Radiation Safety Management*, 5 [1], pp.101-106, 2006.
- [3] Y. Namito, H. Hirayama, A. F. Bielajew and S. J. Wilderman and W. R. Nelson: "THE EGS5 CODE SYSTEM", SLAC-R-730, KEK Report 2005-8 (2005).

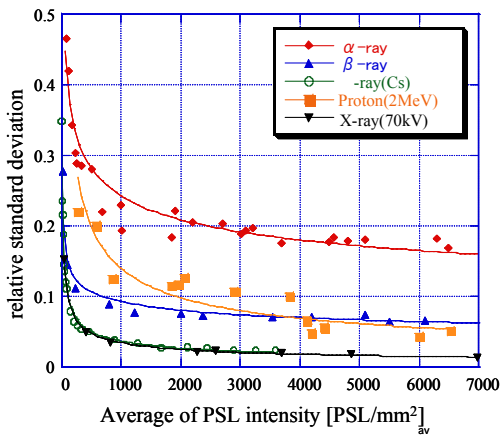


Fig. 1. Dependence of relative standard deviation on the average PSL intensity.

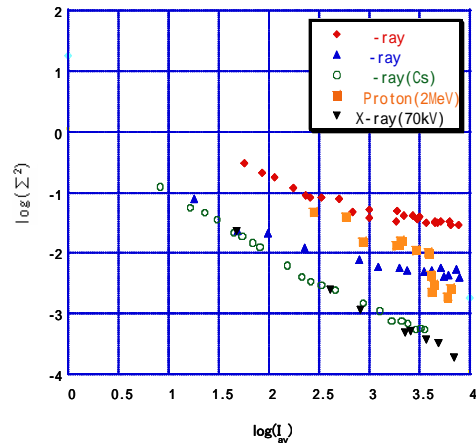


Fig. 2. Square of relative standard deviation as a function of the average PSL intensity in a full-log scale.

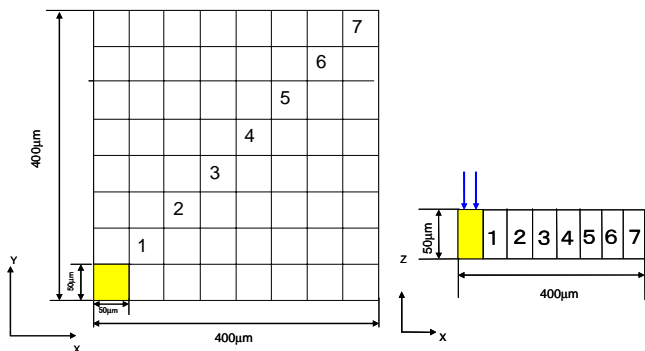


Fig. 3. Geometry for calculation of crosstalk effect.

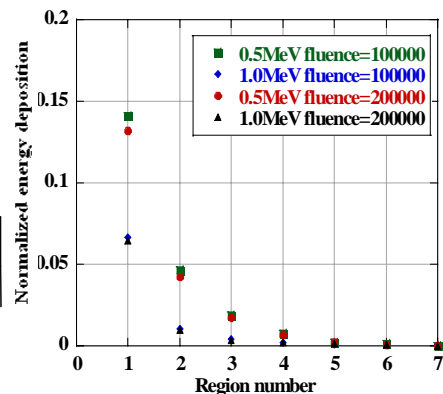


Fig. 4. Result of crosstalk effect.

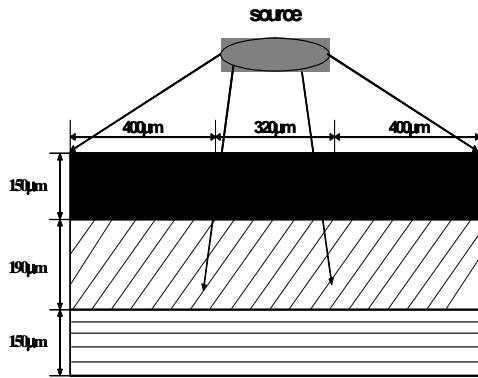


Fig. 5. Geometry for calculation of the energy deposited in phosphor region.

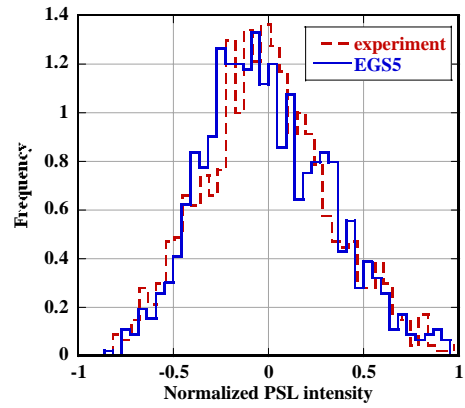


Fig. 6. Distribution of 1024 data in the deposited energy or PSL intensity.

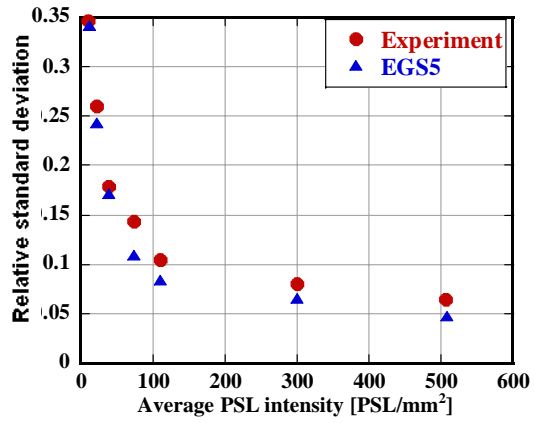


Fig. 7. Dependence of relative standard deviation on the average PSL intensity.

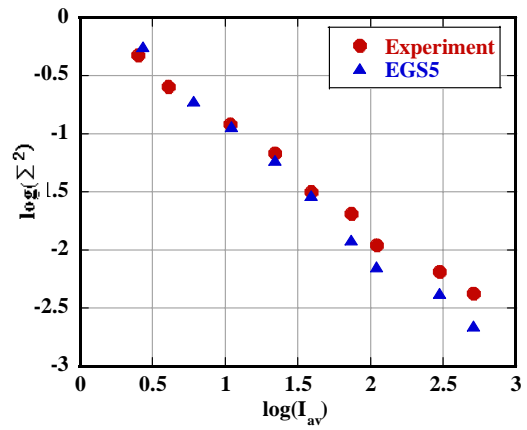


Fig. 8. Square of relative standard deviation as a function of the average PSL intensity in a full-log scale.

DEVELOPMENT OF AN MC GENERATOR FOR POLARIZED γ CONVERSION TO AN e^+e^- PAIR

D. Bernard

Laboratoire Leprince-Ringuet, CNRS/IN2P3 Ecole Polytechnique, 91128 Palaiseau France

Abstract

I am presenting a work in progress, an event generator as part of a project of polarimeter for cosmic γ -rays, which is presently in progress.

1 Introduction

At low energy, corresponding to optics and low energy X-ray photons, the knowledge of the fraction and of the direction of the polarization of the incoming radiation is a powerful tool to better understand the mechanism(s) at work inside cosmic sources. At higher energy, this diagnostic is badly missing [1].

Compton scattering can be used for polarimetry in the hard X-ray energy range, up to about 1 MeV [2] and there are several projects in progress using this method ([3] and references therein).

We at LLR [4] are developing a polarimeter for the γ -ray energy range, above pair creation threshold. The detector is an argon-based TPC, and construction is in progress.

2 Introduction

At low energy, polarimetry is performed inserting a filter in the beam, and measuring the variation of the transmitted (or reflected) flux, as a function of the azimuthal angle ϕ .

At high energy, the photon converts by interacting within a detector, the trajectories of the debris (A and B on Fig. 1) of the conversion are reconstructed, and the value of ϕ is measured from their angular configuration. In all cases, the modulation can be written as:

$$\frac{d\Gamma}{d\phi} \propto (1 + \mathcal{A}P \cos 2(\phi - \phi_0))$$

where P is the polarization fraction of the photon that we want to measure, $0 < P < 1$, and \mathcal{A} is the polarization asymmetry, that depends of the physical process at work in the conversion, $0 < |\mathcal{A}| < 1$. We wish obviously that $|\mathcal{A}|$ be as large as possible, and in particular if $\mathcal{A} = 0$ the detector has no polarimetric sensibility.

The variables that describe the final state completely are:

- The polar angles θ_+ and θ_- and the azimuthal angles φ_+ and φ_- which parameterize the direction of the outgoing electron and positron, respectively;
- The energy share between the electron and the positron.

The small energy carried by the nucleus or the electron of the detector, in the electric field of which the conversion took place, is neglected and the pair is assumed to carry away all the energy of the incoming photon ω , that is $E_+ + E_- = \omega$.

Writing an event generator starts from the differential cross-section which has been obtained from QED in the 1950's.

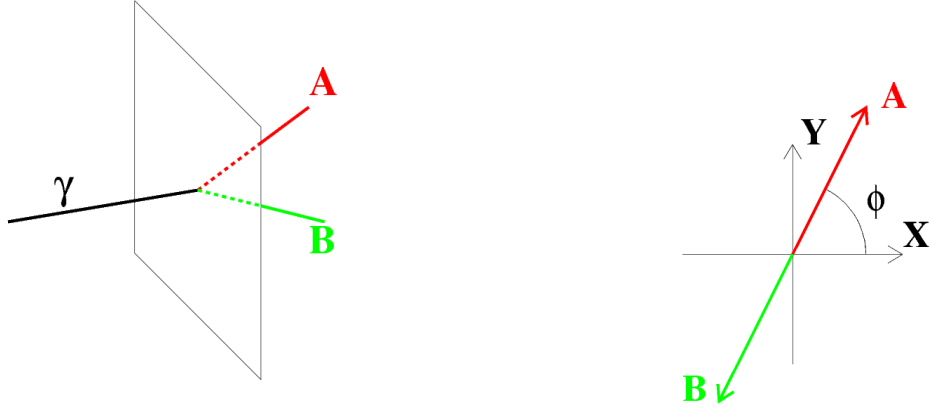


Figure 1: Left: Schema of the conversion of a photon to two secondary particles, A and B. Right: Angular configuration in the plane perpendicular to the photon flight direction

2.1 Linearly polarized photon

In practice it is useful to use the angles:

- ψ , the acoplanarity angle of the electron and positron,
- ϕ , the already mentioned “general” azimuthal angle of the event.

The angles ϕ and ψ are related to the positron and electron azimuthal angles φ_+, φ_- .

$$\psi \equiv \varphi^+ \quad (1)$$

$$\psi + \phi \equiv \varphi^- \quad (2)$$

Using the expression of the cross section for pair production by linearly polarized gamma-rays [7, 5]¹, together with their ϕ -averaged expression [6] that correspond to a non-polarized radiation, we obtain:

$$d\sigma = \Phi(X_u + P \times X_p)dE_+d\Omega_+d\Omega_- \quad (3)$$

, with:

$$\Phi = \frac{-\alpha Z^2 r_0^2 m^2 |p_-||p_+|}{(2\pi)^2 \omega^3 |\vec{q}|^4} \times F(q) \quad (4)$$

and

$$X_u = \left[\left(\frac{p_+ \sin \theta_+}{E_+ - p_+ \cos \theta_+} \right)^2 (4E_-^2 - q^2) + \left(\frac{p_- \sin \theta_-}{E_- - p_- \cos \theta_-} \right)^2 (4E_+^2 - q^2) + \frac{2p_+ p_- \sin \theta_+ \sin \theta_- \cos \phi}{(E_- - p_- \cos \theta_-)(E_+ - p_+ \cos \theta_+)} (4E_+ E_- + q^2 - 2\omega^2) - 2\omega^2 \frac{(p_+ \sin \theta_+)^2 + (p_- \sin \theta_-)^2}{(E_+ - p_+ \cos \theta_+)(E_- - p_- \cos \theta_-)} \right] \quad (5)$$

$$X_p = \cos 2(\phi + \psi)(4E_+^2 - q^2) \left(\frac{p_- \sin \theta_-}{E_- - p_- \cos \theta_-} \right)^2 + \cos 2\psi(4E_-^2 - q^2) \left(\frac{p_+ \sin \theta_+}{E_+ - p_+ \cos \theta_+} \right)^2 + 2 \cos(\phi + 2\psi)(4E_+ E_- + q^2) \frac{p_- \sin \theta_- p_+ \sin \theta_+}{(E_- - p_- \cos \theta_-)(E_+ - p_+ \cos \theta_+)} \quad (6)$$

¹Jauch and Rohlich [5] are mentioning that May's expression [7] is too small by a factor 2.

In these expressions,

- q is the momentum of the “recoiling” particle,

$$|\vec{q}|^2 = |\vec{p}_+ + \vec{p}_- - \vec{\omega}|^2 \quad (7)$$

- E_+ is the positron energy,
- $F(q)$ is an atomic form factor,
- and we have assumed that the polarization direction is along the x axis (Fig.1).

2.2 Generation

The generator is using the acceptance-rejection “Von Neuman” method described for example in the PDG [8]. The phase-space is 5-dimensionnal, and the variables generated are θ_+ , θ_- , ϕ , ψ and E_+ .

A complication arises from the fact that θ_+ and θ_- are strongly peaked close to zero, and ϕ close to π , something that reflects the forward, back-to-back in the center-of-mass-system, emission of the pair.

2.3 θ_+ , θ_- generation

The leading order term of the angular distribution is [9, 10, 11]:

$$\frac{d\sigma}{d\theta_{\pm}} = \frac{\sin \theta_{\pm}}{2p_{\pm}(E_{\pm} - p_{\pm} \cos \theta_{\pm})^2} \quad (8)$$

The generation of electron and positron polar angles is performed by the change of variable:

$$\cos \theta_{\pm} = \frac{E_{\pm}(2u - 1) + p_{\pm}}{p_{\pm}(2u - 1) + E_{\pm}} \quad (9)$$

where u is an uniformly distributed random number between zero and unity.

2.4 ϕ generation

The distribution of the angle ϕ is peaked at $\phi \approx \pi$. In practice, it was found convenient to examine the distribution of

$$v \equiv \ln(\cos \phi + 1) \quad (10)$$

v , when events are generated after pdf built from eq. (3), is peaked around a value that depends on the energy of the incoming photon

$$v_0 \equiv -0.026 - 1.226 \ln(\omega) \quad (11)$$

The slope of the decreasing exponential is found to be a constant $\beta \approx 2$. v is generated with the double exponential shape, and ϕ is obtained from v .

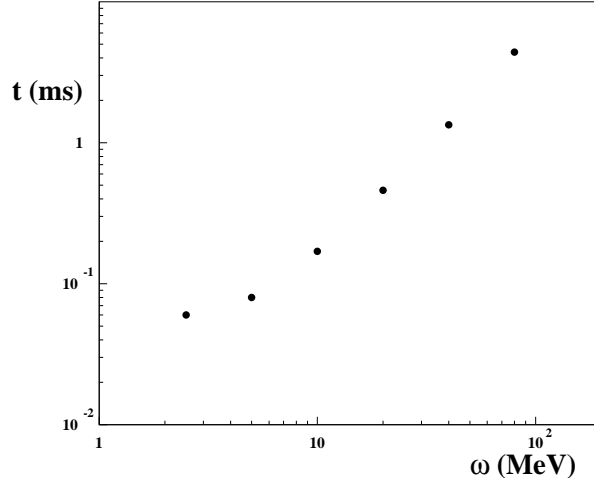


Figure 2: CPU time for the generation of one event, as a function of the energy of the incoming photon.

2.5 Event generation

At this point we have θ_+ , θ_- and ϕ generated. We now take $x = E_+/\omega$ at random, flat, and ψ , flat. The pdf of these events at this point is:

$$p_0(\theta_+, \theta_-, x, \phi, \psi) = p_0(\theta_+)p_0(\theta_-)p_0(\phi) \quad (12)$$

The true, final sample, after pdf p is obtained by a try/reject method: a scaling factor H is determined heuristically so that $H \times p_0 > p$. A number u is taken flat between 0 and 1.

- If $u \times H \times p_0 < p$ the event is kept.
- If $u \times H \times p_0 \geq p$ the event is not kept.

2.6 Validation

At the moment, minimal validation has been performed:

- The polarization asymmetry of the generated events is found to be close to 20% at high energy, as expected.
- The R.M.S. width of the θ_+ or θ_- angles distribution is found to be close to the predicted value [12], of $(m/\omega) \times \ln(\omega/m)$.

2.7 CPU time

Figure 2 shows the CPU time for the generation of one event, as a function of the energy of the incoming photon. The performance of the generator is well suited for our needs, less than 1 ms for $E < 30$ MeV, given that cosmic sources have a spectrum that is strongly decreasing with energy.

Nevertheless, this increase with energy is the sign of some potential of improvement, either in the generation of ϕ , or in the correlation between variables.

3 Conclusion

The generator is running and has been partially validated. After it has been completed I am aiming at providing it to the community as a plug-in for EGS5.

This work is part of an effort aiming at developing, characterizing and validating a concept of polarimeter for cosmic γ sources, but also to validate experimentally the computation, from theory, of the polarization asymmetries just above threshold, at a couple of MeV, where the cosmic signal is peaking, [13], at the same level of precision as what was done in the past for “nuclear” pair creation in the GeV energy range [14].

References

- [1] “Medium Energy Gamma-Ray Astrophysics”, Hunter S.D. et al, published in Astro2010: The Astronomy and Astrophysics Decadal Survey, Science White Papers, no. 137
- [2] “Status and prospects for polarimetry in high energy astrophysics”, M. L. McConnell, J. M. Ryan, *New Astron. Rev.* **48**,215 (2004).
- [3] “The MEGA Advanced Compton Telescope Project,” P. F. Bloser, R. Andritschke, G. Kanbach, V. Schoenfelder, F. Schopper and A. Zoglauer [the MEGA Collaboration], *New Astron. Rev.* **46**, 611 (2002).
- [4] Louis Leprince-Ringuet [1901 – 2000] founded the first high-energy physics laboratory in France.
LLR, Laboratoire Leprince-Ringuet, is a CNRS/IN2P3 Laboratoire at Ecole Polytechnique.
- [5] Jauch and Rohrlich, *The theory of photons and electrons* (Springer Verlag, 1976).
- [6] “The quantum theory of radiation”, W. Heitler, 1954.
- [7] “On the Polarization of High Energy Bremsstrahlung and of High Energy Pairs”, M. M. May, *Phys. Rev.* **84**, 265 - 270 (1951).
- [8] Section 33.3 page 311 of
W. M. Yao *et al.* [Particle Data Group], “Review of particle physics,” *J. Phys. G* **33**, 1 (2006).
- [9] “Improved angular sampling for pair production in the EGS4 code system”, A. F. Bielajew, NRCC Report: PIRS-0287R (1994).
- [10] “The EGS5 code system,” H. Hirayama, Y. Namito, A. F. Bielajew, S. J. Wilderman and W. R. Nelson, SLAC-R-730, KEK-2005-8, KEK-REPORT-2005-8, Dec 2005. 434pp.
- [11] “Simulation of pair production, particle angles”, in “Radiation transport in EGSnrc”, I. Kawrakow 2007-02-13 <http://www.irs.inms.nrc.ca/EGSnrc/pirs701/node24.html>
- [12] M. Stearns, “Mean Square Angles Of Bremsstrahlung And Pair Production,” *Phys. Rev.* **76**, 836 (1949).
- [13] “Polarimetry of cosmic γ -rays above pair-creation threshold and towards a precise measurement of the polarization asymmetry”, D. Bernard, seminar given at SPring8 / NewSubaru, Hygo, Japan, 29 July 2010.
- [14] C. de Jager *et al.*, “A Pair Polarimeter for Linearly Polarized High Energy Photons”, presented at ICTP 4th International Conference on Perspectives in Hadronic Physics, Trieste, Italy, 12-16 May 2003, *Eur. Phys. J. A* **19**, S275 (2004).